Technical University of Munich
Ludwig Maximilian University of Munich
Max Planck Institute of Quantum Optics

Towards Finite Energy Quantum Simulation of the 2D Fermi-Hubbard Model

Alberto Cavallar

Submitted in Partial Fulfillment of the Requirements for the
Master of Science in
Theoretical and Mathematical Physics

Supervisor: Prof. Dr. J. Ignacio Cirac
Second Examiner: Dr. Luis Escalera

August 29, 2024

Technische Universität München
Ludwig-Maximilians-Universität München
Max Planck Institut für Quantenoptik

Zur Quantensimulation des 2D-Fermi-Hubbard-Modells bei endlicher Energie

Alberto Cavallar

Vorgelegt in teilweiser Erfüllung der Voraussetzungen für die
Erlangung des Grades eines Masters of Science in
Theoretischer und Mathematischer Physik

Betreuer: Prof. Dr. J. Ignacio Cirac
Zweitgutachter: Dr. Luis Escalera

August 29, 2024

Der erste Trunk aus dem Becher der Naturwissenschaft macht atheistisch,
aber auf dem Grund des Bechers wartet Gott.

Werner von Heisenberg (1901-1976).
Nobelpreisträger 1932, Direktor des Max Planck Institutes für Physik.

Thesis advisor: Prof. Dr. J. Ignacio Cirac *Alberto Cavallar*

Towards Finite Energy Quantum Simulation of the 2D Fermi-Hubbard Model

ABSTRACT

Understanding low-energy states of a fermionic quantum system is a problem of great significance in condensed matter physics. However, preparing these many-body states quickly becomes intractable for classical computers. Digital quantum computers can, in principle, be used efficiently for this task, but current noisy intermediate-scale quantum (NISQ) devices are still limited by the number of available qubits, their gate fidelities and the maximum circuit depth. Analog quantum simulators offer another pathway to understand many-body systems for specific native models, while being limited in the kind of available operations.

In this work, we study a quantum-classical algorithm for investigating microcanonical properties of the two-dimensional Fermi-Hubbard model. The algorithm is to be implemented in a hybrid fermionic quantum processor combining the advantages of both analog and digital modes in a single platform based on neutral atoms in an optical lattice. It relies on a virtual filtering operation that, without the need to prepare the physical state, allows to compute expectation values of a microcanonical ensemble. The protocol uses measurements of Loschmidt echos for an efficiently preparable initial state. We further present a concrete pathway to obtain the Loschmidt echo in a fermionic quantum processor, together with a benchmark of suitable low-energy initial states. Hopefully, this work will contribute to a better understanding of ground and finite temperature states in fermionic quantum many-body systems.

Betreuer: Prof. Dr. J. Ignacio Cirac *Alberto Cavallar*

Zur Quantensimulation des 2D-Fermi-Hubbard-Modells bei endlicher Energie

ZUSAMMENFASSUNG

Das Verständnis niederenergetischer Zustände eines fermionischen Quantensystems ist ein Problem von großer Bedeutung in der Physik der kondensierten Materie. Die Vorbereitung dieser Vielteilchenzustände wird jedoch für klassische Computer schnell zu einer unlösbaren Aufgabe. Digitale Quantencomputer können im Prinzip effizient für diese Aufgabe eingesetzt werden, doch sind die derzeitigen NISQ-Geräte (noisy intermediate-scale quantum) durch die Anzahl der verfügbaren Qubits, ihre Gattertreue und die maximale Schaltungstiefe begrenzt. Analoge Quantensimulatoren bieten einen weiteren Weg, um Vielteilchensysteme für bestimmte native Modelle zu verstehen, sind aber in der Art der verfügbaren Operationen begrenzt.

In dieser Arbeit untersuchen wir einen quantenklassischen Algorithmus zur Untersuchung der mikrokanonischen Eigenschaften des zweidimensionalen Fermi-Hubbard-Modells. Der Algorithmus soll in einem hybriden fermionischen Quantenprozessor implementiert werden, der die Vorteile von analogen und digitalen Modi in einer einzigen Plattform auf der Grundlage von neutralen Atomen in einem optischen Gitter kombiniert. Er beruht auf einer virtuellen Filterung, die es ermöglicht, Erwartungswerte eines mikrokanonischen Ensembles zu berechnen, ohne den physikalischen Zustand vorbereiten zu müssen. Das Protokoll verwendet Messungen von Loschmidt-Echos für einen effizient vorbereitbaren Anfangszustand. Weiterhin stellen wir einen konkreten Weg vor, um das Loschmidt-Echo in einem fermionischen Quantenprozessor zu erhalten, zusammen mit einem Benchmark geeigneter niederenergetischer Anfangszustände. Wir hoffen, dass diese Arbeit zu einem besseren Verständnis von Grundzuständen und Zuständen mit endlicher Temperatur in fermionischen Quanten-Vielteilchensystemen beitragen wird.

Contents

Chapter 1

Introduction

Quantum simulation is possibly one of the most promising applications of quantum physics, given that quantum many-body systems are hard to simulate classically in an efficient manner. While analog simulators are special purpose devices designed to provide insight on such questions, universally programmable digital quantum computers would be capable of solving any quantum problem. Specially interesting is the simulation of fermionic systems, describing e.g. the behavior of strongly correlated electrons in a material, key for understanding physical properties such as high-temperature superconductivity. One prominent model of such rich physics is believed to be captured in the two-dimensional Fermi-Hubbard Hamiltonian, which up to date has not been fully understood yet. While some properties such as solving its ground state are known to be hard problems, experimentally accessing specific phases can in turn encounter technical constrains such as limitations in the low entropies that can be reached.

Instead, in this work we aim to overcome these obstacles by exploiting the capabilities of the FermiQP demonstrator. The FermiQP project on a fermionic quantum processor combines the advantages of both analog and digital simulation in realizing a new and scalable hybrid platform based on neutral ^{6}Li atoms on an optical lattice. There, the dynamics of the analog quantum simulator implementing highly entangling operations on all of the particles with time-dependent control, can be merged with digital operations leading to a programmable fermionic quantum simulator.

Taking advantage of this platform, this work aims to propose a hybrid quantum-classical algorithm adapted to the given hardware to allow probing both low-temperatures and doped regions in the phase diagram of the 2D Fermi-Hubbard model. The efficient algorithm for the study of observables at finite energy will rely on the virtual filtering of an easy-to-prepare state that has overlap with states in a given energy window. The algorithm will avoid the filtering of the state by recovering the physical values from specific so-called Loschmidt echos retrieved by the quantum simulator. These quantities are complex numbers whose amplitude can be easily retrieved experimentally, yet leaving the phase resolution a challenging task. Thus, a concrete solution for this problem will also be addressed, involving the implementation of a short imaginary time evolution.

The structure of the thesis is as follows. Chapter 2 overviews the history of quantum computing and the state of the art on fermionic quantum simulation. The chapter ends with an introduction to the Fermi-Hubbard model and a presentation of the FermiQP demonstrator, on which the algorithm is meant to be run.

Chapter 3 contains the main results on the proposed algorithm, starting with a motivation from the physical point of view. A section describing the algorithm itself based on a virtual filtering follows. Next, after studying a family of efficiently preparable initial states composed of plaquettes, two different proposals for their adiabatic preparation are made. Last, the implementation of a short imaginary time evolution addressing the phase resolution of Loschmidt echos is discussed in detail.

Chapter 4 provides a summary of the proposed protocol on a small, proof-of-principle system, clearly stating the different steps to be followed in the recipe both at the experimental level in the first instance (quantum part of the protocol) followed by the classical post-processing. Some numerical simulations are added as a last section in this chapter.

Finally, a summary on the obtained results is provided and an outlook is given (Ch. 6). An appendix includes the python code for the simulation of the whole protocol based on the QuSpin package.

Chapter 2

Preliminaries

2.1 A short story on Quantum Computing

Back in the early decades of 20th centry, the fields of quantum mechanics and computer science lived in distant academic worlds. While quantum theory developed to give an explanation to observed atomic scale phenomena such as the wave-particle duality, digital computers appeared to replace humans in tedious computational tasks and even ended up playing a decisive role e.g. in wartime cryptography.

These fields began to converge when physicist began to apply quantum mechanical models to solve computational problems, replacing bits for qubits. Starting in 1980, Benioff [1] introduced the concept of a quantum Turing machine describing a simplified computer based on the Hamiltonian evolution of a pure state. At the same time, Manin [2] independently formulated the idea of a quantum automaton that used superposition and entanglement. Slightly later in 1982, Feynman [3] suggested building a computer based on quantum phenomena to efficiently face the exponential increase in computational complexity when simulating quantum dynamics with classical computers.

Although at that time quantum computers were still only hypothetical, the first quantum algorithms for those machines already started to emerge during the subsequent two decades. Deutsch and Jozsa [4], Simon [5] and Bernstein and Vazirani [6] provided algorithms for oracle problems that demonstrated mathematically an information gain by querying a black box with a quantum state in superposition. Further, Shor [7] showed in 1994 that a scalable quantum computer would be able to break RSA and Diffie–Hellman encryption protocols, drawing a significant attention to the field of quantum computing. Two years later, Grover's algorithm [8] proved a quantum speedup for the widely applicable unstructured search problem, while the same year Lloyd [9] validated Feynman's conjecture establishing that quantum computers could indeed simulate quantum systems circumventing the exponential overhead from classical simulations.

In 1995, the idea of quantum computing became concrete when Cirac and Zoller [10] proposed a way to realize a universal quantum computer using lasers and trapped ionized atoms. Over the years, several other approaches have been introduced on the hardware side, ranging from superconducting circuits [11–13] and ultracold quantum gases [14–17] to quantum dots [18] and photonic systems [19], among others. Still, several technical challenges have to be overcome before being able to exploit the resources of entanglement and superposition for computation. For this reason, already in the year 2000

DiVincenzo [20] proposed a list of requirements for a quantum computer to be practical. It happens that, besides the need for universality and scalability, extreme isolation of the quantum system from the outside world is necessary to restrain decoherence of quantum states, while at the same time an incredible accurate control of said system including state initialization and measurement precision have to be concealed. The failing in any of these latter conditions will lead to errors in the computation, varying in kind among the different platforms. The threshold theorem, in turn, describes how quantum error correction techniques can be used to mitigate those errors, provided the physical error rate lies below a certain threshold [21–23].

Potential applications for fault-tolerant quantum computers extend from cybersecurity, data analytics and artificial intelligence, to optimization and simulation tasks, even though their era has not arrived yet. Nonetheless, it is believed that noisy intermediate-scale quantum (NISQ) machines could already show a technical quantum advantage in the near future[1] — a *comercial* advantage remaining still unclear.

2.2 Fermionic Quantum Simulation

Specially interesting is the simulation of complex quantum systems in condensed matter physics and quantum chemistry, key for the development of e.g. material science and drug discovery, since in general they remain a hard task even for today's supercomputers. While these could be addressed by a universal quantum computer, even simpler special-purpose analog devices — that would require less control and therefore be easier to construct — can be used: quantum simulators [25–27]. These have emerged as one of the most promising applications in the field of quantum computing [28], since the technologies required for the coherent control of such quantum systems have matured to allow for the physical implementation of practical quantum simulation in the very near future [29–35]. Although in equilibrium quantum simulators have not reached the predictive power of numerical simulations [36, 37], interesting results have been obtained for time-dependent phenomena [38, 39] and even a quantum advantage is possible [40].

A common thread for these experiments is their ability to realize a given Hamiltonian H — a model of the physical system that dictates the quantum dynamics of states $|\psi\rangle$ governed by the Schrödinger equation $i\frac{\partial}{\partial t}|\psi\rangle = H|\psi\rangle$ — as well as being equipped with initial state preparation and final measurement capabilities. The unitary evolution e^{-iHt} of the quantum state, $|\psi(0)\rangle \mapsto |\psi(t)\rangle$, can be realized either through a continuous transformation of the model's parameters (analog mode) if the whole Hamiltonian is native, or alternatively by a sequence of discrete unitary gates (digital mode). Key for the latter approach is the fact that the evolution under a k-local Hamiltonian $H = \sum_{m=1}^{M} H_m$ on N qubits — meaning that its terms H_m act on k qubits at most each — can be broken into smaller efficiently-implementable pieces through a Suzuki-Trotter

---

[1] As of July 2024, the quantum computing company Quantinuum has already announced that their new 56-qubit H2-1 computer has broken a world record in *quantum advantage*, surpassing the performance of benchmarking set by Google's Sycamore machine (2019) by 100-fold [24].

decomposition [9, 41, 42],

$$e^{-iHt} = \left(\prod_m e^{-iH_m t/\ell}\right)^{\ell} + \mathcal{O}\left(\frac{t^2}{\ell}\right), \tag{2.1}$$

up to an arbitrarily small digital error[2] $\mathcal{O}(t^2/\ell)$, with ℓ being the chosen number of Trotter steps. That is, the Hamiltonian evolution can be approximated arbitrarily well by repeating ℓ times the sequence of gates corresponding to the product of local terms for time slices t/ℓ. Sometimes, a simple Trotterization $e^{-iHt} \simeq \prod_m e^{-iH_m t}$ with corresponding error $\mathcal{O}(t^2)$ suffices for short time.

However, several outstanding computationally-challenging many-body problems in condensed matter physics and quantum chemistry describing e.g. electronic dynamics are naturally expressed in terms of indistinguishable fermions instead of distinguishable qubits. As discussed by Bravyi and Kitaev [43], at the fundamental level fermionic systems do not satisfy the postulate that *each operation is described by a unitary operator which is the tensor product of some operator U, acting on the selected qubits, and the identity operator acting on the rest of the system:* $\mathbb{1} \otimes \cdots \otimes U \otimes \cdots \otimes \mathbb{1}$. Hence using fermions as carriers of quantum information should be considered as a different computational model, encoding the information in the occupation number of sites — the so-called local fermionic modes — rather than in the internal spin or energy states of an atom as in the qubit counterpart. Local fermionic modes are defined in terms of fermionic operators through the ordered string

$$|n_1, ..., n_N\rangle = \left(c_1^\dagger\right)^{n_1} \cdots \left(c_N^\dagger\right)^{n_N} |0, ..., 0\rangle \tag{2.2}$$

acting on the vacuum, specifying the occupation $n_j \in \{0, 1\}$ on each site $j \in \{1, ..., N\}$. Since fermionic annihilation (creation) operators c_j ($c_j^\dagger$) follow the anti-commutation relations[3] $\{c_i, c_j\} = \{c_i^\dagger, c_j^\dagger\} = 0$ and $\{c_i, c_j^\dagger\} = \delta_{ij}$, their action on the local fermionic modes will be given by

$$c_j|n_1, ..., n_{j-1}, 1, n_{j+1}, ..., n_N\rangle = (-1)^{\sum_{s=1}^{j-1} n_s}|n_1, ..., n_{j-1}, 0, n_{j+1}, ..., n_N\rangle, \tag{2.3}$$

$$c_j|n_1, ..., n_{j-1}, 0, n_{j+1}, ..., n_N\rangle = 0, \tag{2.4}$$

making explicit through the phase factor $(-1)^{\sum_{s=1}^{j-1} n_s}$ that the order in the basis elements matters. Applying a gate to a set of local fermionic modes will thus require special care.

---

[2] This means that for any given $\epsilon > 0$ and t, there exists a n_ϵ such that e^{-iHt} can be computed with an error smaller than ϵ in at most $n_\epsilon M 2^{2k}$ operations, which is polynomial in N whenever $M = \text{poly}(N)$ as in the case of nearest neighbor interactions. The error stems from the non-commutativity of the different terms H_m.

[3] Electrons are fermions, whose statistics are governed by an anti-symmetry in the wave function when swapping two such particles: $\psi(\mathbf{r}_1, \mathbf{r}_2) = -\psi(\mathbf{r}_2, \mathbf{r}_1)$. This implies that no two fermions can simultaneously have the the same quantum numbers (Pauli exclusion principle), since $\psi(\mathbf{r}, \mathbf{r}) = -\psi(\mathbf{r}, \mathbf{r})$ would imply $\psi(\mathbf{r}, \mathbf{r}) = 0$ leading to a vanishing probability $|\psi|^2$ for that configuration. This anti-symmetry is captured by a vanishing anti-commutator, which is defined as $\{A, B\} = AB + BA$.

One possibility is to map fermionic local modes and operators to qubits and the corresponding unitary operators, and then employ the well-established quantum computing tools and algorithms. This comes at the expense of an additional overhead when dealing with system dimensions higher than one. The most known and probably oldest such mapping from fermions to qubits is the so called Jordan-Wigner transformation [44], which stores the occupation number of the ith fermionic mode in the ith qubit

$$|n_1, ..., n_N\rangle \mapsto |q_1, ..., q_N\rangle, \quad n_i, q_j \in \{0, 1\}, \tag{2.5}$$

leaving the encoding of the nonlocal behavior (the parity information) to the operators,

$$c_j \mapsto Z_1 \otimes \cdots \otimes Z_{j-1} \otimes \frac{1}{2}(X_j + iY_j) \otimes \mathbb{1}_{j+1} \otimes \cdots \otimes \mathbb{1}_N \tag{2.6}$$

and its hermitian conjugate, where X, Y, Z are the usual Pauli qubit gates. The problem with this method is that as a consequence of the non-locality of the parity operator $\mathbf{Z}_j \equiv Z_1 \otimes \cdots \otimes Z_j \otimes \mathbb{1}_{j+1} \otimes \cdots \otimes \mathbb{1}_N$, the number of extra qubit operations required to simulate a single fermionic operator scales as $\mathcal{O}(N)$.

This overhead can be reduced by further methods, such as the Bravyi-Kitaev superfast encoding [43] reducing the simulation cost to $\mathcal{O}(\log N)$ qubit operations per fermionic operation. There has been a lot of progress in the past years on optimizing fermion-to-qubit mappings, ranging from the Verstraete-Cirac transformation in 2005 [45] to the more recent maps such as the Generalized Superfast Encoding [46] in 2018, the Compact Derby-Klassen [47] in 2020, both the Super Compact [48] and Optimal [49] in 2023, and the fresh Ultrafast hybrid a few months back this year 2024 [50], among others.

However, they all have in common that in some way or another they have to deal with an extra overhead (in number of qubits or circuit depth, for instance) to simulate the fermionic behavior. The application of such transformations in more than one dimension or with long-range couplings leads to multi-spin interactions in the resulting Hamiltonian, breaking the locality of its terms and thus making its quantum simulation demanding. Alternatively, these issues can be circumvented by using the Fermi Statistics as a native resource to simulate fermions with fermions, in contrast to qubit-based simulators.

One example is given by last year's (2023) work by Zoller's group [51], where a proposal on fermionic digital quantum processing is made by using programmable neutral atom arrays with Rydberg states to locally encode fermionic modes in a fermionic register and simulate them in a hardware-efficient manner using fermionic gates. The authors argue that a generalization of the Bravyi-Kitaev [43] fermionic gate set

$$\mathcal{BK} = \left\{ e^{i\frac{\pi}{4}n_j}, e^{i\pi n_i n_j}, e^{i\frac{\pi}{4}(c_i^\dagger c_j + \text{h.c.})} \right\} \tag{2.7}$$

— universal when restricted to global particle-number conserving transformations — given by

$$\mathcal{G} = \left\{ \mathcal{U}_{i,j}^{(\text{int})}(\theta), \mathcal{U}_{i,j}^{(\text{tun})}(\boldsymbol{\theta}) \right\} \tag{2.8}$$

with

$$\mathcal{U}_{i,j}^{(\text{int})}(\theta) \equiv e^{-i\theta n_i n_j}, \tag{2.9}$$

$$\mathcal{U}_{i,j}^{(\text{tun})}(\boldsymbol{\theta}) \equiv e^{-i\left[\frac{\theta_1}{2}\left(e^{-i\theta_2} c_i^\dagger c_j + \text{h.c.}\right) + \frac{\theta_3}{2}(n_i - n_j)\right]}, \quad \boldsymbol{\theta} = (\theta_1, \theta_2, \theta_3), \tag{2.10}$$

can be precisely realized in experiments. Based on these results, the analysis of Li et al. [52] shows that the fermionic simulators indeed outperform their qubit counterparts with respect to resources for quantum evolution (regarding circuit depth), as well as classical optimization (regarding number of required parameters and iterations). Besides, it turns out that the relative advantage of fermionic simulators becomes even more pronounced as interaction becomes stronger, or tunneling is allowed in more than one dimension, as well as for spinful fermions. This improvement is furthermore scalable, meaning that the performance gap between fermionic and qubit simulators only grows for bigger system sizes. Even variational algorithms for fermionic quantum simulation in chemistry to be implemented in such today's existing Rydberg atom architectures have already been proposed. [53]

There are, nevertheless, other possibilities for native fermionic quantum simulation. A promising one is found in cold atom platforms in optical lattices directly using fermionic isotopes. In the present work we focus on a special instance of such an apparatus, a *fermionic quantum processor*, capable of natively realizing the Fermi-Hubbard model and generalizations of it, which we introduce next.

2.3 A Fermionic Quantum Processor

A particularly good example of the complex problems addressed in fermionic quantum simulation is the determination of low-energy properties and dynamics in the Fermi-Hubbard model, which is a prototypical model for describing strongly interacting electrons in solids. Although in one dimension the Hubbard model is exactly solvable [54], in two dimensions it has been a long-term challenge to find the lowest-energy states of this model, although a lot of recent progress has been made [36, 55].

Interestingly, the Hubbard model can be realized with cold atoms in an optical lattice, where fermionic atoms represent the electrons. These are trapped in an interference pattern of light formed by overlapping laser beams, with tunable interparticle interactions. Quantum gas microscopy has made it possible to take full spin- and charge-resolved photographs of such systems, revealing a complex interplay of magnetic ordering and mobile dopants at the microscopic level [56, 57]. Exciting recent progress on Fermi-Hubbard experiments has already been made by different groups in the world leaded by Markus Greiner [58–60], Martin Zwierlein [61] and Waseem Bakr [62, 63].

Using this very same technology, a fermionic quantum processor (FermiQP) for hybrid digital-analog quantum simulation is currently being realized at the Max Planck Institute for Quantum Optics (MPQ) in the Quantum Many-Body Systems Division of Prof. Dr. Immanuel Bloch in collaboration with the Theory Division of Prof. Dr. Ignacio Cirac and several other project partners.[4]

---

[4] These include Dr. Philipp Preiss and Dr. Timon Hilker coordinating the construction of the demonstrator at MPQ, Prof. Dr. Monika Aidelsburger at the Ludwig Maximilian University of Munich, Prof. Dr. Christian Groß at the Eberhard Karls University Tuebingen, Prof. Dr. Tommaso Calarco at Forschungszentrum Jülich, Prof. Dr. Jens Eisert at Free University Berlin, Prof. Dr. Andreas Tünnermann at the Fraunhofer Institute for Applied Optics and Precision Engineering, as well as

2.3.1 Fermi-Hubbard model

As a starting point, we introduce in some detail the Fermi-Hubbard model, one of the nowadays most widely known in condensed matter physics. The Hubbard Model was first proposed in the 1960s to describe the behavior of electrons in narrow energy bands [64–67]. Its derivation begins with a general Hamiltonian for electrons in a crystal,

$$H = \sum_i \left[\frac{p^2}{2m} + V(\mathbf{r}_i) \right] + \frac{1}{2} \sum_{ij} \frac{e^2}{|\mathbf{r}_i - \mathbf{r}_j|}, \tag{2.11}$$

consisting of a kinetic energy term for the moving electrons, the potential V felt by each electron on the crystal ion lattice and the Coulomb interaction between pairs of electrons at positions $\mathbf{r}_i, \mathbf{r}_j$, where m and e are the electron mass and charge. Switching then to a second quantized notation — better suiting the many-body problem — the Hamiltonian becomes

$$H = -\sum_{i,j,\sigma} T_{ij} c^\dagger_{i\sigma} c_{j\sigma} + \sum_{ijkl} \sum_{\sigma\sigma'} U_{ijkl} c^\dagger_{i\sigma} c^\dagger_{j\sigma'} c_{k\sigma'} c_{l\sigma}, \tag{2.12}$$

with $c^\dagger_{i\sigma}$ ($c_{i\sigma}$) the creation (annihilation) operator of an electron with spin $\sigma \in \{\uparrow, \downarrow\}$ at site i, following the usual fermionic anti-commutation relations

$$\{c_{i\sigma}, c^\dagger_{j\sigma'}\} = \delta_{ij}\delta_{\sigma\sigma'}, \quad \{c_{i\sigma}, c_{j\sigma'}\} = \{c^\dagger_{i\sigma}, c^\dagger_{j\sigma'}\} = 0. \tag{2.13}$$

The coefficients in (2.12) relate to the terms in (2.11) through the Wannier wave functions $\phi(\mathbf{r} - \mathbf{R}_i)$ representing an electron orbital centered on the i-th lattice site, by means of the following integrals

$$T_{ij} = -\int d\mathbf{r} \; \phi^*(\mathbf{r} - \mathbf{R}_i) \left[\frac{p^2}{2m} + V(\mathbf{r}) \right] \phi(\mathbf{r} - \mathbf{R}_j) \tag{2.14}$$

and

$$U_{ijkl} = \int\int d\mathbf{r}d\mathbf{r}' \phi^*(\mathbf{r} - \mathbf{R}_i)\phi^*(\mathbf{r}' - \mathbf{R}_j) \frac{e^2}{|\mathbf{r} - \mathbf{r}'|} \phi(\mathbf{r}' - \mathbf{R}_k)\phi(\mathbf{r} - \mathbf{R}_l). \tag{2.15}$$

Last, to arrive at the Fermi-Hubbard Hamiltonian, one assumes in (2.12) that the only significant contributions are the ones in T_{ij} corresponding to nearest neighbors and the ones in U_{ijkl} for electrons on the same site (U_{iiii}) and thus with opposite spin. This approximation leaves us with the Fermi-Hubbard Hamiltonian

$$H = -t \sum_{\langle i,j \rangle, \sigma} (c^\dagger_{i\sigma} c_{j\sigma} + \text{h.c.}) + U \sum_i n_{i\uparrow} n_{i\downarrow}, \tag{2.16}$$

where $n_{i\sigma} = c^\dagger_{i\sigma} c_{i\sigma}$ is the so-called number operator and h.c. denotes the hermitian conjugate. Thus, in this model we recognize two terms: a first term accounting for the hopping of fermions to neighboring sites governed by the tunneling strength t, and an

---

the companies TOPTICA Photonics AG, Robert Bosch GmbH and Covestro Deutschland AG.

on-site interaction term governed by the parameter U. While the hopping term always contributes to a reduction of energy (negative sign), the on-site interactions will penalize or contribute to it depending on whether we consider the repulsive ($U > 0$) or attractive ($U < 0$) regime, respectively. In this thesis, we will be interested in the repulsive case.

Despite the simplifications it contains, the Fermi-Hubbard model (2.16) has proven itself as a powerful tool for investigating strongly-correlated electron physics, which is key for understanding the electronic properties of materials such as high temperature cuprate superconductors. From a theoretical point of view, the presence of metallic, insulating, ferro- and antiferromagnetic, superconducting, and charge-ordered phases in a model with very few parameters has proven an appealing test bed for new analytical methods. However, it became clear early on that the analytical tool kit of condensed matter theory was insufficient to describe the rich physics to the desired accuracy, since an exact solution for this Hamiltonian only exist under special circumstances[5], thus leaving various of its crucial properties unununderstood. This triggered the development of a wide range of numerical tools based on many different approximations and approaches, including diagonalization, diagrammatics, tensor network, variational, series expansion, Monte Carlo and embedding methods [36, 37, 70]. On the other hand, the simplicity of the model has made it an ideal target for early quantum simulators [31, 71–76], where quantum many-body phenomena can be studied without many of the hurdles present in realistic condensed matter systems and could thus perhaps show a quantum advantage with respect to numerical methods.

2.3.2 FermiQP Experiment

Among the different platforms for analog fermionic quantum simulation, neutral atoms in optical lattices are particularly promising. These are capable of realizing the Fermi-Hubbard Hamiltonian (2.16) by synthetically reproducing the crystal structure of a material with a two-dimensional optical lattice of interfering laser beams (see Fig. 2.1a). These create a periodic potential where loaded neutral ultracold[6] atoms can either stay at the sinks of the wells where energy is minimal, or hop two a neighboring well by a tunneling process provided the energy barrier is low enough. The presence of a magnetic field given by a Feshbach resonance effectively induces an on-site interaction.

These platforms offer easy scalability with several thousands of fermionic modes with long coherent evolution times, making them a natural frontier to search for a practical quantum advantage relative to classical simulations [77]. However, they often lack the

---

[5] Indeed, alone determining the ground state of the two-dimensional Fermi-Hubbard model is known to be an NP-hard problem [68]. More generally, the k-local Hamiltonian problem for $k \geq 2$ is QMA-complete, i.e. QMA-hard and in QMA [69]. NP is the set of decision problems verifiable in polynomial time by a deterministic Turing machine, while QMA problems are those having a polynomial-size quantum proof convincing a polynomial time quantum verifier of this fact with high probability.

[6] *Ultracold* designates that atoms are slowed down by a magneto-optical trap (MOT) localizing particles in both position and momentum (laser cooling). This reduction of the particle's thermal energy corresponds to an atomic temperature in the scale of μK, which can be further cooled down to nK by other experimental techniques, leaving the particles at almost absolute zero temperature.

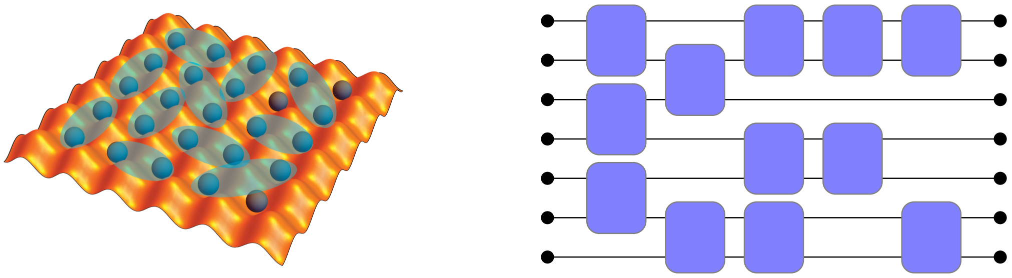

(a) Particles on a 2D optical lattice.

(b) Digital gate operations.

Figure 2.1: Hybrid programmable quantum simulator. (a) The Fermi-Hubbard model can be realized in an analog mode by synthetically reproducing the crystal structure of a material with a two-dimensional optical lattice of interfering laser beams. (b) FermiQP combines this with the capability of performing gate operations in a fault-tolerant digital mode. Reproduced with permission of the FermiQP team.

flexible state initialization tools that digital universal gate sets provide. Moreover, they only have access to the specific models for which the Hamiltonian can be directly realized and not beyond, while the digital form (Fig. 2.1b) allows for performing error correction on imperfect implementation of the gates.

The FermiQP project on a fermionic quantum processor combines these advantages of both analog and digital simulation in realizing a new and scalable hybrid platform based on ^{6}Li lithium isotopes. While the time evolution of the Fermi-Hubbard Hamiltonian and generalizations of it can be observed natively in the analog mode, its universality when including additional site- and spin-dependent chemical potentials [78] can be employed for digital quantum computation[7], in particular aiding the analog mode in state initialization schemes. Fermionic particles can be both locally manipulated and entangled among them by being moved around the lattice with optical tweezers providing full connectivity of the processor, together with microwave-pulse induced spin-flips and by taking advantage of the superlattice tunability [79]. Spin- and site-resolved measurements can be taken by means of a quantum gas microscope [80]. Thus, the dynamics of the analog quantum simulator implementing highly entangling operations on all of the particles with time-dependent control, can be combined with digital operations leading to a programmable fermionic quantum simulator.

The present work is the result of a collaboration with experimentalists Dr. Philipp Preiss and Dr. Timon Hilker, led by Prof. Dr. Ignacio Cirac and in a joint work with Dr. Luis Escalera and M.Sc. Benjamin Schiffer at the Theory Division, on a proposal for a quantum algorithm exploiting the capabilities of the fermionic quantum processor.

---

[7] Note further that the terms in the universal gate set (2.7) from [43] correspond to Hamiltonian evolutions e^{-iHt} for specified times t and Hamiltonians H respectively given by a chemical potential $\mu_j n_j$, 2-body interaction $U_{ij} n_i n_j$ or tunneling term $t_{ij}(c_i^\dagger c_j + \text{h.c.})$, similar to the spinful versions appearing in the Fermi-Hubbard (2.16) with extra chemical potential.

Chapter 3

Finite Energy Algorithm for the 2D Fermi-Hubbard model

The present chapter containing the main results of this thesis describes a hybrid algorithm that exploits the capabilities of the fermionic quantum processor at disposal to study uncharted regions in the phase diagram of the 2D Fermi-Hubbard model.

3.1 Motivation

To motivate the interest of this algorithm, we start by commenting on the phase diagram of the repulsive single-band Fermi-Hubbard model on a two-dimensional square lattice

$$H = -t \sum_{\langle i,j \rangle,\sigma} (c^{\dagger}_{i\sigma} c_{j\sigma} + \text{h.c.}) + U \sum_{i} n_{i\uparrow} n_{i\downarrow}, \quad U > 0, \tag{3.1}$$

at intermediate to strong coupling U/t as shown in Fig. 3.1, where multiple regions corresponding each to a different physical behavior of the collective system are illustrated as a function of temperature and doping.[1]

First we recall some definitions. To begin with, the density or *filling* of particles on a lattice of size N is given by $\langle n \rangle = (N_{\uparrow} + N_{\downarrow})/N$, where N_{σ} is the number of particles in the system with spin $\sigma \in \{\uparrow, \downarrow\}$. At *half filling*, when the lattice contains half of the particles it can hold, one has $\langle n \rangle = 1$. Yet the word is oftentimes reserved for the symmetric case on which we focus in this work, where $N/2$ particles of each species are present. The *doping* is in any case defined as the deviation from half filling, i.e. $x = 1 - \langle n \rangle$.

Coming back to the phase diagram in Fig. 3.1, one sees for instance how the system at zero temperature changes from a conductor (metal phase) to a complete band insulator (antiferromagnet phase) as the doping is decreased down to zero. In between, the system traverses through a different phase known as the pseudogap, characterised by a suppression of the density of states near the antinode $(0, \pi)$ in the Brillouin zone but not near the node $(\pi/2, \pi/2)$, resulting in a closing of the energy gap for specific points

---

[1] Note that the phase diagram is a qualitative one. Although the ground-state phase diagram of the model at weak coupling is fairly well understood, the phase diagram in the intermediate to strong interaction limit is still debated. Correspondingly, though a broad consensus exists on the phases and their approximate locations, the precise shape of the transition lines is often not known.

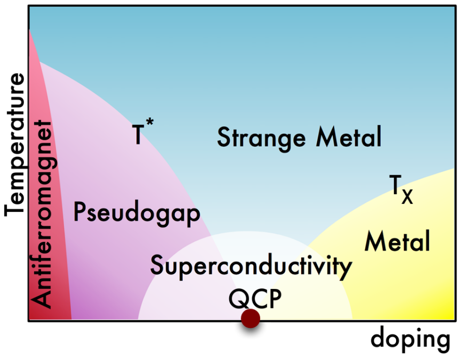

Figure 3.1: Temperature-resolved phase diagram of the 2D Fermi-Hubbard model as a function of doping at intermediate interaction strength U/t. Reprinted from Galanakis et al. [82].

in momentum space only while opening for others. This effect can readily be observed through the spectral function $A(\mathbf{k}, \omega)$ at $\mathbf{k} = (0, \pi)$ e.g. in Fig. 4a of [81], where the peak at zero energy (Fermi level) appearing in the conducting phase starts to show a null at $\omega = 0$ when decreasing doping, meaning the pseudogap is opening. This pseudogap phase, as well as the metal and antiferromagnet phases, persists for finite temperatures up to some critical value depending on doping, leading beyond to a strange metal phase.

In order to better understand these phases capturing the physics of the Fermi-Hubbard model, one aims to simulate the system and extract information on observables characterizing the states within that regime, such as the already mentioned spectral function. Main static quantities of interest are typically ground-state and finite-temperature expectation values of energies and entropies, as well as spin and charge correlation functions or pairing. Also interesting are well-defined short-ranged magnetic fluctuations, since according to Qin et al. [81] they lead to the opening of the pseudogap. Considerably more challenging are the numerical calculations of dynamical (i.e. frequency-dependent) results. For instance, resolving the full frequency and momentum dependence of the spectral function in the Brillouin zone is a difficult outstanding problem for classical computers. Results from cluster dynamical mean-field theory are available at selected momentum points or averaged over small areas in momentum space, but extracting the detailed momentum dependence and Fermi surface shape yields results that strongly depend on the periodization schemes employed [81].

While extracting such information on observables with classical methods is computationally demanding already for small system sizes, directly accessing the pseudogap on the experimental side is challenging for low temperatures due to a limitation on the amount of entropy that can be removed from the system. Hence, an alternative method to study the pseudogap or other phases of the 2D Fermi-Hubbard model with a quantum simulator, but without having to actually access them directly in experiments, would be interesting and valuable.

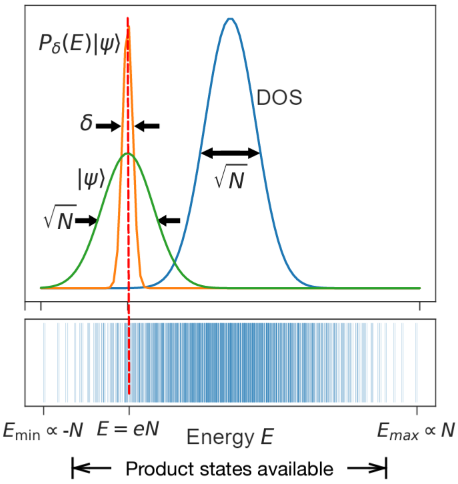

Figure 3.2: The algorithm computes properties of a state with narrow energy variance (schematical spectral distribution shown in orange), which would result from applying a filter $P_\delta(E)$ onto an easy to prepare state $|\psi\rangle$, e.g. a product state (green curve). For local Hamiltonians such as the Fermi-Hubbard model, for which the density of states in the thermodynamic limit approaches a Gaussian distribution of width proportional to $\sqrt{N}$ (blue curve), the accessible energy densities can lie on the tails of the spectrum. The box under the graph sketches the energy spectrum of a model H for a given system size N. Adapted from Lu et al. [83].

Such a method is what the present work aims to provide by proposing a concrete hybrid quantum-classical algorithm mainly relying on the results in [83, 84]. In [83], two proposals to efficiently retrieve microcanonical and canonical properties for many-body systems are presented. We focus here on the first one, providing an algorithm to compute expectation values of observables in a finite energy interval around the mean energy of a given easy-to-prepare[2] initial state. It is based on a filtering operator projecting out the energies outside the desired energy interval (see Fig. 3.2), yet it avoids the actual preparation of the filtered state by recovering the physical values of interest from interferometric measurements. The result relies on being able to determine specific Loschmidt echos for the easy-to-prepare state by using a quantum simulator (FermiQP in the present work). To completely determine the phase of these complex numbers, the result in [84] involving a short imaginary time evolution is further employed, while providing a concrete way of implementing it in the given quantum processor.[3]

---

[2] That is, an efficiently preparable state $|\psi\rangle$ on N qubits, meaning that for any prescribed error $\epsilon > 0$ one is able to prepare a state $|\varphi\rangle$ with $\||\psi\rangle - |\varphi\rangle\| < \epsilon$ in a time $T = \text{poly}(N, 1/\epsilon)$.

[3] Note that, unlike in results relying on the eigenstate thermalization hypothesis (ETH) [85, 86] — where one expects eigenstates to thermalize with time, but without knowing how long it requires to do so —, this protocol provides *certified* finite energy quantum simulation in the sense that the thermal state is truly targeted.

3.2 Virtual Filtering

We start by introducing in detail the mentioned algorithm as proposed in [83]. The choice of the suitable initial state to be virtually filtered and the key ingredient consisting in the ability of retrieving Loschmidt echos from the quantum simulator will be further analyzed in the subsequent sections.

3.2.1 Setup and cosine filter

Following Lu et al. [83], we consider a local Hamiltonian on N sites

$$H = \sum_{j=1}^{N} h_j, \tag{3.2}$$

given in our case by — but not restricted to — the Fermi-Hubbard model (3.1) where each local term

$$h_j = \sum_{\sigma} \sum_{i:\langle i,j \rangle} c^{\dagger}_{i\sigma} c_{j\sigma} + U n_{j\uparrow} n_{j\downarrow} \tag{3.3}$$

acts on the j-th site and its nearest neighbors in the lattice only. The main requirement is that the evolution e^{-iHt} generated by H can be efficiently implemented with the quantum simulator, which is indeed the case for the FermiQP platform in e.g. the analog mode. More precisely, one requires the quantum simulator to be able to efficiently determine

$$\begin{aligned} a_{\psi}(t) &= \langle \psi | e^{-iHt} | \psi \rangle, && (3.4)\\ a_{A,\psi}(t) &= \langle \psi | A e^{-iHt} | \psi \rangle, && (3.5)\\ a_{\psi,A}(t) &= \langle \psi | e^{-iHt} A | \psi \rangle, && (3.6) \end{aligned}$$

with a sufficiently small error, for given initial state $|\psi\rangle$ and observable A. Each of these quantities (3.4) is called a Loschmidt echo. It provides the complex overlap between the state $|\psi\rangle$ before and after a Hamiltonian evolution, i.e. how close does $e^{-iHt}|\psi\rangle$ get back to the initial state $|\psi\rangle$ after a time t.[4]

On the other hand, we introduce the cosine-filtering operator [87]

$$P_{\delta}(E) = \left[\cos\left(\frac{H - E}{N} \right) \right]^{\lfloor N^2/\delta^2 \rfloor_2} \tag{3.7}$$

---

[4] Note, however, that the word *Loschmidt echo* commonly refers in the literature to $\langle \psi | e^{-i(-H_2)t} e^{-iH_1 t} | \psi \rangle$, which provides a measure of the revival occurring when an imperfect time-reversal procedure is applied to a complex quantum system, allowing to quantify the sensitivity of quantum evolution to perturbations. The backwards evolution to $e^{-iH_1 t}|\psi\rangle$ is implemented by the (erroneous) Hamiltonian $-H_2$, which would yield a perfect recovery of the initial state if H_2 would be equal to H_1 (generally not possible in realistic setups).

where $\lfloor ... \rfloor_2$ denotes the nearest even integer and $\delta > 0$ is a parameter that can take arbitrary values[5]. To better interpret the action of this operator, the following approximation [87] can be considered[6]

$$P_\delta(E) \simeq e^{-(H-E)^2/2\delta^2}, \tag{3.8}$$

where it is clear that it basically projects out the eigenstates $|E'\rangle$ of H with energy $|E'-E| \gg \delta$, while keeping the ones within $[E-\delta, E+\delta]$ (where $P_\delta(E) \simeq \mathbb{1}$), acting thus as a filter around E. Further, one can express (3.8) as a Gaussian integral or Fourier transform $e^{-(H-E)^2/2\delta^2} = \int dt e^{-t^2\delta^2/2} e^{iEt} e^{-iHt}$ and approximate it by a finite sum

$$P_\delta(E) \simeq \sum_{m=-R}^{R} b_m e^{-i(H-E)t_m} \tag{3.9}$$

evaluated at times $t_m = 2m/N$ covering up to the tails lying at $\pm t_R$, with cutoff $R = xN/\delta \in \mathbb{N}$ and coefficients

$$b_m = \frac{1}{2^M} \binom{M}{M/2-m} \tag{3.10}$$

with $M = \lfloor N^2/\delta^2 \rfloor_2$. This leaves us with an expression for the filtering operator expanded in terms of the evolution operator e^{-iHt}, which is hard to simulate efficiently for classical computers but easy for quantum simulators.

The idea of the algorithm [83] is to apply the operator $P_\delta(E)$ to a specific initial state $|\psi\rangle$ to filter it around some energy of interest E (see Fig. 3.2), and then obtain expectation values of observables at the resulting state $P_\delta(E)|\psi\rangle$. However, instead of preparing such filtered state, the desired values are first expressed in terms of the Loschmidt echos (3.4, 3.5, 3.6), which are then retrieved from the quantum simulator separately. The number of measurements will be $2R$ times the number of repetitions required to obtain a prescribed accuracy, and each of the runs of the simulator will last for a time $t \leq 2x/\delta$. The protocol ends with a classical post-processing task.

3.2.2 Efficient quantum algorithm for observables at finite energy

Recall that given a state $|\psi\rangle = \sum_n c_n |E_n\rangle$ expressed in the eigenbasis of the Hamiltonian H, the expectation value of an observable A in the normalized state $|\psi\rangle$ is given by

$$\langle A \rangle_\psi \equiv \langle \psi | A | \psi \rangle = \sum_{m,n} c_m^* c_n \langle E_m | A | E_n \rangle, \tag{3.11}$$

with $c_n = \langle \psi | E_n \rangle \in \mathbb{C}$ the overlap of the state with each eigenvector. Note that such an expectation value involves the whole energy spectrum $\{E_n\}_n$ of H. Instead, we will

---

[5] This includes any scaling with N, such as decreasing e.g. $\delta \sim 1/N$.

[6] The approximation is valid as long as the argument in the cosine is an operator with spectrum lying in the interval $[-\pi/2, \pi/2]$. For the Fermi-Hubbard model (3.1), this can be achieved by simultaneously decreasing the parameters t and U to lower frequencies, shrinking the spectrum at desire while preserving the relevant ratio U/t.

consider expectation values related to the microcanonical quantum statistical ensemble, i.e. for a specific energy E. More precisely, we will consider a small interval around that energy, $[E-\delta, E+\delta]$, and compute the expectation value of the observable A not at the state $|\psi\rangle$ but at the state filtered within that energy range, i.e. involving only the eigenstates in its decomposition with energy lying in that interval. This quantity may be defined by means of the filtering operator (3.7) through either of the following expressions

$$A_{\delta,\psi}(E) := \frac{\langle\psi|[AP_\delta(E)+P_\delta(E)A]|\psi\rangle}{2\langle\psi|P_\delta(E)|\psi\rangle} \tag{3.12}$$

$$A'_{\delta,\psi}(E) := \frac{\langle\psi|P_\delta(E)AP_\delta(E)|\psi\rangle}{\langle\psi|P_\delta(E)^2|\psi\rangle} \tag{3.13}$$

related to the microcanonical expectation value of A.[7] In particular, if $|\psi\rangle$ has non-zero overlap $\langle\psi|E\rangle \neq 0$ with an eigenstate of H with energy E, the expression (3.13) converges to that value in the limit $\delta \to 0$.[8]

Obtaining $A_{\delta,\psi}(E)$ is relevant because the actual microcanonical expectation value of A can be recovered in the limit $\delta \to 0$ from $A_\delta(E) = \frac{\mathrm{Tr}[AP_\delta(E)]}{\mathrm{Tr}[P_\delta(E)]}$, an expression that can be rewritten as[9]

$$A_\delta(E) = \frac{\int d\mu_\psi D_{\delta,\psi}(E) A_{\delta,\psi}(E)}{\int d\mu_\psi D_{\delta,\psi}(E)}, \tag{3.14}$$

— with $D_{\delta,\psi}(E) = \langle\psi|P_\delta(E)|\psi\rangle$ a broadened version of the local density of states —, which can thus be computed using Monte Carlo algorithms as long as one is able to compute $D_{\delta,\psi}(E)$ and $A_{\delta,\psi}(E)$, which is what we discuss in the present work.

Crucially, these generalized microcanonical expectation values (3.12, 3.13) can be expressed in terms of Loschmidt echos when introducing (3.9) for $P_\delta(E)$ in both numerator and denominator, yielding for Eq. (3.12)

$$D_{\delta,\psi}(E) \equiv \langle\psi|P_\delta(E)|\psi\rangle \simeq \langle\psi|\sum_{m=-R}^{R} b_m e^{-i(H-E)t_m}|\psi\rangle = \sum_{m=-R}^{R} b_m e^{iEt_m} a_\psi(t_m),$$

$$\langle\psi|[AP_\delta(E)+P_\delta(E)A]|\psi\rangle \simeq \sum_{m=-R}^{R} b_m e^{iEt_m} a_{A,\psi}(t_m) + \sum_{m=-R}^{R} b_m e^{iEt_m} a_{\psi,A}(t_m), \tag{3.15}$$

which are simply linear combinations of the Loschmidt echos (3.4, 3.5, 3.6) with known coefficients $b_m e^{iEt_m}$.[10] Thus, the protocol consists of a hybrid quantum-classical algo-

---

[7] Note that (3.13) is nothing else than the expectation value of A at the filtered state $P_\delta(E)|\psi\rangle$ with norm squared being $\langle\psi|P_\delta(E)^2|\psi\rangle$.

[8] Note that in this limit $\delta \to 0$, then $R \to \infty$ in (3.9), leaving an infinite sum of exponentials reminding us of a representation of the delta function $\delta(H-E)$, retrieving only the microcanonical information at energy E. On the other hand, when $\delta \to \infty$, then $P_\delta(E) \to \mathbb{1}$ in (3.8) becomes flat recovering the whole spectrum of H, leading to $A_{\delta,\psi}(E) \to \langle A\rangle_\psi$.

[9] Here $d\mu_\psi$ is a measure in the basis set (see [83]).

[10] Note that, being able to measure (3.4, 3.5), one has also access to the terms $a_{A,\psi}(t_1,t_2) = \langle\psi|e^{iHt_1}Ae^{-iHt_2}|\psi\rangle$ that appear in the numerator of (3.13), since $a_{A,\psi}(t_1,t_2) = a_{A,\psi(t_1)}(t_2-t_1)$. Further, $a_{\psi,A}(t_m)$ can also be written as $a_{A,\psi}(-t_m,0)$ and thus obtained from (3.4, 3.5).

rithm, where the quantum simulator is used to determine the Loschmidt echos up to the required precision, which are then multiplied with the classically computed b_m and $\exp(iEt_m)$ factors and summed together, before performing the final division between numerator and denominator (classical post-processing).

The quantum simulator will be able to efficiently measure A provided it can perform measurements to obtain the Loschmidt echos (3.4, 3.5, 3.6) at time t with an error smaller than $\epsilon > 0$ in a time $T = \text{poly}(N, t, 1/\epsilon)$. This basically requires an efficient procedure to evolve under the Hamiltonian H (available in the analog mode of FermiQP) and the possibility of performing interferometric measurements (which we discuss in the next section). Then, if the quantum simulator is able to efficiently prepare[11] $|\psi\rangle$ and measure A, Lu et al. [83] show that for any $\epsilon, \delta > 0$ one can always find $E \in [E_\psi - r\sigma_\psi, E_\psi + r\sigma_\psi]$ with $r = [3\log[2(1 + 2\sigma_\psi^2/\delta^2)]]^{1/2}$, so that one can obtain (3.12, 3.13) up to an additive error ϵ in a time $T = \text{poly}(N, 1/\delta, 1/\epsilon)$.

3.3 Selection of Initial State

Having now discussed the proposed algorithm relying on the virtual filtering of a suitable initial state $|\psi\rangle$, we proceed now to discuss the selection of such a state in the case of the Fermi-Hubbard Hamiltonian (3.1) and explore possible state preparation schemes. While one is typically interested in calculating properties of the lowest-energy states or specific excited states of the quantum system, most important here is that such a state needs to have a significant overlap with the energy window of interest onto which the state will be virtually filtered — as described in the previous section — in order for the algorithm to provide information within a reasonable amount of measurements (see Fig. 3.2, where green and orange distributions overlap). With this in mind, we seek for low energy states that are efficiently preparable on the FermiQP quantum simulator.

3.3.1 iPEPS benchmarks

We begin by learning the ground state energy density e_0 for the Fermi-Hubbard model on an infinite grid system (see Fig. 3.3) from iPEPS[12] results. This serves as a benchmark for understanding how close in energy are the initial states we aim to propose to the true ground state of the system. From [36, 88] we find out the following filling-dependent results in the limit of zero temperature or infinite bond dimension χ (i.e. zero truncation error w) at the $U/t = 8$ regime:

- At half filling, $\langle n\rangle = 1$: $e_0/t \simeq -0.52$.
- With doping, $\langle n\rangle = 0.875$: $e_0/t \simeq -0.76$.

---

[11] Recall that efficiently preparing a state $|\psi\rangle$ means that for any prescribed error $\epsilon > 0$ one is able to prepare a state $|\varphi\rangle$ with $\||\psi\rangle - |\varphi\rangle\| < \epsilon$ in a time $T = \text{poly}(N, 1/\epsilon)$.

[12] This is a 2D tensor network method for infinite spatially extending systems which can provide estimations on ground state energies by extrapolating numerical results to zero truncation error. The name iPEPS stands for “infinite projected entangled pair states”.

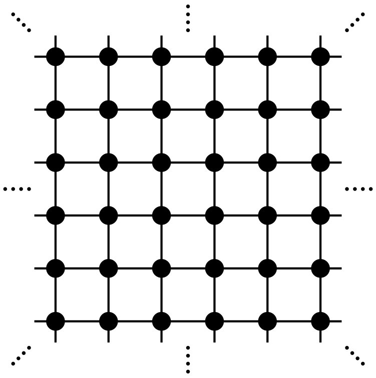

Figure 3.3: Infinitely extending square grid on which the 2D Fermi-Hubbard model is defined, where particles are allowed to hop between neighboring sites.

These numbers will serve as reference for the selection of low-energy lying initial states. We will mainly focus on the half filled case within the scope of this thesis, leaving the doped case for future investigations.

3.3.2 Plaquette states

Now we address the question on which initial states $|\psi\rangle$ to choose for the simulation algorithm to be efficient in accessing finite energies of the 2D Fermi-Hubbard Hamiltonian H on N sites. Since H is local, we know that if $|\psi\rangle$ has finite correlation length, both its mean energy $E_\psi = \langle\psi|H|\psi\rangle$ and variance $\sigma_\psi^2 = \langle\psi|(H - E_\psi)^2|\psi\rangle$ will scale as N. The simplest states to consider, then, would be product states $|p\rangle$, e.g. Fock states. However, their mean energy E_p won't cover the full spectrum of H, but just an interval $[E_{p,\min}, E_{p,\max}]$.[13] In order to efficiently explore energies with the algorithm in [83] lying beyond this interval (specially the low energy spectrum), one thus needs to consider slightly more complex states $|\psi\rangle$ that are still efficient to prepare.

A possibility is to propose the following family of states: plaquettes that repeat homogeneously over the lattice[14] as in Fig. 3.4. On each plaquette, the ground state at half filling is considered, leading to an overall half filled state as well.[15]

Comparing this state to the true ground state at half filling on the N-site lattice — which will in general be a highly complex state with entanglement between all pairs of neighboring sites —, we notice that in the state defined as product of plaquettes we are missing the entanglement between the decoupled plaquettes, leading to an increase in

---

[13] Which is clearly extensive in N for local Hamiltonians H.

[14] Note that, although these decoupled plaquette states $|\psi\rangle$ alone might be too simple to recover any physics of the Fermi-Hubbard model, information about the whole lattice physics will be extracted from its dynamics $e^{-iHt}|\psi\rangle$, where the Hamiltonian time evolution entangles plaquettes together.

[15] Note, however, that a doped state could be achieved by considering an inhomogeneous product of plaquettes, each plaquette having a different number of particles (i.e. different dopings within the plaquettes leading to an overall doping in the overall state).

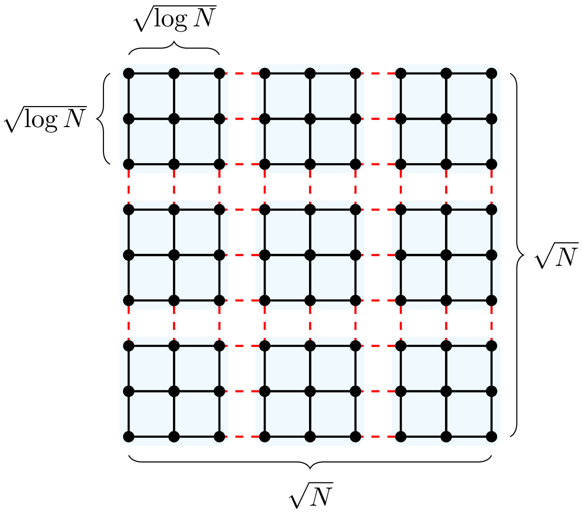

Figure 3.4: Visualization of a state defined on a $\sqrt{N} \times \sqrt{N}$ lattice with N sites and given by the product of $\sqrt{\log N} \times \sqrt{\log N}$ plaquettes. Red dashed lines represent the missing entanglement in this state in comparison to the ground state.

energy above the ground state. The larger the plaquettes, the less entangled sites we omit and thus the closer we are to the ground state energy. However, this is at the expense of having to prepare larger plaquettes efficiently, which becomes challenging.

Now, if the plaquettes on the system of size N are taken to be of size $\sqrt{\log N} \times \sqrt{\log N}$ (as depicted in Fig. 3.4), the number of sites of the plaquette will then be $\log N$ and so the number of basis states in the plaquette $2^{\log N} = N$, i.e. linear in N and not exponential. Further, the energy density $e = E/N$ of the state defined as the product of each plaquette ground state, $e_p(N)$, will then differ from the one of the true ground state, $e_0(N)$, by $\Delta e(N) = \frac{c}{\sqrt{\log N}}$, for some constant $c \in \mathbb{R}$. That is, $e_p(N)$ and $e_0(N)$ will get closer and closer for increasing N, meaning that the larger $\sqrt{\log N} \times \sqrt{\log N}$ plaquettes better approximate the true ground state of the system. Note that $e_0(N) < 0$ is decreasing in N but converges to the iPEPS benchmark result e_∞ from [88] corresponding to an infinite lattice, while $e_p(N) < 0$ approaches from above (see Fig. 3.5). We might as well directly compare each energy density $e_p(N)$ for increasing system sizes N with the one from iPEPS, e_∞, and observe how they converge to that limiting value.

Proof. Regarding the claimed scaling for $\Delta e(N)$, we show how it can be obtained by counting the density of violated bonds in Fig. 3.4 (red lines) as follows. To begin with, the number of plaquettes is given by the number of sites in the lattice, N, divided by the size of the plaquettes, $\log N$, i.e. $N/\log N$. Thus, the number of plaquettes per row is $\sqrt{N/\log N}$. With this we can count the number of violations: we have $\sqrt{N}$ pairs of horizontal violated edges (red) per column, over $\sqrt{N/\log N} - 1$ columns, and the same holds for rows, yielding $\sqrt{N}(\frac{\sqrt{N}}{\sqrt{\log N}} - 1) \cdot 2 = \mathcal{O}(\frac{N}{\sqrt{\log N}})$ violated edges. On the other

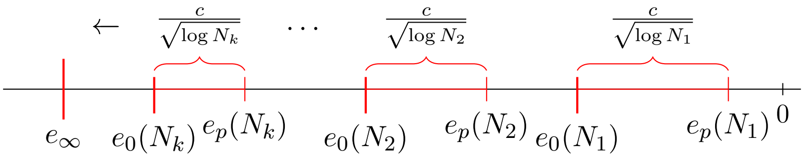

Figure 3.5: Sketch on the scaling $\Delta e(N) = \mathcal{O}(\frac{1}{\sqrt{\log N}})$ for the difference in energy density between the ground state of an N-site lattice, $e_0(N)$, and the product of $\sqrt{\log N} \times \sqrt{\log N}$ plaquette ground states on it, $e_p(N)$. While $e_0(N) < 0$ decreases in N to the iPEPS result e_∞ for infinite system size (left), the $e_p(N) < 0$ approaches rapidly from above (right) due to the scaling.

hand, the total number of edges in the lattice can be counted as $\sqrt{N} - 1$ columns of $\sqrt{N}$ horizontal edges each and the same number holding for rows with vertical edges, yielding $(\sqrt{N} - 1)\sqrt{N} \cdot 2 = \mathcal{O}(N)$ edges in the lattice. Putting both results together, we have a density of violations of $\mathcal{O}(\frac{1}{\sqrt{\log N}})$, computed as the number of violated edges over the total number of edges. For each violated bond we get an extra energy term above the ground state of the large $\sqrt{N} \times \sqrt{N}$ system. Therefore, $\Delta e(N)$ is $\mathcal{O}(\frac{1}{\sqrt{\log N}})$, as claimed. □

Thus, as already mentioned, by increasing N one approaches with $e_p(N)$ the ground state energy density $e_0(N)$ by $\Delta e(N) = \frac{c}{\sqrt{\log N}}$. The question is how large the constant $c \in \mathbb{R}$ is; i.e. given a system size N, how far away is one from the true ground state energy density $e_0(N)$ if instead the $\sqrt{\log N} \times \sqrt{\log N}$ plaquette product state with energy density $e_p(N)$ is considered. For this reason, we next compute numerically the energy density for different product-of-plaquette states.

First we note the following property that the energy density of such a uniform product of plaquettes coincides with the energy density of a single plaquette provided that its particle number of each species is fixed. This can be understood by noticing that there are no energy contributions from the Hamiltonian hopping terms between decoupled plaquettes — i.e.[16] $\langle\psi|h_{ij}^{\sigma}|\psi\rangle = 0$ for all neighboring $i \in P, j \in P'$ in decoupled plaquettes $P \cap P' = \emptyset$ — provided the state $|\psi\rangle$ has a definite particle number of each species $(u_P \uparrow, d_P \downarrow)$, $u_P, d_P \in \mathbb{N}$, in each plaquette P. The reason is that the product-of-plaquettes state $|\psi\rangle = |..., (u_P, d_P), (u_{P'}, d_{P'}), ...\rangle$ will be orthogonal to the "hopped" state $h_{ij}^{\sigma}|\psi\rangle$ in having an additional (respectively missing) particle on each plaquette, such that the overlap with $|\psi\rangle$ will vanish: $\langle\psi|h_{ij}^{\sigma}|\psi\rangle = 0$. This means we can compute the energy density of the proposed state homogeneously defined over disjoint plaquettes simply as the energy density of a single plaquette.[17]

---

[16] We denote here $h_{ij}^{\sigma} \equiv c_{i\sigma}^{\dagger} c_{j\sigma} + \text{h.c.}$ as the hopping operator term appearing in the Hamiltonian for neighboring sites $\langle i, j\rangle$ and spin $\sigma \in \{\uparrow, \downarrow\}$.

[17] In the doped case where one would consider the product of different plaquettes $A, B, C...$ with different particle number (different doping) each, the result on vanishing hopping contributions would hold but the energy density would be averaged over the ones within a unit cell ABCD.

$\mathbf{2\times 1}$	**filling**	**doping**	e_0/t
$(1\uparrow,1\downarrow)$	1.000	0.000	-0.2361
$(1\uparrow,0\downarrow)$	0.500	0.500	-0.5000
$(2\uparrow,1\downarrow)$	1.500	-0.500	$+3.5000$

$\mathbf{2\times 2}$	**filling**	**doping**	e_0/t
$\mathbf{(2\uparrow,2\downarrow)}$	**1.000**	**0.000**	$\mathbf{-0.3301}$
$(2\uparrow,1\downarrow)$	0.750	0.250	-0.5811
$(3\uparrow,0\downarrow)$	0.750	0.250	-0.4999
$(1\uparrow,1\downarrow)$	0.500	0.500	-0.8019

$\mathbf{3\times 3}$	**filling**	**doping**	e_0/t
$(4\uparrow,4\downarrow)$	0.889	0.111	-0.5601

Table 3.1: Ground state energy densities e_0/t for the Fermi-Hubbard model, $U/t = 8$, on different lattice sizes and different restricted particle number sectors, specifying their corresponding filling and doping.

With this knowledge at hand, we numerically obtain the energy densities in Table 3.1 via exact diagonalization on the `QuSpin` python package for fermionic systems [89].[18]

According to the previous consideration, these energies also hold for states given by product of plaquettes with such a ground state on each plaquette. Looking at the half filled data (zero doping), we see that for the 2×2 square plaquettes the ground state energy density is at $e_0/t \simeq -0.33$ in units of the tunneling parameter. Given the existing trade-off between larger plaquette sizes to reach lower energy densities and the difficulty in experimentally preparing them, we then focus on studying what we can learn by considering this 2×2 half filled plaquette.[19] Its ground state is given by

$$|\psi_0\rangle = 0.2695(|\uparrow,\uparrow,\downarrow,\downarrow\rangle - |\uparrow,\downarrow,\uparrow,\downarrow\rangle - |\downarrow,\uparrow,\downarrow,\uparrow\rangle + |\downarrow,\downarrow,\uparrow,\uparrow\rangle) - 0.5390(|\uparrow,\downarrow,\downarrow,\uparrow\rangle + |\downarrow,\uparrow,\uparrow,\downarrow\rangle), \tag{3.16}$$

obtained with a `QuSpin` code, where the numbering of sites in the plaquette goes from left to right and from bottom to top, and where fermionic states are defined with the following order:

$$(1,\uparrow) \to \ldots \to (N,\uparrow) \to (1,\downarrow) \to \ldots \to (N,\downarrow). \tag{3.17}$$

Notice that this ground state has indeed no doublons $\uparrow\!\downarrow$, which would penalize the energy with $U > 0$ contributions.

---

[18] Note that beyond system sizes of 3×3, solving the ground state with exact diagonalization becomes already numerically demanding due to the exponential dimension of the Hilbert space. One might then estimate the results with tensor network methods, yet running soon into the same issue in 2D.

[19] However, to show first a proof of principle for this algorithm, one can consider Fock states as (zero energy) initial state, even if they will not have significant overlap with the pseudogap energy regimes.

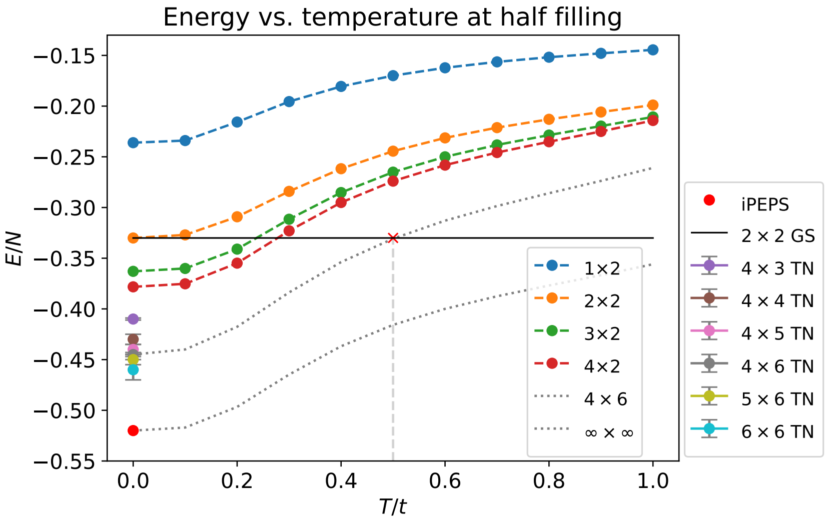

Figure 3.6: Energy density as a function of temperature for half-filled thermal states on different system sizes, with the Fermi-Hubbard model at $U/t = 8$ as Hamiltonian. Additional points from Tensor Network simulations (TN) obtained by Benjamin Schiffer and iPEPS results from [88] are added at zero temperature, together with guessed curves (gray) for qualitative understanding.

3.3.3 Thermal states

In order to understand what information can the latter state given by the product of 2×2 half filled plaquettes provide us, we consider now different thermal states

$$\rho_{\text{th}} = \frac{1}{Z} e^{-\beta H}, \quad Z = \text{Tr}[e^{-\beta H}], \tag{3.18}$$

for different (inverse) temperatures $\beta = 1/T$ and defined on different system sizes, with H being the Fermi-Hubbard Hamiltonian at $U/t = 8$. To specify a half filled thermal state, traces are taken within that restricted basis only. The mean energy of these mixed states is obtained through $E = \text{Tr}[H\rho_{\text{th}}]$, leading to the coloured curves shown in Fig. 3.6. Additional single points at zero temperature (corresponding thus to ground states) obtained by Benjamin Schiffer using tensor network simulations together with the iPEPS benchmark from [88] are added for systems sizes where exact diagonalization is no longer feasible due to the exponential Hilbert space dimension. No curves are obtained for these cases because their classical simulation is too demanding. We add some (gray dotted) curves which are just a guess following the trends in order to conclude some qualitative results. The shape of the curves is consistent with Fig. 12a (blue curve) in [90], where they consider a system size of 4×4 (cylinder MPS). As expected, the energy density increases with temperature. Further, the larger the system size, the lower the energy density. An additional horizontal dark line shows the energy density we are targeting with the 2×2 plaquettes.

We interpret the figure as follows. Let us say we are interested in studying properties of an $m \times n$ system. The ground state energy density of that system will decrease with system size, following the leftmost dots at zero temperature ($T/t = 0$) in Fig. 3.6 till reaching the bottom most point corresponding to infinite system size (iPEPS result). Now, say we consider to fix the choice of state on the big system to be the product of copies of the half-filled 2×2 plaquette ground state (call it pGS), having the same energy density as the individual plaquettes. Then one can look at which thermal state defined on the $m \times n$ system will have the same energy density as our pGS state, which would guarantee the overlap needed for the algorithm as mentioned earlier on.[20] One can do this by looking in Fig. 3.6 at the intersection of the corresponding $m \times n$ curve with the dark line accounting for the fixed energy density. The crossing point (red cross in Fig. 3.6) will tell the temperature of the thermal state one can reach. With the guessed curves, for instance, this would mean a thermal state of around $T/t = 0.5$ on a 4×6 lattice (gray dashed vertical line), where pGS would consist of six 2×2 plaquettes.

Following the dark line in Fig. 3.6 from left to right, one reads that the crossing point moves to the right with increasing system size. This means that the bigger the system one considers the thermal state on, the higher the temperature corresponding to the thermal state will be (and in the limit for very large system sizes, it is unknown whether such a crossing will happen). Thus, if one wants to explore lower temperatures for a given fixed system size $m \times n$, larger enough plaquettes need to be considered to lower the energy density (lower the dark line) to the desired corresponding crossing point.

However, so far only the precise mean energy has been taken into account, which guarantees the overlap if the one for pGS and for the thermal state match. Yet states lying at other energy densities might still have some overlap in their energy distribution with the target energy density. This is precisely what can be seen when looking at the overlap between the true ground state of the 4×2 system and the the product of two 2×2 ground states (all at half filling), shown in Fig. 3.7. One observes an overlap of around 75%, which is considerably large. Certainly, when adding more and more plaquettes, the overlap will rapidly decrease. But what can be learned from here is that one could indeed explore lower temperatures corresponding to a crossing point in Fig. 3.6 with the horizontal dark line lying now at the height of the 4×2 ground state energy density, while actually making use of the 2×2 plaquettes instead — provided they had some overlap with the tail in the energy distribution. This, of course, would be at the expense of needing more measurements depending on the value of said overlap.

On the other hand, one still needs to consider how these energies actually relate to entropy, since from the experimental point of view we know the constraint lies in being currently unable to reach entropies lower than 0.3 (in k_{B} units) for large system sizes. To this respect, qualitative results are obtained next for a better understanding.

In Fig. 3.8 the energy density curves are shown as a function of the von Neumann entropy $S = -\mathrm{Tr}[\rho_{\mathrm{th}} \ln \rho_{\mathrm{th}}]$ for thermal states $\rho_{\mathrm{th}} = e^{-\beta H}/Z$ at half filling and different system sizes, with the temperature data points corresponding to the ones in Fig. 3.6.

---

[20] Note that the overlap between two general quantum states given by density matrices ρ and σ can be measured through the fidelity $F(\rho, \sigma) = \left[\mathrm{Tr}\left(\sqrt{\sqrt{\rho}\,\sigma\sqrt{\rho}}\right)\right]^2$.

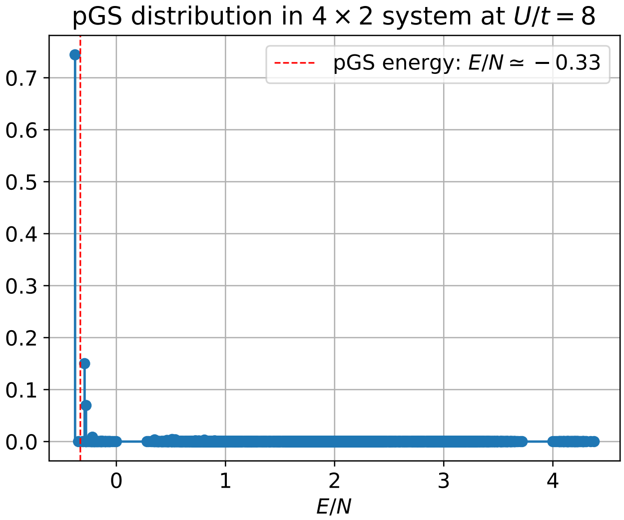

Figure 3.7: Eigenenergy distribution of the product of 2×2 plaquette half-filled ground states (pGS) of the Fermi-Hubbard model at $U/t = 8$, showing a 75% overlap with the ground state of the 4×2 plaquette.

The points at zero entropy correspond to pure states. Again, the curves are guessed (dotted in gray) for larger system sizes following the data trends. Further, we know on the one hand that for a 1×2 lattice, experiments can reliably reach the pure ground state with zero entropy (upper left dark crossed point), while on the other hand one can experimentally only go down to around 0.3 in entropy for larger systems with the current technology (bottom right dark crossed point, where this large system is considered to be infinitely extended in a rough approximation). For intermediate system sizes, we guess by interpolating a decaying exponential curve (dashed-dotted in dark) separating the experimentally forbidden region (red shaded) from the accessible one (green shaded). The filtering algorithm could then be used to virtually filter a state from the green region to one in the red, experimentally forbidden region.

For completeness, the entropy vs. temperature curves are also presented. Fig. 3.9 shows the von Neumann entropy $S = -\mathrm{Tr}[\rho_{\mathrm{th}} \ln \rho_{\mathrm{th}}]$ as a function of temperature for thermal states $\rho_{\mathrm{th}} = e^{-\beta H}/Z$, $\beta = 1/T$, at half filling and different system sizes. Pure states correspond both to zero entropy and to thermal states in the limit of zero temperature, thus collapsing all of them to the point at the origin, regardless of system size. Thermal states at higher temperatures contain larger amounts of entropy, seemingly saturating at some value increasing with system size. The larger the system size, the larger the amount of entropy for a fixed temperature.

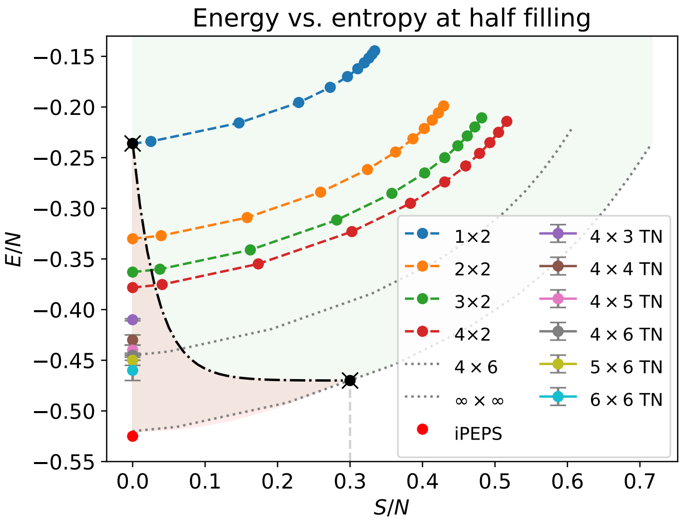

Figure 3.8: Energy density as a function of the von Neumann entropy $S = -\mathrm{Tr}[\rho \ln \rho]$ for half-filled thermal states $\rho = e^{-\beta H}/Z$ on different system sizes for the Fermi-Hubbard Hamiltonian at $U/t = 8$, together with guessed curves (gray) for qualitative understanding. A guessed black curve divides the space into the experimentally accessible (green) and prohibited (red) regions.

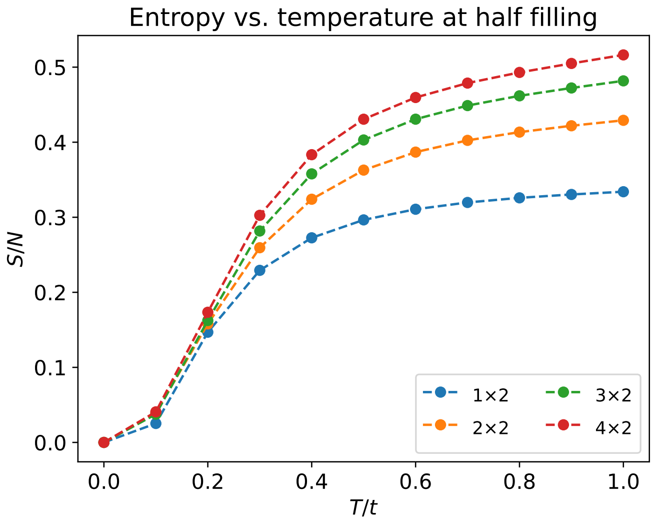

Figure 3.9: Von Neumann entropy $S = -\mathrm{Tr}[\rho \ln \rho]$ as a function of temperature for half-filled thermal states $\rho = e^{-\beta H}/Z$, $\beta = 1/T$, on different system sizes for the Fermi-Hubbard Hamiltonian at $U/t = 8$.

3.3.4 Adiabatic state preparation

A so far missing ingredient to be discussed on the initial state is to propose a protocol on how to prepare it experimentally. One option would be to consider designing a circuit using the available native gate set, which would provide the initial state when applied to e.g. a specific Fock state[21]. An alternative is to propose a path for an adiabatic evolution, since we want to prepare a state that is a ground state of a known Hamiltonian. We focus on the latter possibility and propose two different approaches[22] that seem reasonable for experimental capabilities.

Recall that the quantum adiabatic algorithm [91] provides a procedure for the ground state preparation of a Hamiltonian. The setting is as follows. One considers a path between a trivial Hamiltonian H_0, with known ground state $|\varphi_0(s=0)\rangle$ that is efficiently preparable[23], and the Hamiltonian of interest H_1, whose ground state $|\psi_0\rangle \equiv |\varphi_0(s=1)\rangle$ one aims to obtain:

$$H(s) = (1-s)H_0 + sH_1, \quad s \in [0,1]. \tag{3.19}$$

One can think of (3.19) as a parameter dependent Hamiltonian with physical parameter $s(t)$ varying in time.[24] Note that the initial and final Hamiltonians are then indeed $H(0) = H_0$ and $H(1) = H_1$. Now, the time evolution of the initial state will be governed by the Schrödinger equation

$$i\frac{\partial}{\partial t}|\varphi(s_t)\rangle = H(t)|\varphi(s_t)\rangle, \tag{3.20}$$

with $s_t \equiv s(t)$, written in units such that the Planck constant is set to $\hbar = 1$. From (3.20) follows that the evolution of the initial state $|\varphi(0)\rangle$ will be given by the unitary time evolution operator $\mathcal{U}_{0\to T}$ implementing $|\varphi(0)\rangle \mapsto |\varphi(1)\rangle$ by

$$|\varphi(1)\rangle \equiv |\varphi(s(T))\rangle = e^{-i\int_0^T H(t)dt}|\varphi(s(0))\rangle = \mathcal{U}_{0\to T}|\varphi(0)\rangle. \tag{3.21}$$

The adiabatic algorithm then states that if $|\varphi(0)\rangle = |\varphi_0(s=0)\rangle$ is the initial ground state and the energy gap $\Delta(s) = E_1(s) - E_0(s)$ between the ground state and first excited state of $H(s)$ never closes during the whole path, i.e. $\Delta = \min_{s\in[0,1]} \Delta(s) > 0$, then one has $|\varphi_0(s(T)=1)\rangle = |\psi_0\rangle$ in the limit $T \to \infty$, i.e. the desired ground state of the Hamiltonian of interest H_1.

If instead a finite time T is taken, some population may be excited from the ground state to excited states during the evolution if the process is too fast, loosing thus any

---

[21] Fock states are the natural available product states in the FermiQP platform, since they consist of atoms sitting one on each lattice site.

[22] Note that these could be improved to the best adiabatic preparation protocol by means of optimal control methods by providing the available control parameters and optimizing the resulting fidelity. We leave this out of the scope of the present thesis.

[23] For instance, a state that is easy to prepare in an experiment.

[24] Note that the adiabatic path will be specified by the form of the function $s : [0,T] \longrightarrow [0,1],\ t \mapsto s(t)$, which is only constrained to be monotone increasing from $s(0) = 0$ to $s(T) = 1$. We will make the (not necessarily optimal) linear choice $s(t) = t/T$.

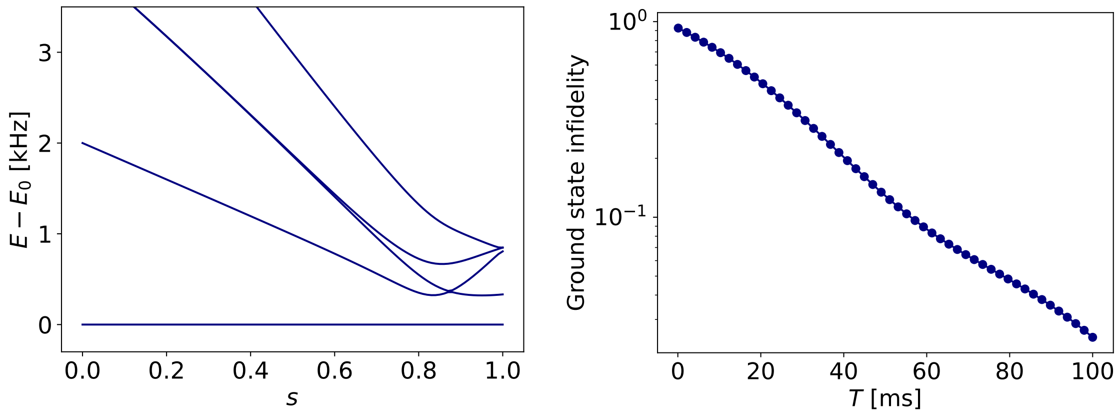

(a) Adiabatic spectrum (b) Simulation of adiabatic algorithm

Figure 3.10: Spectrum of the adiabatic path $H(s) = (1-s)[H_U + H_{\mu_{i\sigma}}] + sH_{\text{FH}}$ with finite gap $\Delta = 0.3211$ and (in)fidelity of the adiabatic algorithm preparing the ground state $|\psi_0\rangle$ of the Fermi-Hubbard model H_{FH} at $U/t = 8$ on a 2×2 lattice at half filling.

guarantee to obtain the ground state $|\psi_0\rangle$ as the final state. However, the adiabatic theorem states that if $T = \text{poly}(1/\Delta^3, 1/\epsilon)$ [92], one can obtain a state $|\varphi(s(T))\rangle$ that is at a distance $\| |\varphi(s(T))\rangle - |\psi_0\rangle \| < \epsilon$, i.e. a very good approximation provided $\epsilon > 0$ is small. Thus, given the presence of a persistent gap, the adiabatic evolution is able to provide the ground state of the target Hamiltonian with high fidelity if the evolution is carried out sufficiently slow, i.e. for large T.

In the FermiQP platform, the adiabatic evolution can readily be simulated analogically, avoiding Trotterization schemes used in digital quantum computers where it has to be discretized in steps with unitary gates. In what follows, two distinct adiabatic analog evolutions are presented for the ground state preparation of the Fermi-Hubbard model (3.1) defined only on decoupled 2×2 plaquettes, which is the product of plaquettes we are aiming as initial state for our algorithm.[25]

- **Introducing a chemical potential gradient $\mu_{i\sigma}$.** Here the starting Hamiltonian consists of an on-site interaction term and an additional site and spin dependent chemical potential term, while omitting any hopping between sites. The final Hamiltonian is the Fermi-Hubbard H_{FH} (3.1) at $U/t = 8$, with the path being

$$H(s) = (1-s)\left[U\sum_i n_{i\uparrow}n_{i\downarrow} + \sum_{i\sigma}\mu_{i\sigma}n_{i\sigma}\right] + sH_{\text{FH}} \tag{3.22}$$

$$= -\tilde{t}(s)\sum_{\langle i,j\rangle,\sigma}(c_{i\sigma}^\dagger c_{j\sigma} + \text{h.c.}) + U\sum_i n_{i\uparrow}n_{i\downarrow} + (1-s)\sum_{i\sigma}\mu_{i\sigma}n_{i\sigma} \tag{3.23}$$

---

[25] Note, however, that for the numerical simulation of the following adiabatic evolutions, a discretization with *piecewise* time evolutions has indeed been impemented.

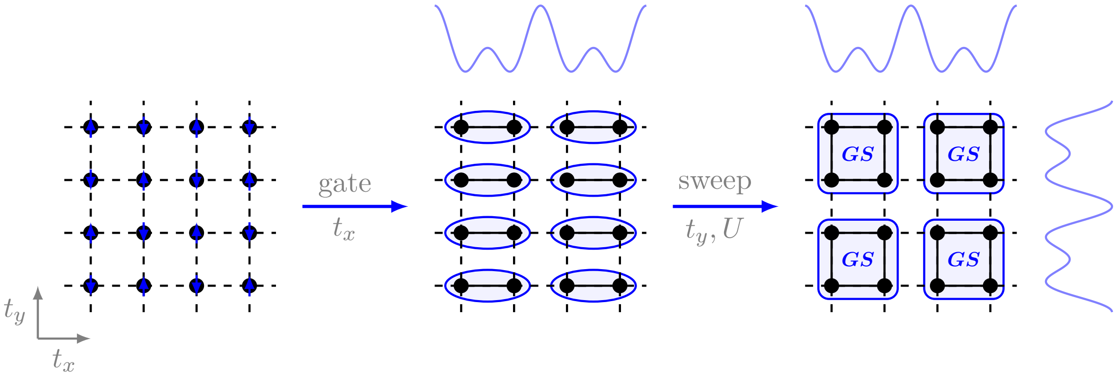

Figure 3.11: Initial state preparation starting from an AFM Fock state with alternated spins. A global gate delocalizes the state $|\uparrow, \downarrow\rangle$ within each consecutive double well, after which the adiabatic evolution is implemented by ramping up t_y and U leading to the ground state on each plaquette.

where $\mu_{i\sigma} = 2i\delta_{\sigma,\downarrow}$ and $\tilde{t}(s) = st$.[26] The initial and final ground states are the Fock state $|\uparrow, \uparrow, \downarrow, \downarrow\rangle$ and the superposition (3.16), respectively.[27]

Ramping up the tunneling parameter of the Fermi-Hubbard model alone is not enough to open the gap in the adiabatic path; hence the reason for introducing a gradient in the chemical potential breaking the symmetry between sites and spins.

Observe that this adiabatic evolution can be carried out on a analog quantum simulator by ramping up the tunneling parameter $\tilde{t}(s) = st$ from 0 to t *while simultaneously* ramping down the chemical potential gradient. The resulting spectrum is shown in Fig. 3.10a with a finite gap $\Delta = 0.3211$ that allows the adiabatic evolution to reach the ground state of the Fermi-Hubbard model within each 2×2 plaquette with fidelities of 99.9% for evolution times $T \simeq 50$ms (see Fig. 3.10b).

The drawback of this proposal from the practical point of view is that experimentally inducing a spin-dependent chemical potential can be challenging.

- **Tuning the on-site interaction U and tunneling t_y.** This second proposal avoids the introduction of chemical potential gradients by instead making use of a simple gate sequence preceding the actual adiabatic evolution. The procedure is the following (see Fig. 3.11):
  1. Start with on-site interaction and tunneling parameters in both directions switched off, i.e. $U = t_x = t_y = 0$.
  2. Prepare the Fock state given by an antiferromagnet (AFM), i.e. with alternated spins for consecutive sites: ↑↓↑↓ ...
  3. Apply then a global pulse consisting of one gate per each pair of horizontally consecutive sites that brings the state $|\uparrow, \downarrow\rangle$ within every double well into its

---

[26] The numbering i of the sites goes from bottom to top and from left to right on the 2×2 lattice.

[27] Following QuSpin's ordering convention (3.17).

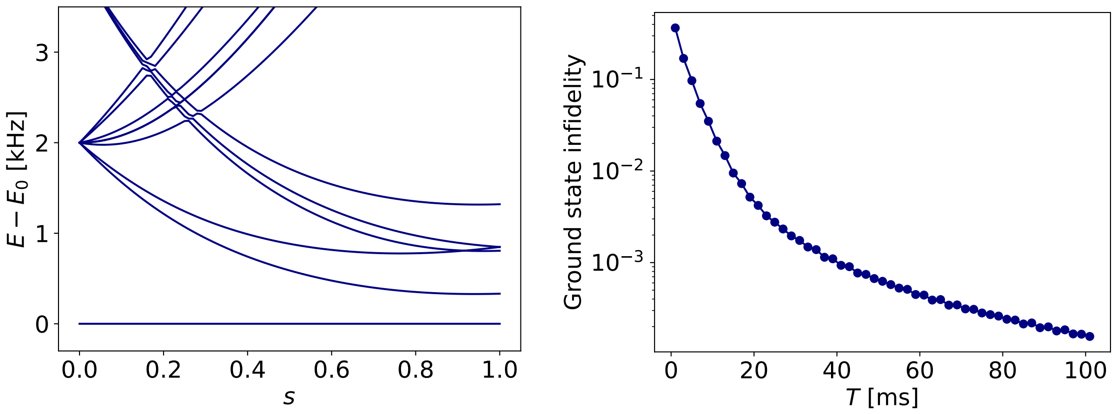

(a) Adiabatic spectrum (b) Simulation of adiabatic algorithm

Figure 3.12: Spectrum of the adiabatic path $H(s) = (1-s)H_{\mathrm{FH}}(1,0,0) + sH_{\mathrm{FH}}(1,1,8)$ with finite gap $\Delta = 0.3287$ and (in)fidelity of the adiabatic algorithm preparing the ground state $|\psi_0\rangle$ of the Fermi-Hubbard model $H_{\mathrm{FH}}(t_x, t_y, U)$ on a 2×2 lattice at half filling.

delocalized configuration $\frac{1}{2}(|\uparrow,\downarrow\rangle + |\downarrow,\uparrow\rangle + |\uparrow\downarrow,0\rangle + |0,\uparrow\downarrow\rangle)$. The product of two copies of this state forming a 2×2 plaquette constitutes the ground state $|\varphi_0(s=0)\rangle$ of the Fermi-Hubbard Hamiltonian $H_{\mathrm{FH}}(t_x, t_y, U)$ on that plaquette with $t_x = 1$ and $t_y = U = 0$, which is considered as initial Hamiltonian H_0 for the adiabatic path.

4. Now adiabatically evolve from H_0 to the complete Fermi-Hubbard Hamiltonian $H_1 \equiv H_{\mathrm{FH}}(t_x = 1, t_y = 1, U = 8)$ within each plaquette:

$$H(s) = -t_x \sum_{\langle i,j\rangle_x,\sigma} (c^\dagger_{i\sigma}c_{j\sigma} + \text{h.c.}) - st_y \sum_{\langle i,j\rangle_y,\sigma} (c^\dagger_{i\sigma}c_{j\sigma} + \text{h.c.}) + sU\sum_i n_{i\uparrow}n_{i\downarrow}. \tag{3.24}$$

The resulting adiabatic spectrum is shown in Fig. 3.12a with a gap $\Delta = 0.3287$ that allows the adiabatic evolution to reach the half-filled ground state of the Fermi-Hubbard model within each 2×2 plaquette with fidelities of 99.999% for evolution times $T \simeq 40$ms (Fig. 3.12b). This constitutes an improvement both in fidelity and speed of the adiabatic preparation in comparison to the first proposal.

The drawback in this case is that one has to ramp up the on-site interaction U, which can be experimentally challenging for fast evolutions. One can do it by either tuning the magnetic field (Feshbach resonance), which is a rather slow process, or by tuning the width of the wells in the optical lattice, which is plausible. All in all, it seems to be the more promising proposal among the two presented ones.

To sum up, we select the initial state for the algorithm as the product of 2×2 plaquette half-filled ground states, lying at $e/t \simeq -0.33$ in energy density, and also have a well-defined way of efficiently preparing it from the AFM Fock state via adiabatic evolution.

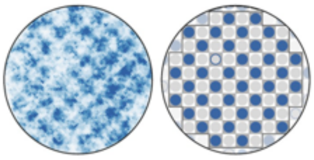

Figure 3.13: Snapshot of a many-body state on an optical lattice taken by means of a quantum gas microscope, which allows single site and spin resolved imaging of fermions. This enables the direct observation of e.g. magnetic order, spread of particle correlations and detection of many-fermion entanglement. Reproduced from Mazurenko et al. [60].

3.4 Loschmidt echo resolution via Imaginary Time Evolution

We are now left with the question on how to efficiently determine the Loschmidt echos (3.4, 3.5, 3.6) with the FermiQP quantum simulator. Note first that these three distinct quantities can be summarised as $\langle\psi'|e^{-iHt}|\psi''\rangle$, with $|\psi'\rangle = A|\psi\rangle$ for (3.5) and $|\psi''\rangle = A|\psi\rangle$ for (3.6), while $|\psi'\rangle, |\psi''\rangle$ being $|\psi\rangle$ in any other case.[28] We will focus on the case $\langle\psi|e^{-iHt}|\psi\rangle$ for simplicity and comment on the slight modifications for the other cases in passing. Note that for each t, these will in general be complex numbers

$$\langle\psi|e^{-iHt}|\psi\rangle = r(t)e^{i\phi(t)} \in \mathbb{C} \tag{3.25}$$

having an amplitude $r(t)$ and a phase $\phi(t)$.

The former, $r(t) = |\langle\psi|e^{-iHt}|\psi\rangle|$, can be found by just preparing the state $|\psi\rangle$ and letting the system evolve under H in the analog mode, before measuring the resulting state in a basis containing $|\psi\rangle$. To be more precise, one would start with a definite Fock state on the optical lattice, e.g. an antiferromagnet (AFM) $\uparrow\downarrow\cdots\uparrow\downarrow$, and prepare the state $|\psi\rangle$ by applying a unitary V (be it a gate sequence or the adiabatic preparation), $|\psi\rangle = V|\text{AFM}\rangle$, followed by the Hamiltonian evolution e^{-iHt} before undoing the state preparation with $V^\dagger$ (or reversing the adiabatic evolution with $\mathcal{U}_{T\to 0}$).[29] At this stage one would apply a spin-resolved measurement such as in Fig. 3.13 to the resulting state $|\zeta\rangle = V^\dagger e^{-iHt}V|\text{AFM}\rangle$, which amounts to implementing a measurement in the Fock basis (the natural analogue of the computational basis for this platform). Each measurement will collapse the state $|\zeta\rangle$ to a different Fock state $|\sigma_1, \sigma_2, ...\rangle, \sigma_i \in \{0, \uparrow, \downarrow, \uparrow\!\downarrow\}$, with probability given by the modulus squared $|c_{\boldsymbol{\sigma}}|^2$ of its coefficients in the Fock basis, i.e. $|\zeta\rangle = \sum_{i=1}^{N}\sum_{\sigma_i} c_{\boldsymbol{\sigma}}|\sigma_1, \sigma_2, ...\rangle$. Thus, the initial (basis) state $|\text{AFM}\rangle$ will be measured with probability $|\langle\text{AFM}|\zeta\rangle|^2 = |\langle\text{AFM}|V^\dagger e^{-iHt}V|\text{AFM}\rangle|^2 = |\langle\psi|e^{-iHt}|\psi\rangle|^2 = r(t)^2$. Repeating the experiment enough times to decrease the variance of the distribution to the desired accuracy, one can estimate this number from the statistical observed probability

---

[28] Observables in quantum mechanics are hermitian operators, $A^\dagger = A$, so $|\psi'\rangle = A^\dagger|\psi\rangle = A|\psi\rangle$ in (3.5).

[29] For the Loschmidt echos (3.5, 3.6), the action of the observable A can be simply introduced as an intermediate gate before/after the time evolution provided it is unitary. If it is not, one can decompose any non-unitary operator into a linear combination of unitaries (LCU) and implement each of them at the expense of needing more measurements [93, 94].

of obtaining that outcome. Taking the square root of that number leaves us with the desired amplitude $r(t)$.

A comment is in order regarding reversing the adiabatic evolution. We consider the case where the state $|\psi\rangle = V|\mathrm{AFM}\rangle$ — e.g. the plaquette ground state $|\psi\rangle = |\mathrm{pGS}\rangle$ considered in previous sections — is prepared from the Fock state $|\mathrm{AFM}\rangle$ through V, the adiabatic evolution

$$\mathcal{U}_{0\to T} := \mathcal{T} e^{-i\int_0^T \widetilde{H}(t)dt}, \tag{3.26}$$

where the time ordering of the exponential has been made explicit. After a given time evolution e^{-iHt}, one is interested in reversing V to measure in the Fock basis, as explained earlier. Although the operation $V^\dagger$ given by

$$\mathcal{U}^\dagger_{0\to T} = \mathcal{T} e^{+i\int_0^T \widetilde{H}(t)dt} \tag{3.27}$$

is in this case unavailable in that it involves a backwards-in-time evolution, the effect of the time reversal can fortunately be implemented (up to a phase) by applying the adiabatic evolution with the reversed path[30]

$$\mathcal{U}_{T\to 0} := \mathcal{T} e^{-i\int_T^0 \widetilde{H}(t)dt}. \tag{3.28}$$

The latter differs from $\mathcal{U}^\dagger_{0\to T}$ due to the time ordering present, but indeed maps $|\mathrm{pGS}\rangle$ back to $|\mathrm{AFM}\rangle$ possibly up to a phase factor, i.e. $\mathcal{U}_{T\to 0}|\mathrm{pGS}\rangle = e^{i\phi}|\mathrm{AFM}\rangle$, leading to

$$|\langle \mathrm{AFM}|\mathcal{U}_{T\to 0} e^{-iHt}\mathcal{U}_{0\to T}|\mathrm{AFM}\rangle| = |e^{+i\phi}\langle \mathrm{pGS}|e^{-iHt}|\mathrm{pGS}\rangle| = |\langle \mathrm{pGS}|e^{-iHt}|\mathrm{pGS}\rangle|, \tag{3.29}$$

as desired. In case any gate sequence is applied before the adiabatic evolution, this can in turn be simply undone in the reversed process by applying the daggered gate sequence after reversing the adiabatic evolution. This makes clear how to reverse the adiabatic evolution process to measure in the Fock basis, allowing the measurement of amplitudes $r(t) = |\langle\psi|e^{-iHt}|\psi\rangle|$ in (3.25).

Resolving the phase in (3.25) with the quantum simulator, however, is a more challenging task. We will consider next two different approaches to determine such variable, before ending with the third proposal to overcome this affair.

3.4.1 Hadamard test

The first option to resolve the phase of a Loschmidt echo is to consider the well-known Hadamard test (see Fig. 3.14). This is an interferometric method to extract the real and imaginary part of the expectation value $\langle\psi|U|\psi\rangle$ for a given unitary U, thus in particular allowing to discern its phase. In the special case $U = e^{-iHt}$, the Loschmidt echo (3.4) is recovered.

The test works as follows. One starts with a state $|\psi\rangle$ and an auxiliary qubit $|0\rangle$. Applying the Hadamard gate yields $H|0\rangle|\psi\rangle = |+\rangle|\psi\rangle$.[31] The unitary U on the second

---

[30] Note that the presence of the gap is only dependent on the path $\widetilde{H}(s)$, but not the evolution's time direction, meaning the mapping of ground states between endpoints is guaranteed in both directions.

[31] Recall that $|\pm\rangle = (|0\rangle \pm |1\rangle)/\sqrt{2}$.

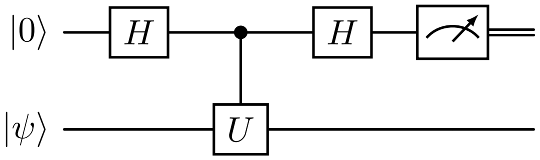

Figure 3.14: Circuit for the Hadamard test, which allows to retrieve the real part of the expectation value $\langle\psi|U|\psi\rangle$ for a given unitary U. Starting instead with $S|\psi\rangle$ gives the imaginary part.

register controlled to the auxiliary qubit acts then as[32] $|0\rangle|\psi\rangle + |1\rangle(U|\psi\rangle)$. Applying the second Hadamard gate leaves $|+\rangle|\psi\rangle + |-\rangle(U|\psi\rangle) = |0\rangle(\mathbb{1}+U)|\psi\rangle + |1\rangle(\mathbb{1}-U)|\psi\rangle$, with normalization factor $1/2$. Measuring then the first (auxiliary) qubit in the computational basis, the result will be $|0\rangle$ with probability $\frac{1}{4}\langle\psi|(\mathbb{1}+U^\dagger)(\mathbb{1}+U)|\psi\rangle = \frac{1}{2}(1+\mathrm{Re}\langle\psi|U|\psi\rangle)$ for output 1, and $|1\rangle$ with probability $\frac{1}{4}\langle\psi|(\mathbb{1}-U^\dagger)(\mathbb{1}-U)|\psi\rangle = \frac{1}{2}(1-\mathrm{Re}\langle\psi|U|\psi\rangle)$ for output -1. Repeating the test many times and obtaining the statistical probability of obtaining each outcome, one can estimate $\mathrm{Re}\langle\psi|U|\psi\rangle$. Repeating the same procedure by applying first an S gate to $|\psi\rangle$ at the very beginning (i.e. starting with the state $\frac{1}{\sqrt{2}}(|0\rangle + i|1\rangle)|\psi\rangle$ instead), yields probabilities $\frac{1}{2}(1 \pm \mathrm{Im}\langle\psi|U|\psi\rangle)$, from which $\mathrm{Im}\langle\psi|U|\psi\rangle$ can be estimated. Thus, in particular, the phase of $\langle\psi|U|\psi\rangle$ can be learned with an accuracy determined by the number of measurements[33].

The issue in this approach is that it involves a global controlled operation, which is hard to implement. This demands for an alternative approach to resolve the phase of Loschmidt echos.

3.4.2 Symmetric Hamiltonians

A second possibility is presented in Appendix A.5 of [83], where a result avoiding the use of ancilla qubits, global controlled operations and catlike states is provided. However, it holds only for Hamiltonians H with certain symmetries. Fortunately, these are satisfied by the 2D Fermi-Hubbard model (3.1).

The assumption is that there exist a unitary operator R and a Hermitian operator T such that

$$R^\dagger H R = -H + T \tag{3.30}$$

with $[T, H] = 0$ and for which $|\psi\rangle$ is an eigenstate, i.e.

$$R|\psi\rangle = \lambda|\psi\rangle, \quad T|\psi\rangle = \mu|\psi\rangle. \tag{3.31}$$

Being R unitary, necessarily $|\lambda| = 1$. Then, given such R, T and $|\psi\rangle$, it holds

$$a_\psi(t) \equiv \langle\psi|e^{-iHt}|\psi\rangle = \langle\psi|R^\dagger e^{-iHt}R|\psi\rangle = \langle\psi|e^{i(H-T)t}|\psi\rangle = \overline{a_\psi(t)}e^{-i\mu t}. \tag{3.32}$$

---

[32] We omit global factors for the computation, deferring the normalization till the end before measuring.

[33] Assuming noiseless gates.

As a consequence, $a_\psi(t)e^{i\mu t/2} \in \mathbb{R}$ is real.[34] Thus, the phase of the Loschmidt echo $a_\psi(t)$ is simply given by minus the phase of $e^{i\mu t/2}$.[35]

In the concrete case of the two-dimensional Fermi-Hubbard model in a bipartite lattice

$$H = \sum_{k\in A, m\in B} \sum_\sigma J_{km\sigma}(c^\dagger_{k\sigma} c_{m\sigma} + \text{h.c.}) + \sum_k U n_{k\uparrow} n_{k\downarrow}, \tag{3.33}$$

condition (3.30) is fulfilled according to [83] with[36]

$$R = e^{i\pi \sum_{k\in A} n_{k\downarrow}} \prod_k (c_{k\uparrow} + c^\dagger_{k\uparrow}), \quad T = U\sum_k n_{k\downarrow}. \tag{3.34}$$

Expression (3.1) is recovered for $J_{km\sigma} = -t$ for all k, m, σ and with bipartition $A \cup B$ of the 2D lattice defined by dividing the sites into even (A) and odd (B), i.e. whether site (i, j) has $i \oplus j \equiv 0$ (even) or 1 (odd) mod 2.

One still needs to consider states $|\psi\rangle$ satisfying (3.31) and lying at the desired energy regime of interest to apply the algorithm on. Lu et al. [83] provide a hole orthogonal basis of common eigenstates of R and T with simple structure for a lattice with an even number of sites N in the following way. They divide the lattice in $N/2$ disjoint pairs of sites $S_j = (n_j, m_j)$, $j = 1, \dots, N/2$ — e.g. snake-like ordering double wells as $S_j := (2j-1, 2j)$ — and choose within each of them a state $|\phi_{0,j}\rangle$, which is the vacuum of spin up and an arbitrary Fock state of spin down modes, to then define

$$|\varphi_j^\pm\rangle = \frac{1}{\sqrt{2}}(a^\dagger_{n_j,\uparrow} \pm i a^\dagger_{m_j,\uparrow})|\phi_{0,j}\rangle, \tag{3.35}$$

$$|\phi_j^\pm\rangle = \frac{1}{\sqrt{2}}(1 \pm i a^\dagger_{n_j,\uparrow} a^\dagger_{m_j,\uparrow})|\phi_{0,j}\rangle. \tag{3.36}$$

Then, an orthogonal basis of common eigenvectors $|\psi\rangle$ can be formed as all possible products of one of these 2 × 1 "plaquette" states.

However, the energy range these states cover has to be analyzed yet. For this purpose, we proceed at this point with some simulations on a 3 × 2 lattice[37] on python's `QuSpin` package [89]. The Hamiltonian (3.1) is implemented and the energy density of its eigenstates is checked to follow a Gaussian-like distribution, as expected from the Law of Large Numbers. Then, we compute as a function of U/t the energies of the

---

[34] Since we have seen that it is equal to its complex conjugate.

[35] Moreover, if $R^\dagger A R = \pm A$, and additionally either $|\psi\rangle$ is an eigenstate of A (with eigenvalue 1 for simplicity), or $[A, H] = 0$, then $a_{A,\psi}(t)e^{i\mu t/2}$ is also real or purely imaginary, depending on the sign ±. To determine $a_{A,\psi}(t)$, then, one only needs the absolute value $|a_{A,\psi}(t)|$ and a sign.

[36] The intuition behind this is as follows: T counts — times a U factor — the number of spin-down modes, while R has two terms: one that flips the occupation number of spin-up modes at each site ($0 \longleftrightarrow \uparrow$) and then a prefactor that reminds of a Jordan-Wigner string, though here only applied to the A sublattice (hence the reason why this term does not commute with the Hamiltonian H, which swaps particles between both sublattices $A \leftrightarrow B$).

[37] The Hilbert space dimension $2^{2\cdot 8}$ for a 4 × 2 lattice becomes already too large for numerical studies within a reasonable amount of time.

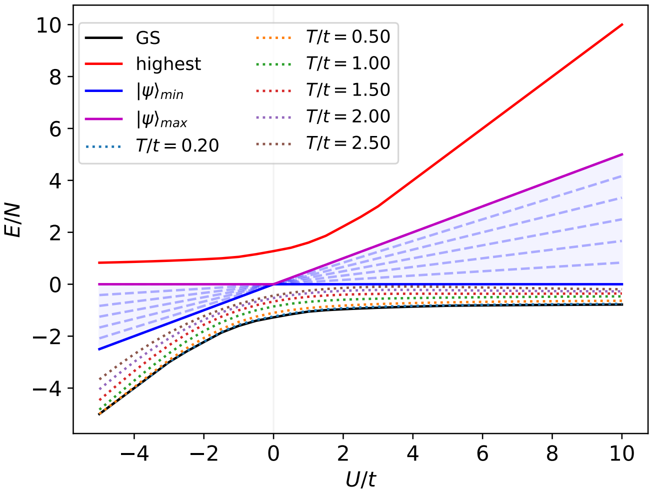

Figure 3.15: Energy range (blue colored) for states given by any product of (3.35, 3.36) in the 2D Fermi-Hubbard model on a 3×2 lattice as a function of U/t, together with the lowest (black) and highest (red) eigenenergies enclosing the spectrum of the model. Blue dashed lines show the precise discrete energies these states can reach. Energy curves for different thermal states at $T/t \in \{0.2, 0.5, 1, 1.5, 2, 2.5\}$ are added, showing that those temperatures correspond to low energies not covered by the considered family of states.

proposed states $|\psi\rangle$ given by all possible products of (3.35, 3.36) for each pair of sites S_j. The result is shown in Fig. 3.15, where the energy range for these states is delimited by the bright-blue and purple lines, while sitting within the spectrum of the 3×2 Fermi-Hubbard model delimited by the ground state energy (black) and maximal eigenenergy (red). This family of states does actually not cover the whole energy range (depicted in blue), but just a discrete set of values (dashed blue lines) linear in U. This behavior is reminiscent of the symmetry constrains (3.30, 3.31) imposed on the Hamiltonian.

Indeed, one can explicitly show this from relations (3.30, 3.31) with $|\lambda| = 1$ and realizing that (3.34) simply counts the number $N_\downarrow$ of spin-down modes of the state:

$$E(\psi) = \langle\psi|H|\psi\rangle = \langle\psi|R^\dagger H R|\psi\rangle = -\langle\psi|H|\psi\rangle + \langle\psi|T|\psi\rangle = -E(\psi) + UN_\downarrow, \qquad (3.37)$$

recovering the linear scaling $E(\psi) = \frac{1}{2}UN_\downarrow \propto U$. Furthermore, $N_\downarrow$ might be any natural number between 0 and N depending on the choice of $|\phi_{0,j}\rangle \in \{|0,0\rangle, |0,\downarrow\rangle, |\downarrow,0\rangle, |\downarrow,\downarrow\rangle\}$ for each of the $N/2$ pairs of sites S_j, where the information on the number of spin-down modes of the state lies. In particular, the bright-blue line in Fig. 3.15 corresponds to the case where all $|\phi_{0,j}\rangle$ are $|0,0\rangle$ thus giving zero energy, while the purple line relates to the one where they are all $|\downarrow,\downarrow\rangle$ yielding indeed energy $U \times N/2$. Therefore, the different energies covered by these states corresponds to the choice of each $|\phi_{0,j}\rangle$, determining the number $N_\downarrow \in \{0, 1, ..., N\}$ of spin-down modes in $|\psi\rangle$. For each of these $N+1$ possibilities, $E(\psi)$ scales with U with slope $N_\downarrow/2$, yielding the dashed blue lines in Fig. 3.15.

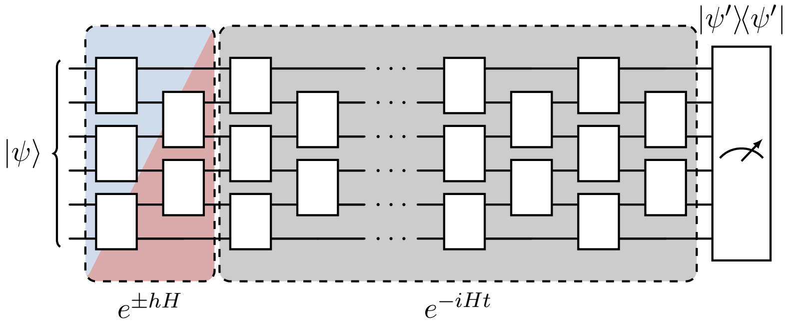

Figure 3.16: Circuit to measure $r(t \pm ih) = |\langle\psi'|e^{-iHt}e^{\pm hH}|\psi\rangle|$, where $e^{\pm hH}$ implements an imaginary time evolution onto $|\psi\rangle$, followed by a digital or analog real time evolution e^{-iHt} before applying a projective measurement onto the state $|\psi'\rangle$. The phase $\phi(t)$ of a Loschmidt amplitude $\mathcal{G}(t)$ can then be estimated from $r(t \pm ih)$. Reprinted from Yang et al. [84].

All in all, we notice that in the repulsive case $U > 0$ those states are not enough to cover the more interesting energy regime below zero, corresponding to low temperature thermal states $\rho_{\text{th}} = e^{-\beta H}/Z$, $Z = \text{Tr}[e^{-\beta H}]$. In Fig. 3.15 we show that energy curves $E = \text{Tr}[H\rho_{\text{th}}]$ for thermal states at temperatures ranging from $T/t = 2.5$ to $T/t = 0.2$ all lie within the negative energy regime beyond the blue shaded region, hinting at the fact that states (3.35, 3.36) are insufficient for the study of low-temperature physics.

To sum up, even though this proposal in [83] avoids the implementation of a controlled Hamiltonian evolution as instead required in the Hadamard test, the symmetries imposed in the argument unfortunately restrict the energy range covered by the initial states, preventing the algorithm from exploring lower energies of interest. Therefore, a different approach for the phase resolution is needed, which we provide next.

3.4.3 Imaginary Time Evolution

A great alternative circumventing these inconveniences in the Hadamard test and in the previous approach is presented by Yang et al. [84]. As will be shown, the proposal no longer involves global controlled operations, but this comes at the price of needing a short imaginary time evolution to be implemented (see Fig. 3.16).

The argument starts by considering an analytical continuation of the Loschmidt echo $\mathcal{G}(t) = \langle\psi'|e^{-iHt}|\psi\rangle$ extending time $t \in \mathbb{R}$ to the whole complex plane $z = t - i\beta \in \mathbb{C}$, with β being the imaginary time or inverse temperature.[38] The resulting complex function

$$\mathcal{G}(z) = \langle\psi'|e^{-iHz}|\psi\rangle = r(z)e^{i\phi(z)} \tag{3.38}$$

can be seen to be holomorphic by expanding the states $|\psi\rangle, |\psi'\rangle$ in the energy eigenbasis of H, leading to a linear combination of exponentials, which are known to be holomorphic.

---

[38] Recall that one may think of the Boltzmann factor $e^{-\beta H}$ for thermal states, with inverse temperature $\beta = 1/T \in \mathbb{R}$, as a Hamiltonian evolution $e^{-iH\tau}$ over a (pure) *imaginary* time $\tau = -i\beta \in \mathbb{C}$.

Then, the logarithm $\ln \mathcal{G}(z)$ will also be holomorphic everywhere except at those points where possibly $\mathcal{G}(z) = 0$. This means that for a choice of analytic branch for $\phi(z)$, one can apply Cauchy-Riemann equations to $\ln \mathcal{G}(z) = \ln r(z) + i\phi(z)$ and obtain

$$\frac{\partial}{\partial t}\phi(z) = \frac{\partial}{\partial \beta}[\ln r(z)], \tag{3.39}$$

relating the real time derivative of the phase we are interested in, to the imaginary time derivative of the logarithm of the amplitude. Numerically approximating the derivative on the right hand side by the symmetric difference quotient[39]

$$\frac{\partial}{\partial \beta}[\ln r(z)]\bigg|_{\beta=0} \approx \frac{\ln r(t-ih) - \ln r(t+ih)}{2h} \tag{3.40}$$

for small $h \ll 1$, Eq. (3.39) shows that one can compute the desired phase $\phi(t)$ of a Loschmidt echo by (numerical) integration

$$\phi(t) = \phi(0) + \int_0^t \left[\frac{\partial}{\partial \beta}[\ln r(z)]\bigg|_{\beta=0} \right] dt \tag{3.41}$$

provided $\mathcal{G}(t) \neq 0$ in the interval $[0,t]$ and the initial phase $\phi(0)$ and the amplitudes $r(t \pm ih)$ can be determined.

The initial phase is trivial for the most simple case (3.4) where $|\psi'\rangle = |\psi\rangle$, since $\mathcal{G}(0) = \langle\psi|\psi\rangle = 1 = r(0)e^{i\phi(0)}$ means $\phi(0) = 0$. For the Loschmidt echos (3.5, 3.6), we have $\mathcal{G}(0) = \langle\psi|A|\psi\rangle = \langle A\rangle_\psi$ meaning that $\phi(0) = \arg\langle A\rangle_\psi \in \{0, \pi\}$, since observables in quantum mechanics are Hermitian and thus have real expectation values.

Thus, the problem of finding the phase $\phi(t)$ of a Loschmidt echo is reduced to measuring the amplitudes $r(t \pm ih) = |\langle\psi'|e^{-iHt}e^{\pm hH}|\psi\rangle|$, which is what the circuit in Fig. 3.16 describes: prepare first the state $|\psi\rangle$ and then apply an imaginary time evolution $e^{\pm hH}$ before the usual real time Hamiltonian evolution e^{-iHt}, to end with a measurement projecting onto $|\psi'\rangle\langle\psi'|$. It has already been discussed at the beginning of this section how similar amplitudes could be determined experimentally by implementing the Hamiltonian evolution e^{-iHt} in the analog mode and taking spin-resolved measurements (see Fig. 3.13). While here we have the extra term $e^{\pm hH}$, the recipe is clear as long as we are able to implement this very short ($h \ll 1$) imaginary time evolution.

Implementation of the imaginary time evolution

Even though the non-unitarity of the imaginary time evolution forbids its direct application as a gate that one could implement in a quantum computer, Motta et al. [95] show how it can be simulated by a unitary circuit for short times h if H is a local Hamiltonian and the spacial correlations of $|\psi\rangle$ decay exponentially, which is the case for the Fermi-Hubbard model and the considered decoupled plaquette states.

---

[39] This formula for numerical differentiation cancels first order errors leading to an error of $\mathcal{O}(h^2)$.

The argument is as follows. Applying the imaginary time evolution e^{-hH} onto the state $|\psi\rangle$ will shrink its components inhomogeneously.[40] The resulting state $e^{-hH}|\psi\rangle$ can then be normalized with $\mathcal{N} = \|e^{-hH}|\psi\rangle\|$ to yield a valid quantum state $|\xi\rangle := \frac{1}{\mathcal{N}} e^{-hH}|\psi\rangle$. Then, there must exist a unitary U mapping $|\psi\rangle \mapsto |\xi\rangle$, i.e.

$$\frac{1}{\mathcal{N}} e^{-hH}|\psi\rangle \overset{!}{=} U|\psi\rangle. \tag{3.42}$$

Note that the unitary U will depend on the given state $|\psi\rangle$ to which the imaginary time evolution is applied. This unitary, however, can be highly complex for a general quantum state.[41] Nevertheless, following Motta et al. [95], one can decompose beforehand $e^{-hH} \simeq \prod_m e^{-hH_m}$ by a first-order Trotterization[42] into factors involving each a local term H_m in the Hamiltonian. One could then recursively apply the same argument as in (3.42) to each of the factors e^{-hH_m} to recursively obtain local unitaries V_m,

$$\frac{1}{\mathcal{N}_m} e^{-hH_m}|\psi_m\rangle \overset{!}{=} V_m|\psi_m\rangle, \quad \mathcal{N}_m = \|e^{-hH_m}|\psi_m\rangle\|, \tag{3.43}$$

where $|\psi_m\rangle = V_{m-1}|\psi_{m-1}\rangle$, $m > 1$, starting with $|\psi_0\rangle = |\psi\rangle$, such that $U = \prod_m V_m$. Each unitary V_m will be local acting on a domain surrounding the sites involved in H_m, depending on the finite correlation length of the state $|\psi_m\rangle$.

In practice, the V_m will be approximated, with the error being of the same order as the one already being made in the Trotterization step anyways. Indeed, since $e^{-hH_m} = \mathbb{1} - hH_m + \mathcal{O}(h^2)$ and $\mathcal{N}_m^2 = \langle\psi_m|e^{-2H_m}|\psi_m\rangle = 1 - 2h\langle\psi_m|H_m|\psi_m\rangle + \mathcal{O}(h^2)$ such that $1/\mathcal{N}_m = 1 + \langle\psi_m|H_m|\psi_m\rangle + \mathcal{O}(h^2)$, one sees that (3.43) — reading from right to left — becomes $V_m|\psi_m\rangle = [\mathbb{1} + \langle\psi_m|H_m|\psi_m\rangle - hH_m + \mathcal{O}(h^2)]|\psi_m\rangle$. Thus, taking the approximated unitaries $\widetilde{V}_m$ gives a good approximation $U \simeq \prod_m \widetilde{V}_m$.

Further, for small h, it is enough to consider the V_m defined all for the state $|\psi\rangle$ only, avoiding the recursive chain of states $|\psi_m\rangle$. Thus, one only needs to obtain each from

$$\frac{1}{\mathcal{N}_m} e^{-hH_m}|\psi\rangle \overset{!}{=} V_m|\psi\rangle, \quad \mathcal{N}_m = \|e^{-hH_m}|\psi\rangle\|, \tag{3.44}$$

and the order of the V_m in $U \simeq \prod_m V_m$ can be arbitrary. This can be illustrated by considering the simple example where the Hamiltonian is a geometrically 2-local one that can be written as a sum of two non-commuting Hamiltonians H_A, H_B consisting each of commuting summands. Then the unitaries U_A, U_B defined for the same state $|\psi\rangle$ as

$$U_A|\psi\rangle = \frac{1}{\mathcal{N}_A} e^{-hH_A}|\psi\rangle = \frac{1}{N_A}[\mathbb{1} - hH_A + \mathcal{O}(h^2)]|\psi\rangle, \tag{3.45}$$

$$U_B|\psi\rangle = \frac{1}{\mathcal{N}_B} e^{-hH_B}|\psi\rangle = \frac{1}{N_B}[\mathbb{1} - hH_B + \mathcal{O}(h^2)]|\psi\rangle, \tag{3.46}$$

---

[40] We focus here on the negative case. For e^{+hH}, simply replace $h \mapsto -h$ in the following results.

[41] That it is hard to compute follows from the fact that $\lim_{h\to 0} \frac{(e^{-H})^h}{\mathcal{N}}|\psi\rangle = |\mathrm{GS}\rangle$, where only the lowest eigenvalue survived, and obtaining the ground state (GS) of a local Hamiltonian is known to be a QMA-hard problem [69]. Thus finding a U implementing $\frac{1}{\mathcal{N}} e^{-hH}|\psi\rangle$ must be hard as well.

[42] With error $\mathcal{O}(h^2)$, as discussed in (2.1).

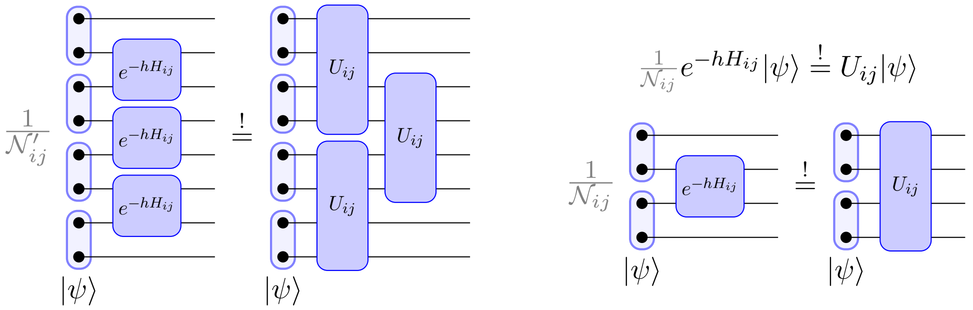

(a) ITE depth-two circuit.

(b) ITE building block.

Figure 3.17: Gate implementation of the imaginary time evolution (ITE) of the Hamiltonian given by the sum of hopping terms H_{ij} acting on decoupled pairs of sites. Its action on the state can be approximated up to normalization by a depth-two circuit (a) composed of building block unitaries U_{ij} acting each on four sites at most (b).

can be implemented by a shallow-depth quantum circuit depending on the correlation length of the state $|\psi\rangle$. The normalization factors are $1/\mathcal{N}_X = 1 + \langle\psi|H_X|\psi\rangle + \mathcal{O}(h^2)$, for $X \in \{A, B\}$, as similarly shown earlier. Then, $U_B U_A|\psi\rangle$ can be used to approximate $U|\psi\rangle$, since

$$\begin{aligned} U_B U_A|\psi\rangle &= \frac{1}{\mathcal{N}_A \mathcal{N}_B}[\mathbb{1} - hH_A - hH_B + \mathcal{O}(h^2)]|\psi\rangle \\ &= [\mathbb{1} + \langle\psi|H_A|\psi\rangle + \langle\psi|H_B|\psi\rangle - hH_A - hH_B + \mathcal{O}(h^2)]|\psi\rangle \end{aligned} \tag{3.47}$$

and on the other hand

$$U|\psi\rangle = \frac{1}{\mathcal{N}} e^{-hH}|\psi\rangle = [\mathbb{1} + \langle\psi|H|\psi\rangle - hH + \mathcal{O}(h^2)]|\psi\rangle, \tag{3.48}$$

so that the error is

$$\|(U - U_B U_A)|\psi\rangle\| = \mathcal{O}(h^2), \tag{3.49}$$

i.e. of the same order in h as the error of the Trotterization that we are making anyways. Note also that the alternative ordering $U_A U_B|\psi\rangle$ would give the same result as in (3.47) up to $\mathcal{O}(h^2)$.[43]

Focusing on the case of the 2D Fermi-Hubbard model (3.1), which is geometrically 2-local, Fig. 3.17b illustrates the idea for the imaginary time evolution of a single hopping term $H_{ij} = t\sum_\sigma(c^\dagger_{i\sigma}c_{j\sigma} + \text{h.c.})$ on a state $|\psi\rangle$ given by the product of disjoint pairs of entangled sites. The resulting unitary acts on at most the four sites involved in both entangled pairs. Fig. 3.17a illustrates the circuit of depth two that one would need in order to implement the imaginary time evolution of the full Hamiltonian term (the

---

[43] Note that this example can be straightforwardly extended to a larger number of such non-commuting Hamiltonians H_A, H_B, H_C..., as will be needed later for the Fermi-Hubbard model (five terms).

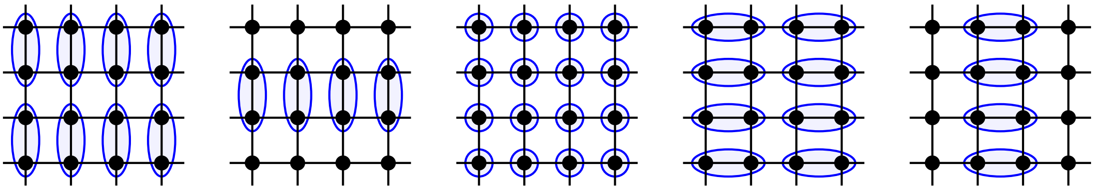

Figure 3.18: Illustration of the five non-commuting terms in the 2D Fermi-Hubbard Hamiltonian (H_x^e, H_x^o, H_U, H_y^e and H_y^o from left to right), each given by the sum of either disjoint hopping terms between neighboring sites (ellipses) or disjoint on-site interactions (circles).

analogue of H_A in the previous example) given by the sum of commuting hopping terms. In this case, the number of such non-commuting Hamiltonians H_X consisting each of commuting terms, would not be two but five (Fig. 3.18): one for the on-site interactions, $H_U = U\sum_i n_{i\uparrow}n_{i\downarrow}$, and two for the hoppings in both directions $\alpha \in \{x, y\}$, each acting on either even or odd pairs $p_\alpha \in \{e, o\}$, i.e. $H_\alpha^{p_\alpha} = t_\alpha \sum_{\langle i,j\rangle \in p_\alpha}(c_{i\uparrow}^\dagger c_{j\uparrow} + c_{i\downarrow}^\dagger c_{j\downarrow} + \text{h.c.})$.

Imaginary time evolution on the product of 2×2 plaquettes

Now, if we focus on the state $|\psi\rangle = |\text{pGS}\rangle$ given by the product of half-filled 2×2 plaquette ground states discussed earlier, we notice that the imaginary time evolution has to be implemented only for the hopping terms acting between decoupled plaquettes, and not for the terms acting within each plaquette (see Fig. 3.19a). The reason can be best explained by focusing on two plaquettes only (as in Fig. 3.19b). What we want to show is that, given the Hamiltonian $H = H_U + \sum_{\langle i,j\rangle} H_{ij}$ consisting of on-site interaction terms H_U plus hopping terms H_{ij} defined on two plaquettes $P \cup P'$, we only need to care about the terms H_{ij} *between* plaquettes, i.e. $i \in P, j \in P', P \cap P' = \emptyset$ (we denote these as $\langle i, j\rangle \in P \vee P'$). Indeed, this is the case because of the fact that we are applying the imaginary time evolution e^{-hH} to the state $|\text{pGS}\rangle$, which by definition is an eigenstate of the Hamiltonian on decoupled plaquettes $H_d \equiv H_U + \sum_{X\in\{P,P'\}}\sum_{\langle i,j\rangle\in X} H_{ij}$. As a result, a first order Trotterization will yield

$$e^{-hH}|\text{pGS}\rangle = e^{-hH_\vee}e^{-hH_d}|\text{pGS}\rangle \ + \ \mathcal{O}(h^2) = e^{-h\lambda_0}e^{-hH_\vee}|\text{pGS}\rangle \ + \ \mathcal{O}(h^2), \tag{3.50}$$

where $H_\vee \equiv \sum_{\langle i,j\rangle \in P\vee P'} H_{ij}$ and λ_0 is the eigenvalue of $H_d|\text{pGS}\rangle = \lambda_0|\text{pGS}\rangle$. Thus, up to a global phase $e^{-h\lambda_0}$ of the resulting state[44] and the Trotter error, the imaginary time evolution under H amounts to implementing it just for $H_\vee$ consisting of the Hamiltonian terms H_{ij} *between* plaquettes only.

Then, each of the corresponding gates U_{ij} implementing the effect of the imaginary time evolution between two 2×2 plaquettes (and thus in principle acting on the eight sites) could be decomposed into the native set of gates that can be implemented by the

---

[44] Remember we then normalize the resulting state $e^{-hH}|\psi\rangle$, so global factors disappear.

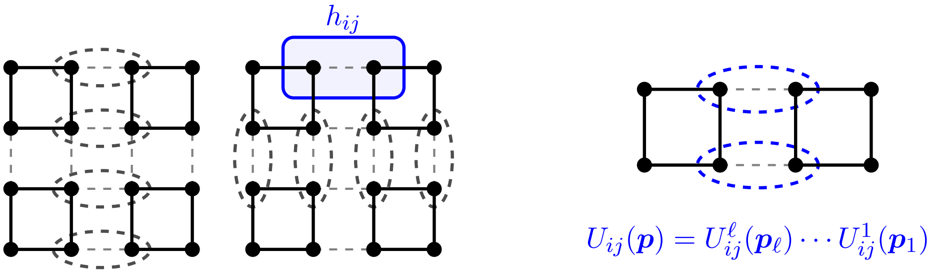

(a) ITE between plaquettes only. (b) Variational ansatz on building block.

Figure 3.19: The imaginary time evolution (ITE) of the Fermi-Hubbard model acting on the product of 2×2 plaquette ground states, has to be implemented for the hopping terms *between* the decoupled plaquettes only (a). The corresponding gates for the building block (b) could be obtained from the native gate set by means of a variational circuit ansatz optimized over parameters.

FermiQP quantum simulator. The approach would be to consider a variational circuit[45] ansatz $U_{ij}(\mathbf{p}) = U^{\ell}_{ij}(\mathbf{p}_\ell) \cdots U^{1}_{ij}(\mathbf{p}_1)$ with native gates U^{k}_{ij}, $k = 1, ..., \ell$, and optimize over the parameters[46] $\mathbf{p} = (\mathbf{p}_1, \dots, \mathbf{p}_\ell)$ by maximizing the cost function

$$\max_{\mathbf{p}} |\langle \mathrm{pGS}| U^{\dagger}_{ij}(\mathbf{p}) \frac{1}{\mathcal{N}} e^{-hH_{ij}} |\mathrm{pGS}\rangle|^2, \tag{3.51}$$

consisting in the fidelity of obtaining the same state by applying onto $|\mathrm{pGS}\rangle$ the imaginary time evolution than by applying the unitary $U_{ij}(\mathbf{p})$. Once the gate sequence for U_{ij} is obtained, by symmetry it can be used for all other terms between plaquettes.

Such task can be assessed with quantum optimal control techniques relying on gradient-based optimization methods such as the Gradient Ascent Pulse Engineering (GRAPE), which was first introduced in the context of NMR spectroscopy [96]. There, the fidelity between a given state $|\varphi\rangle$ and a time evolved one $e^{-iHt}|\psi\rangle$ is maximized[47] by discretizing the evolution with a finite number of steps with fixed step size Δt and optimizing over parameters $\mathbf{p} = (\mathbf{p}_1, ..., \mathbf{p}_\ell)$, i.e.

$$\max_{\mathbf{p}} |\langle \varphi| e^{-iH(\mathbf{p}_\ell)\Delta t} \cdots e^{-iH(\mathbf{p}_1)\Delta t} |\psi\rangle|^2. \tag{3.52}$$

Indeed, we have employed this method to successfully solve our optimization problem (3.51), where $|\varphi\rangle$ corresponds to the imaginary time evolved state and the unitaries are the time evolution operators. Following the above-mentioned approach, we have employed python's optimization function `scipy.optimize.minimize` with the bound-constrained minimization method L-BFGS-B [97, 98] guaranteeing the hopping control parameters to remain positive, $t \geq 0$, during optimization. We have fixed the on-site

---

[45] One could instead search for an adiabatic evolution implementing the same effect as the gate acting on the state. Working with gates, however, gives us more insight for scaling to larger plaquette sizes.

[46] Parameters may be e.g. the tunneling strengths t_x, t_y, on-site interaction U and gate durations τ.

[47] In practice, what is actually optimized is the minimization of the infidelity.

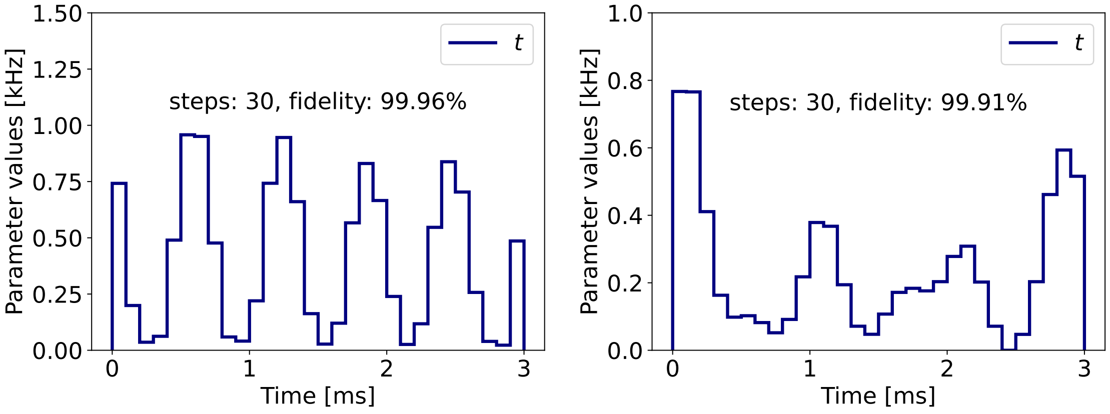

(a) Pulse sequence on a double well. (b) Pulse sequence on two 2×2 plaquettes.

Figure 3.20: Successful implementation of the imaginary time evolution ($h = 0.1$) under the Fermi-Hubbard Hamiltonian at $U/t = 8$ on a product of two (a) single sites and (b) 2×2 plaquettes through an optimal pulse sequence, with respective fidelities of 99.96% and 99.91% achieved within 3 ms. The pulse consists on a 30-step time evolution modulating the hopping strength t within the whole (a) double well or (b) 4×2 lattice, while keeping the global on-site interaction $U = 8$ activated.

interaction term to $U = 8$. It may be noted that there has been no need to include here spin-dependent tunneling to provide further computational resources, since both the initial state and the Hamiltonian involved in real and imaginary time evolutions are spin-symmetric[48], meaning that no preferred spin direction should be present in the optimal pulse sequence. We have indeed observed this numerically when optimizing over spin-dependent hopping strengths t_σ. We show in Fig. 3.20 the obtained pulse sequences for the implementation of the imaginary time evolution between both 1×1 “plaquettes” (single sites) and 2×2 plaquettes.[49] After a 3 ms sequence of 30 pulses, we already reach respective fidelities of 99.96% and 99.91%.

The discovery of this high-fidelity gate sequence for the implementation of the imaginary time evolution between two 2×2 plaquettes (Fig. 3.20b) constitutes one of our main achievements throughout this work. The four-layer application of simultaneous copies of this building block (Fig. 3.19b) pulse sequence between neighboring plaquettes as in Fig. 3.19a provides an implementation of the imaginary time evolution on the initial state given by the product of 2×2 plaquette half-filled ground states, enabling thus the experimental realization of the protocol on the FermiQP platform.

---

[48] Meaning that both spins play a symmetric role in the state and in the Hamiltonian as well.

[49] The pulse sequence on 1×1 “plaquettes” will be used later in Chapter 4.

Imaginary time evolution on a Fock state

For completeness, even though the obtained pulse sequences constitute already a great achievement and are experimentally more advantageous, an alternative approach for the implementation of imaginary time evolution would be to provide explicit gate decompositions at a theoretical level. We provide an example for the most simple case given by the product of 1 × 1 "plaquettes" (a product state), for which explicit[50] gate decompositions can be found for arbitrary unitaries acting on double wells (two sites). Although we know these states will not have low enough energies as wished for the proposed algorithm, the example serves as a proof of principle for the whole protocol, perhaps allowing us to gain some insight into the imaginary time evolution on larger plaquettes. We show this for a concrete initial state given by the antiferromagnet Fock state $|\mathrm{AFM}\rangle$.

First note that the imaginary time evolution has to be now engineered between 1 × 1 "plaquettes", i.e. between all pairs of sites. This means that the building block unitary will be acting on two sites only. Within each double well, the initial state will be $|\uparrow,\downarrow\rangle$. Then, we need a gate sequence that maps this state to the imaginary time evolved one

$$e^{\pm hH_{ij}}|\uparrow,\downarrow\rangle \simeq (1\pm hH_{ij})|\uparrow,\downarrow\rangle = |\uparrow,\downarrow\rangle \mp ht(|D,0\rangle + |0,D\rangle) =: \mathcal{N}|\xi_\pm\rangle \tag{3.53}$$

with norm $\mathcal{N} = \sqrt{1+2(ht)^2}$, where the approximation is of order $\mathcal{O}(h^2)$ as in the Trotterization. No on-site contributions U from (3.1) appear due to the fact that no doublons $D = \uparrow\!\downarrow$ are present in the initial state. Since the Hamiltonian H is particle and spin number preserving and we start with the state $|\uparrow,\downarrow\rangle$, we only have to work within the subspace $\mathcal{B} = \{|\uparrow,\downarrow\rangle, |\downarrow,\uparrow\rangle, |D,0\rangle, |0,D\rangle\}$. Then, the building block unitary $U_\pm$ of size 4×4 mapping $|\uparrow,\downarrow\rangle \mapsto |\xi_\pm\rangle$ can be decomposed into a two-step sequence of rotation gates as follows:

1. Rotate first $|\psi\rangle = |\uparrow,\downarrow\rangle$ to

$$|\psi'\rangle = (|\uparrow,\downarrow\rangle - \gamma|D,0\rangle)\frac{1}{\sqrt{1+\gamma^2}}, \tag{3.54}$$

   transferring thus some population to the doublon sector.

2. Then rotate within the doublon sector, leading to

$$|\psi''\rangle = \left[|\uparrow,\downarrow\rangle - \frac{\gamma}{\sqrt{2}}(|D,0\rangle + |0,D\rangle)\right]\frac{1}{\sqrt{1+\gamma^2}}, \tag{3.55}$$

   which recovers (3.53) for $\gamma_\pm = \pm\sqrt{2}ht$.

To obtain the gates implementing these two rotations, recall first the general form for an arbitrary "single-qubit" rotation[51]

$$U(\theta,\varphi,\delta) = \begin{pmatrix} \cos\left(\frac{\theta}{2}\right)e^{-i\delta} & \sin\left(\frac{\theta}{2}\right)e^{-i\varphi} \\ -\sin\left(\frac{\theta}{2}\right)e^{i\varphi} & \cos\left(\frac{\theta}{2}\right)e^{i\delta} \end{pmatrix} \tag{3.56}$$

---

[50] Explicit will be the unitary sequence, but not the Hamiltonians inducing them through time evolution.

[51] Up to a global phase $e^{i\mu}$.

with parameters $\theta \in [0, \pi]$ and $\varphi, \delta \in [0, \pi]$. Then, the first rotation in the ordered basis $\mathcal{B}$ is given by

$$U_1(\gamma) = \begin{pmatrix} \frac{1}{\sqrt{1+\gamma^2}} & 0 & \frac{\gamma}{\sqrt{1+\gamma^2}} & 0 \\ 0 & 1 & 0 & 0 \\ -\frac{\gamma}{\sqrt{1+\gamma^2}} & 0 & \frac{1}{\sqrt{1+\gamma^2}} & 0 \\ 0 & 0 & 0 & 1 \end{pmatrix} \tag{3.57}$$

and zero elsewhere, which can be attained for $(\theta, \varphi, \delta) = (\arccos(1/\sqrt{1+\gamma^2}), 0, 0)$. The second rotation is simply given by

$$U_2 = \begin{pmatrix} 1 & 0 & 0 & 0 \\ 0 & 1 & 0 & 0 \\ 0 & 0 & \frac{1}{\sqrt{2}} & -\frac{1}{\sqrt{2}} \\ 0 & 0 & \frac{1}{\sqrt{2}} & \frac{1}{\sqrt{2}} \end{pmatrix} \tag{3.58}$$

and zero elsewhere, which can in turn be attained for $(\theta, \varphi, \delta) = (\pi/2, \pi, 0)$.

All in all, the unitary $U_\pm = U_2 \cdot U_1(\gamma_\pm)$ with $\gamma_\pm = \pm ht$ acting on $|\psi\rangle = |\uparrow, \downarrow\rangle$ implements the imaginary time evolution $|\uparrow, \downarrow\rangle \mapsto \frac{1}{\mathcal{N}_\pm} e^{\pm h H_{ij}} |\uparrow, \downarrow\rangle$ as $U_\pm |\uparrow, \downarrow\rangle$ up to an error of order $\mathcal{O}(h^2)$, as desired.

This unitary would have to be applied to all pairs of sites to implement the imaginary time evolution for the whole Hamiltonian H, which could be done with a depth-4 circuit — corresponding to the terms in Fig. 3.18 involving pairs of sites.

Nevertheless, as anticipated, the concrete way how the rotation gates (3.56) would be implemented in the FermiQP demonstrator, amounts to finding native Hamiltonians $H(\theta, \varphi, \delta)$ and the proper times τ for which (3.56) can be realized as an analog Hamiltonian time evolution — that is $U(\theta, \varphi, \delta) = e^{-iH(\theta,\varphi,\delta)\tau}$ —, or rather a sequence thereof.

Chapter 4

Numerical Benchmark on small-sized 2D lattice

Having introduced and discussed the main aspects of the algorithm in the previous chapter, we present now a toy model on a small lattice of 3×2 sites to summarize the procedure by stating clearly all the steps to be followed in the protocol. This will be accompanied by a numerical simulation that could serve as a benchmark.

Recall we aim to use the filtering algorithm [83] to study microcanonical properties of a state in a system governed by the repulsive two-dimensional Fermi-Hubbard Hamiltonian

$$H = -t \sum_{\langle i,j \rangle, \sigma} (c^{\dagger}_{i\sigma} c_{j\sigma} + \text{h.c.}) + U \sum_{i} n_{i\uparrow} n_{i\downarrow}, \quad U > 0, \tag{4.1}$$

by computing Loschmidt echos of a different, in turn efficiently preparable state having some overlap with the target state.

4.1 Selection of parameters, observable and initial state

First and foremost, there are some choices to be made. We decide on the following:

a) We focus on the $U/t = 8$ regime of the Fermi-Hubbard model on a 3×2 grid, which means $N = 6$.

b) Several target energies are considered, given by the 20 lowest eigenenergies E_k up to $E = 2.84 \cdot 10^{-14} \simeq 0$ and the parameter $\delta = 1$ specifies the energy window $[E_k - \delta, E_k + \delta]$ for the filter.

c) The parameter x is simply chosen to be 1 — thus defining the cutoff $R = xN/\delta = 6$ in the Fourier transform for the filtering operator.

d) The antiferromagnetic Fock state $|\psi\rangle = |\uparrow, \downarrow, \uparrow, \downarrow, \uparrow, \downarrow\rangle \equiv |\text{AFM}\rangle$ is chosen as initial state (1×1 "plaquettes"), so in particular no preparation $|\psi\rangle = V|\text{AFM}\rangle$ is necessary ($V = \mathbb{1}$) further than obtaining $|\text{AFM}\rangle$. This state is efficiently preparable at FermiQP and lies at $E(\psi) = 0$. The overlap with each $|E_k\rangle$ will have to be checked. This state has no doping since it is at half filling. It specifies the particle number sector to be $S = (3\uparrow, 3\downarrow)$.

e) The observable A of interest — for which microcanonical expectation values are to be obtained — is chosen here to be simply the Hamiltonian energy H (4.1).

   Alternatively the local[1] longitudinal magnetization on the first site could be chosen:

$$A = n_{1\uparrow} - n_{1\downarrow}, \tag{4.2}$$

   with $\langle A\rangle_\psi \in [-1, 1]$ for any $|\psi\rangle$.

f) The small imaginary time parameter for the amplitudes $r(t \pm ih)$ involving imaginary time evolution is chosen to be $h = 0.1$.

g) The integration step for the phase resolution of Loschmidt echos — employing the data on $r(t \pm ih)$ — is taken to be $\Delta t = 0.1$.

Now the protocol can be summarized by following step by step the next sections.

4.2 Determination of Loschmidt echos

For each time $t_m = 2m/N$, with $m \in \{0, ..., R\}$, determine the Loschmidt echos

$$a_\psi(t_m) = \langle\psi|e^{-iHt_m}|\psi\rangle, \tag{4.3}$$
$$a_{A,\psi}(t_m) = \langle\psi|Ae^{-iHt_m}|\psi\rangle, \tag{4.4}$$
$$a_{\psi,A}(t_m) = \langle\psi|e^{-iHt_m}A|\psi\rangle, \tag{4.5}$$

by determining their amplitude $r(t_m)$ and phase $\phi(t_m)$.

4.2.1 Amplitude measurement of Loschmidt echos

For each given time t_m, to obtain the amplitude $r(t_m)$ for the Loschmidt echo (4.3), follow the next steps:

1. Prepare the initial state $|\psi\rangle = |\uparrow,\downarrow,\uparrow,\downarrow,\uparrow,\downarrow\rangle \equiv |\mathrm{AFM}\rangle$.
2. Let the system evolve under H (4.1) for a time t_m to reach the state $e^{-iHt_m}|\psi\rangle$.
3. Measure in the Fock basis by taking a site and spin resolved snapshot. Count $+1$ on the number of successes Σ if it coincides with the intial Fock state $|\mathrm{AFM}\rangle$.
4. Repeat (a-c) a large number of times, e.g. $L = 1000$.
5. Estimate the probability $r(t_m)^2 = |\langle\psi|e^{-iHt_m}|\psi\rangle|^2$ as Σ/L, from which the amplitude $r(t_m)$ can be obtained by taking the square root — this step is actually carried out in the classical post-processing part of the protocol.

---

[1] The global magnetization would always yield zero, since we are starting with a state at half filling and the Fermi-Hubbard Hamiltonian preserves the particle number of both spin up and down modes.

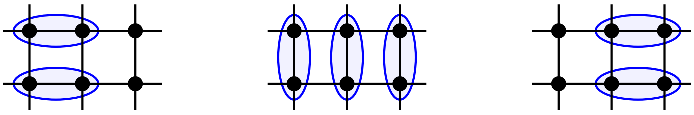

Figure 4.1: Illustration of the three non-commuting terms consisting of 2-site gates (blue) $U(h)$ on the 3×2 lattice, each composed of two rotation gates U_1, U_2, leading to a circuit of depth six.

For the Loschmidt echo (4.4), apply A between step 2 and step 3, and proceed the same way to obtain the amplitude $r(t_m) = |\langle\psi|Ae^{-iHt_m}|\psi\rangle|$.

For the Loschmidt echo (4.5), apply A between step 1 and step 2, and proceed the same way to obtain the amplitude $r(t_m) = |\langle\psi|e^{-iHt_m}A|\psi\rangle|$.

Note that for the special case where the operator A is diagonal in the Fock basis, there is no need to actually apply the operator before measuring. Instead, the value of the observable can be retrieved from the (collapsed) measured state. Thus, in the case of A being the local magnetization, the amplitudes $r(t_m)$ can be computed as $|\langle\psi|e^{-iHt}|\psi\rangle|$ times the number $|n_{1\uparrow} - n_{1\downarrow}|$ counted from the measured snapshot of the state.

4.2.2 Phase measurement of Loschmidt echos

For each given time t_m, to obtain the phase $\phi(t_m)$ for the Loschmidt echo (4.3), follow the next steps:

1. Prepare the initial state $|\psi\rangle = |\uparrow,\downarrow,\uparrow,\downarrow,\uparrow,\downarrow\rangle \equiv |\mathrm{AFM}\rangle$.

2. Apply the unitary $U(h)$ — optimal control pulse sequence (Fig. 3.20a and analogous for negative h) or rotation unitaries $U_2U_1(\gamma = ht)$ (3.57, 3.58) — onto $|\psi\rangle$ on pairs of neighboring sites by a 3-layer circuit (see Fig. 4.1), implementing the imaginary time evolution e^{-hH} under H (4.1), i.e.

$$\mathcal{U}(h)|\psi\rangle \equiv \left(\prod_{\langle i,j\rangle} U(h)\right)|\psi\rangle \overset{!}{=} \frac{1}{\mathcal{N}}e^{-hH}|\psi\rangle, \tag{4.6}$$

up to a normalization $\mathcal{N} = \mathcal{N}_{ij}^{|\langle i,j\rangle|}$, with $|\langle i,j\rangle| = (L_x-1)L_y + (L_y-1)L_x$ the number of hopping terms H_{ij} between 1×1 "plaquettes", for which the imaginary time evolved state (3.53) has norm $\mathcal{N}_{ij} = \sqrt{1+2(ht)^2}$.[2]

3. Discretize the interval $[0, t_m]$ into `isteps` $= \frac{t_m}{\Delta t} + 1$ slices $\{0, ..., \tilde{t}_{m_k}, ..., t_m\}$, with $k \in \{0, ..., \texttt{isteps} - 1\}$ and integration step Δt. For each $\tilde{t}_{m_k} := k\cdot\Delta t$:

   a) Let the system evolve analogically under H for a time $\tilde{t}_{m_k}$ to reach the state

$$|\varphi_h(\tilde{t}_{m_k})\rangle := e^{-iH\tilde{t}_{m_k}}\mathcal{U}(h)|\psi\rangle \tag{4.7}$$

---

[2] Note here that t is the tunneling parameter of the Fermi-Hubbard model, while t_m are times.

   b) Measure in the Fock basis by taking a spin resolved snapshot. Count +1 on the number of successes Σ if it coincides with the initial Fock state $|\mathrm{AFM}\rangle$.
   c) Repeat (1-3b) a large number of times, e.g. $L = 1000$.
   d) Estimate the probability $|\langle\psi|e^{-iH\tilde{t}_{m_k}}\mathcal{U}(h)|\psi\rangle|^2$ as Σ/L (later in the classical post-processing part).

4. Repeat the procedure (1-3) replacing $h \mapsto -h$ in the gates $U_1(\gamma)$ implementing e^{+hH}, to obtain the (estimated) probabilities $|\langle\psi|e^{-iH\tilde{t}_{m_k}}\mathcal{U}(-h)|\psi\rangle|^2$.

For the Loschmidt echo (4.4), apply A after step 3a leading to the state $A|\varphi_h(\tilde{t}_{m_k})\rangle$. Then proceed with (3b-4) to obtain the (estimated) probability $|\langle\psi|Ae^{-iH\tilde{t}_{m_k}}\mathcal{U}(h)|\psi\rangle|^2$.

For the Loschmidt echo (4.5), apply A after step 1 before implementing the imaginary time evolution, and then proceed with (2-4) to obtain the (estimated) probability $|\langle\psi|e^{-iH\tilde{t}_{m_k}}\mathcal{U}(h)A|\psi\rangle|^2$.

These probabilities will then be employed in the post-processing part of the protocol to classically compute the corresponding phase $\phi(t_m)$.

4.3 Classical Post-Processing

Once the required information on the Loschmidt echos is obtained from the quantum simulator, a classical post-processing task completes the computation of the generalized microcanonical expectation value of the observable of interest. The steps are as follows:

1. Estimate the amplitudes $r(t_m)$ as described in the previous section 4.2.1. by taking the square root of the estimated probabilities Σ/L. This holds for all three kinds of Loschmidt echos (4.3, 4.4, 4.5).

2. Estimate the phase $\phi(t_m)$ of each Loschmidt echos at time t_m as follows:
   a) Estimate the quantities $\nu_k^{\pm} := |\langle\psi|e^{-iH\tilde{t}_{m_k}}\mathcal{U}(\pm h)|\psi\rangle|$ for both $\pm h$ and each k by taking the square root of the corresponding estimated probabilities $\Sigma_k^{\pm}/L$, as described in section 3.2.2.
   b) Multiply each $\nu_k^{\pm}$ by the normalization factor $\mathcal{N}$ to properly implement the imaginary time evolution

$$\mathcal{N} \cdot \nu_k^{\pm} = |\langle\psi|e^{-iH\tilde{t}_{m_k}}\left(\mathcal{N} \cdot \mathcal{U}(\pm h)\right)|\psi\rangle| = |\langle\psi|e^{-iH\tilde{t}_{m_k}}e^{\pm hH}|\psi\rangle|^2, \qquad (4.8)$$

   and then take the square root to recover the amplitude $r(\tilde{t}_{m_k} \pm ih)$.
   c) Estimate then the derivatives

$$\gamma(\tilde{t}_{m_k}) := \frac{\partial}{\partial\beta}[\ln r(z)]\Big|_{t=\tilde{t}_{m_k},\beta=0} \approx \frac{\ln r(\tilde{t}_{m_k} - ih) - \ln r(\tilde{t}_{m_k} + ih)}{2h}, \qquad (4.9)$$

   where $z = t - i\beta$ has been used[3].

---

[3] Hence the reason why the minus term is placed before the plus one in the differentiation formula.

d) Resolve the phase by numerical integration

$$\phi(t_m) = \phi(0) + \int_0^{t_m} \left[\frac{\partial}{\partial\beta}[\ln r(z)]\Big|_{t=\tilde{t}_{m_k},\beta=0} \right] dt \approx \sum_k \gamma(\tilde{t}_{m_k})\Delta\tilde{t}, \tag{4.10}$$

with $\Delta\tilde{t} = \frac{t_m}{\texttt{isteps}-1}$, and where $\phi(0) = 0$ for Loschmidt echos (4.3) — since $r(0)e^{i\phi(0)} = \langle\psi\,|\,\psi\rangle = 1$ by normalization —, while for Loschmidt echos (4.4, 4.5) involving the observable A one has $r(0)e^{i\phi(0)} = \langle\psi|A|\psi\rangle \in \mathbb{R}$ so the initial phase is $\phi(0) = \arg\langle A\rangle_\psi \in \{0, \pi\}$.

3. Estimate each Loschmidt echo from its amplitude and phase as $r(t_m)e^{i\phi(t_m)}$ and call this number $a_\psi(t_m)$, $a_{A,\psi}(t_m)$ or $a_{\psi,A}(t_m)$ depending on the Loschmidt echo (4.3, 4.4, 4.5) that is being computed.

4. For negative times $t_m < 0$ within $m \in \{-R, ..., 0, ..., R\}$, retrieve the Loschmidt echos from the counterparts at positive times[4]

$$a_\psi(-|t_m|) = a^*_\psi(|t_m|), \tag{4.11}$$
$$a_{A,\psi}(-|t_m|) = a^*_{\psi,A}(|t_m|), \tag{4.12}$$
$$a_{\psi,A}(-|t_m|) = a^*_{A,\psi}(|t_m|). \tag{4.13}$$

5. Compute the numbers e^{iEt_m} and the coefficients

$$b_m = \frac{1}{2^M}\binom{M}{M/2 - m} \tag{4.14}$$

with $M = \lfloor N^2/\delta^2 \rfloor_2$.

6. Estimate the local density of states as the linear combination of Loschmidt echos

$$D_{\delta,\psi}(E) \equiv \langle\psi|P_\delta(E)|\psi\rangle \simeq \sum_{m=-R}^{R} b_m e^{iEt_m} a_\psi(t_m) \tag{4.15}$$

and call this number q.

7. Estimate the linear combination of Loschmidt echos involving A

$$\langle\psi|[AP_\delta(E) + P_\delta(E)A]|\psi\rangle \simeq \sum_{m=-R}^{R} b_m e^{iEt_m} a_{A,\psi}(t_m) + \sum_{m=-R}^{R} b_m e^{iEt_m} a_{\psi,A}(t_m) \tag{4.16}$$

and call it p.

8. Last, estimate the broadened microcanonical expectation value of observable A

$$A_{\delta,\psi}(E) = \frac{\langle\psi|[AP_\delta(E) + P_\delta(E)A]|\psi\rangle}{2\langle\psi|P_\delta(E)|\psi\rangle} \tag{4.17}$$

as the quotient $\frac{p}{2q}$.

---

[4] Note that $a_{\psi,A}(-t) = \langle\psi|e^{-iH(-t)}A|\psi\rangle = \langle\psi|A^\dagger e^{+iH(-t)}|\psi\rangle^* = \langle\psi|Ae^{-iHt}|\psi\rangle^* = a^*_{A,\psi}(t)$.

4.4 Numerical simulation

In this last section we present a few results obtained from the numerical implementation of the protocol. The fermionic quantum system is simulated via the `QuSpin` python package [89]. The codes are included in the Appendix. Two comments are in order:

Comment 1. Regarding the numerical simulation, amplitudes $r(t)$ and $r(t \pm ih)$ will not be estimated from repeated measurements as would be done in the quantum simulator. Instead, the measurement will be implemented numerically by directly computing the overlap of the time-evolved state with the initial state $|\psi\rangle$ — corresponding to applying a projector $|\psi\rangle\langle\psi|$.

Comment 2. Regarding the implementation of the imaginary time evolution, we briefly analyze the obtained fidelity when applying the multiple layers of pulse sequence corresponding to hopping terms between plaquettes. However, in subsequent parts of the protocol we instead implement the imaginary time evolution by matrix exponentiation to assess their errors independently.

4.4.1 ITE pulse sequence fidelity

First of all, we test the implementation of the imaginary time evolution (ITE), e^{-hH}, through the composition of 2-site unitaries as in Fig. 4.1 — each given by the pulse sequence from Fig. 3.20a — times the proper normalization factor, yielding an overall fidelity of 98% for $h = 0.1$. For the imaginary time evolution e^{+hH}, a corresponding optimized pulse sequence has been obtained with the same fidelity 99.96% as in Fig. 3.20a, which after the composition as in Fig. 4.1 together with the normalization factor yields an overall fidelity of 98.2%. These fidelities are still below 99.9% and give thus bad estimates on the phase, as has been observed numerically. For this reason, in the subsequent subsections we simulate the imaginary time evolution directly by matrix exponentiation.

4.4.2 Phase estimation

Here, the numerical result on the phase estimation method for the resolution of a Loschmidt echo is presented. This corresponds to steps 2c-2d in section 4.3. Fig. 4.2 shows the cumulative integration of the phase $\phi(t_m)$ for different times t_m and the corresponding error at each of them, where the integration step has been taken to be $\Delta t = 0.1$ ms.[5] In Fig. 4.2a we observe how the phase is precisely estimated for $h = 0.1$ up to times $t_m \simeq 15$ ms, when the errors start being significant. Fig. 4.2b shows that the oscillating instantaneous error is at least one order of magnitude smaller[6] than the computed phase up to $t_m \simeq 15$ ms, when the error indeed blows up for $h = 0.1$, in contrast to the smaller h. One can also observe that the phase estimation with $h = 0.01$ is as good as with $h = 0.001$, since both error curves overlap. The larger error for $h = 0.1$ hints at the fact that Δt should be smaller for larger h in order to keep the error small.

---

[5] We consider the tunneling strength $t = 1$ — different from time — to be in kHz.

[6] For $\Delta t = 0.01$ ms, the error $\Delta\phi$ is one order of magnitude further smaller than for $\Delta t = 0.1$ ms, but simulations take much longer times.

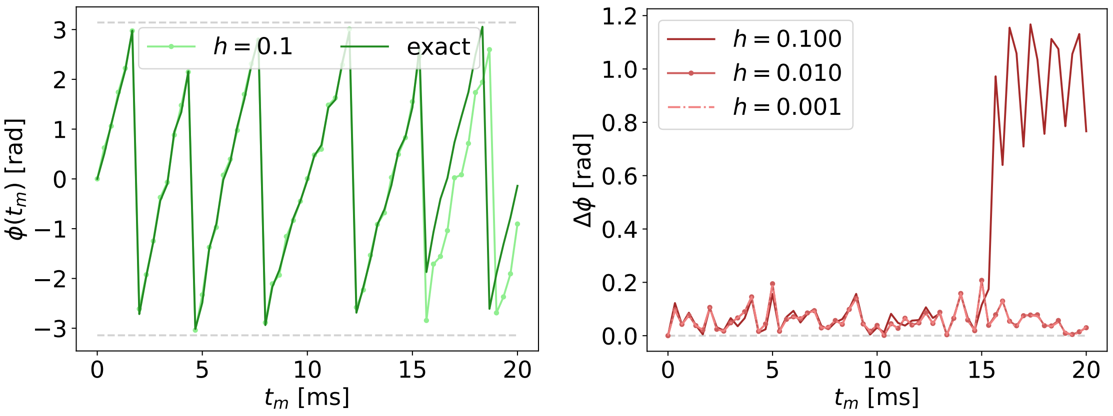

(a) Cumulative integrated phase mod 2π.

(b) Instantaneous integration error.

Figure 4.2: Phase of Loschmidt echos $\langle\psi|e^{-iHt}|\psi\rangle = r(t)e^{i\phi(t)}$ for different times t_m estimated through integration of the (approximated) imaginary time derivative of $\ln r(z)$ — with $h \in \{10^{-1}, 10^{-2}, 10^{-3}\}$ being the short imaginary time. The Hamiltonian H under consideration is the Fermi-Hubbard model at $U/t = 8$ on a 3×2 lattice and the state $|\psi\rangle$ is an antiferromagnetic Fock state. The integration step is $\Delta t = 0.1$.

All in all, these results show that the integration method for phase resolution works sufficiently well for already $h = 0.1$ up to times $t_m \simeq 15$ ms, and for $h = 0.01$ if longer times are needed.

4.4.3 Loschmidt echo resolution

Next, for that choice $h = 0.1$ of short imaginary time, the Loschmidt echo as a function of time, $\mathcal{G}(t) = \langle\psi|e^{-iHt}|\psi\rangle$, is computed estimating the phase as above by integration of the approximated imaginary time derivative. Fig. 4.3a shows the real and imaginary parts of the Loschmidt echo, with bright (dark) colors corresponding to the estimated (resp. exact) values. We observe how both amplitude and phase decrease oscillating in time with a phase shift of $\pi/2$. Fig. 4.3b shows the corresponding error of the estimation as a function of time. It is between one and two orders of magnitude smaller than the values for the Loschmidt echo. The main source of error has been checked to be indeed due to the phase estimation alone, yet remaining small.

4.4.4 Local density of states

Once the functions for Loschmidt echo resolution have been tested, some quantities such as the broadened version of the local density of states $D_{\delta,\psi}(E)$ introduced in (3.15) can be estimated to check the well functioning of the protocol. This should converge (up to a factor) to that quantity in the limit $\delta \to 0$.

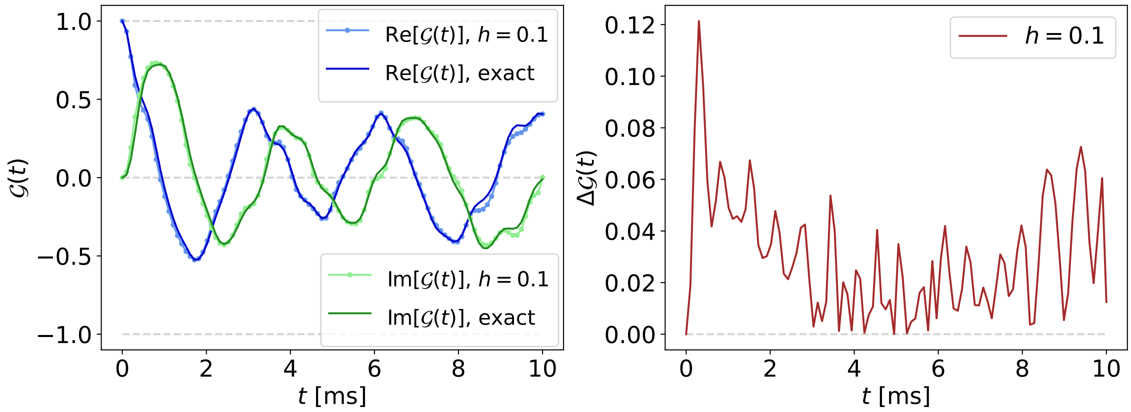

(a) Loschmidt echo's evolution.

(b) Loschmidt echo's error.

Figure 4.3: Real (green) and imaginary (blue) parts of the Loschmidt echo at time t, $\mathcal{G}(t) = \langle\psi|e^{-iHt}|\psi\rangle$, where the phase is resolved through imaginary time evolution with $h = 0.1$. The error (red) is one order of magnitude smaller. The Hamiltonian H under consideration is the Fermi-Hubbard model at $U/t = 8$ on a 3×2 lattice and the state $|\psi\rangle$ is an antiferromagnetic Fock state.

Fig. 4.4a shows $D_{\delta,k}(E_k)$ estimated through Loschmidt echos for the lowest energy spectrum E_k of the Fermi-Hubbard Hamiltonian H at $U/t = 8$ on a 3×2 lattice, where the state $|\psi\rangle$ has been taken to be the corresponding eigenstate $|E_k\rangle$ for each energy E_k. As δ decreases, the interval $[E - \delta, E + \delta]$ over which the filter $P_\delta(E)$ is applied shrinks, capturing thus fewer eigenstates and leading to a (slightly) lower estimation of the local density of states. Anyways, the estimations lie at 95-98% of the true (unnormalized) local density of states in the absence of degeneracies (i.e. one state per eigenenergy). Fig. 4.4b shows the convergence of $D_{\delta,\psi}(E_k)$ as a function of δ for the three lowest eigenenergies in the spectrum. When $|\psi\rangle$ is taken to be the corresponding eingestate $|E_k\rangle$, the estimation converges close to one (blue). If a state $|\psi\rangle$ with no overlap with the energy of interest E is instead considered — such as taking $|E_0\rangle$ for energy E_2 —, the interval $[E - \delta, E + \delta]$ will shrink with decreasing δ and end up not capturing the energy distribution of $|\psi\rangle$ at all, yielding convergence to zero (purple).

Next, the estimation of the local density of states $D_{\delta,\psi}(E)$ has been computed with a fixed state $|\psi\rangle$, namely the antiferromagnetic Fock state $|\mathrm{AFM}\rangle$, whose lowest energy distribution is shown in Fig. 4.5a. It has 5% overlap with an eigenstate at almost zero energy — i.e. close to its mean energy — and above 15% overlap with the ground state and two more low-energy excited states. This means one should be able to recover the estimation on the local density of states at those energies where overlap with $|\psi\rangle$ is non-negligible. Fig. 4.5b shows how $D_{\delta,\psi}(E)$ is recovered up to said overlap in the limit $\delta \to 0$ at the two lowest eigenenergies E_0 and E_1 (blue), where overlap with $|\mathrm{AFM}\rangle$ was just below 20% and 35%, respectively. Two further data curves have been added (purple) corresponding to energies close to the discrete spectrum but different to any

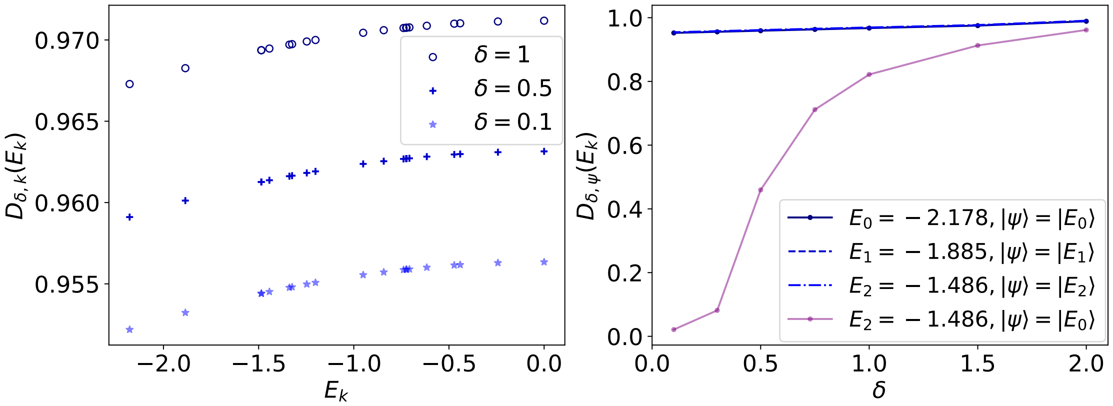

(a) Local density of states.

(b) Convergence.

Figure 4.4: (a) Broadened version $D_{\delta,\psi}(E_k) = \langle\psi|P_\delta(E_k)|\psi\rangle$ of the local density of states estimated with the (non-degenerate) eigenstates $|\psi\rangle = |E_k\rangle$. (b) When $|\psi\rangle = |E_k\rangle$, $D_{\delta,\psi}(E_k)$ convergences for decreasing δ (blue), while the signal is lost for any different $|\psi\rangle$ with no overlap with E_k (purple). The Fermi-Hubbard Hamiltonian H at $U/t = 8$ on a 3×2 lattice is considered and $h = 0.1$.

eigenenergy, i.e. $E \neq E_k$. For $E = -2.0$ (dark purple), the curve follows the blue ones for large and medium $\delta > 0$ for which $[E - \delta, E + \delta]$ still captures E_0 or E_1. For further smaller $\delta \simeq 0.05$, no eigenstate lies in that interval any more, which explains the sudden dropping of that curve at the last data point down to zero. For $E = 0$ (bright purple), instead, the eigenstate E_{14} is close enough to zero so as to still be captured by the filter's energy window at the lowest considered δ, approximately recovering said 5% overlap.

4.4.5 Full protocol testing

Last, the full protocol has been tested in two ways by computing the generalized microcanonical expectation values $H_{\delta,\psi}(E_k)$ at the eigenenergies E_k with the Hamiltonian energy H as observable of interest. Results are shown for $\delta = 1$. Studying the error when selecting the eigenergies — where no filtering error should appear — allows us to benchmark the error of the algorithm itself.

Fig. 4.6a shows the error $[H_{\delta,\psi}(E_k) - E_k]/N$ on the estimation of the Hamiltonian energy at the lowest part of the spectrum of the Fermi-Hubbard Hamiltonian H at $U/t = 8$ on a 3×2 lattice, where $|\psi\rangle$ is taken to be the eigenstate $|E_k\rangle$ corresponding to each eigenenergy E_k. Already for $\delta = 1$, the error is two orders of magnitude smaller than the physical value. All the error is due to approximations involved in the algorithm.

Fig. 4.6b shows the error $[H_{\delta,\psi}(E_k) - E_k]/N$ on the estimation of the Hamiltonian energy at the lowest part of the spectrum of the Fermi-Hubbard Hamiltonian H at $U/t = 8$ on a 3×2 lattice, where $|\psi\rangle$ is taken to be the fixed antiferromagnetic Fock state $|\mathrm{AFM}\rangle$ with (lowest energy) distribution shown in Fig. 4.5a. The error is only one order of magnitude smaller in this case, improving to two orders of magnitude when

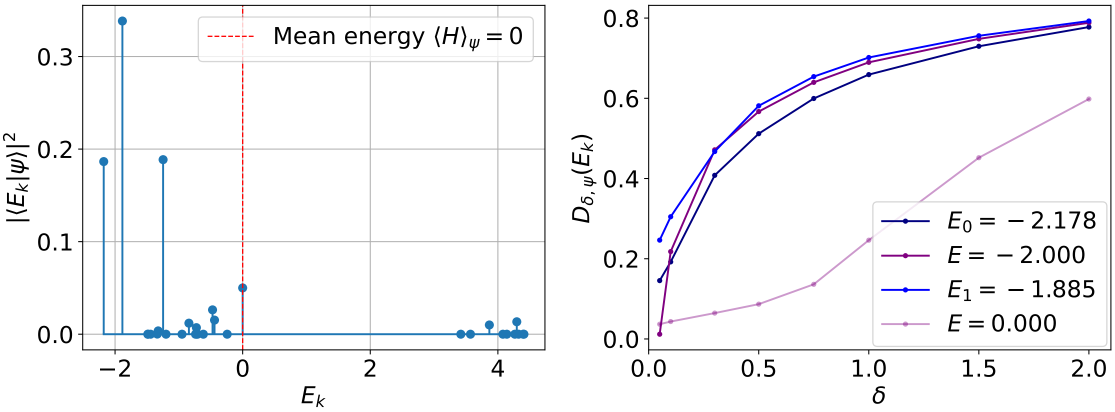

(a) Distribution of $|\mathrm{AFM}\rangle$.

(b) Local density of states.

Figure 4.5: Lowest energy distribution of the antiferromagnetic Fock state $|\psi\rangle = |\mathrm{AFM}\rangle$ with zero mean energy (left) together with the estimation on the local density of states $D_{\delta,\psi}(E)$ as a function of δ for different energies E. The Fermi-Hubbard Hamiltonian H at $U/t = 8$ on a 3×2 lattice is considered. $h = 0.1$.

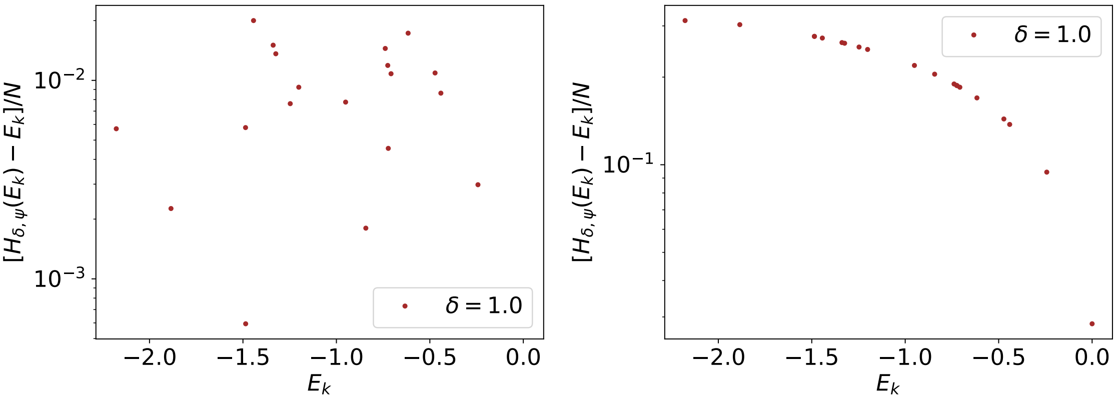

(a) Error when $|\psi\rangle = |E_k\rangle$.

(b) Error when $|\psi\rangle = |\mathrm{AFM}\rangle$.

Figure 4.6: Error $[H_{\delta,\psi}(E_k) - E_k]/N$ on the Hamiltonian energy estimation of the generalized expectation value retrieved through the proposed protocol. The evaluated energies E_k correspond to the lowest part of the spectrum of the Fermi-Hubbard Hamiltonian H at $U/t = 8$ on a $N = 3 \times 2$ lattice. The state $|\psi\rangle$ is taken to be either (a) each eigenstate $|E_k\rangle$ or (b) a fixed state given by the antiferromagnetic Fock state $|\mathrm{AFM}\rangle$. Parameters: $h = 0.1, \delta = 1$.

approaching the zero mean energy of the employed state $|\psi\rangle$. This shows that selecting a state for the filtering lying precisely at the target energy yields better estimates.

Chapter 5

Summary and Outlook

In this thesis, we have presented an efficient quantum-classical algorithm for the study of microcanonical properties of the two-dimensional Fermi-Hubbard model, designed to be implemented on the given fermionic quantum processor (FermiQP). The algorithm relies on a virtual filtering [83] that — without the need to prepare the physical state — recovers the physical values from the quantum simulator by performing interferometric measurements determining specific Loschmidt echos for an efficiently preparable state.

A family of initial states beyond simple Fock states has been considered and analyzed to access low-energy regimes while still being efficiently preparable. These states consisting of products of plaquettes with specific size have been shown to systematically approach the ground state benchmark [88] in the limit of large N. The mean energy density of different states has been studied in Table 3.1 varying plaquette size and doping.

The 2×2 plaquettes have then been chosen for the rest of the work as easy-to-prepare state to be considered. First, the accessible temperatures and entropies with such a state have been analyzed numerically. Although unable to provide quantitative results due to the classical hardness in simulation, insight has been learned from Fig. 3.6 and Fig. 3.8 on the thermal states $\rho_{\text{th}} = e^{-\beta H}/Z$ such plaquettes would have overlap with, even if not lying at the exact same energy density — as suggested by Fig. 3.7.

Subsequently, the state preparation of such product of plaquettes with the FermiQP demonstrator has been addressed in proposing two distinct adiabatic evolution schemes. The first one involves a spin and site dependent chemical potential while keeping the on-site interaction strength U fixed throughout the process, reaching state preparation fidelities of around 99.9% for evolution times of $T \simeq 50$ ms. The second option, on the other hand, circumvents the requirement on spin-dependent gradients at the price of tuning the U interaction, leading to near-perfect fidelities for evolution times $T \simeq 40$ ms. The latter combines the analog mode with the digital one in applying first a single layer of gates acting within double wells. The reversal of the adiabatic evolution relevant for measuring in the Fock basis has been addressed as well within a later section.

Next, the determination of Loschmidt echos $\langle\psi|e^{-iHt}|\psi\rangle$ for specific evolution times t has been addressed. Despite estimating the amplitude of these complex numbers with measurements on the quantum simulator has been argued to follow from a clear recipe, resolving their phase has proven to be a challenging task. Regarding this question, a possible solution given by the well-known Hadamard test has been reminded, highlighting its inconvenience consisting in the presence of global controlled operations. A second approach for symmetric Hamiltonians — including the Fermi-Hubbard model — circumventing the presence of global controlled gates has been discussed, yet holding only for states with a fixed number of spin down modes $N_\downarrow$ leading to a constrained range of positive energies $E(\psi) = \frac{1}{2}N_\downarrow U$, as seen in Fig. 3.15. To overcome all these obstacles, a new great solution based on [84] has been explored, beating the deficiencies of the previous approaches by relying in turn on the capacity of implementing a short imaginary time evolution to then recover the desired phase from complex analysis arguments [84].

The concrete way on how to realize the effect of the imaginary time evolution on the initial state has been then discussed following Motta et al. [95], arguing how a unitary can accomplish the task up to normalization. For plaquette states as initial state, it has been shown how only the imaginary time evolution between plaquettes has to be implemented, leading — for the Fermi-Hubbard Hamiltonian — to a circuit depth of four (even and odd for both vertical and horizontal hoppings) times the number of unitaries to implement the imaginary time evolution of a hopping term within neighboring sites. Although no such unitaries for 2 × 2 plaquettes have been found explicitly in analytical form in the time frame of this work, an approach based on the GRAPE [96] quantum optimal control method has been employed to obtain a pulse sequence (Fig. 3.20b) implementing the imaginary time evolution between two such plaquettes with high fidelities. Last, an analytical proof of principle has been shown for the limit of 1 × 1 “plaquettes” (taking a Fock state), where the corresponding gate has been decomposed into a sequence of two rotations. What hasn’t been shown in the present work is how to engineer these unitary rotations from the time evolution of native Hamiltonians, i.e. $U = e^{-iH\tau}$.

Last to mention, it has remained unclear how to implement the spectral function as observable involved in the Loschmidt echos to retrieve information on the pseudogap phase. Further, no state beyond half-filling has been properly studied yet, even though it has been commented on how doping could be introduced by considering plaquettes at different particle number sectors. Finally, only 2 × 2 plaquettes have been studied in depth so far, while being able to handle larger plaquettes would give access to lower, more interesting energies. Still, the proposed protocol is valid in general for the exploration of any other region in the phase diagram of the Fermi-Hubbard model.

Nevertheless, a full protocol for the implementation of the algorithm on a toy model consisting of a 3 × 2 lattice with an antiferromagnetic Fock state as initial state has been provided step by step as a proof-of-principle recipe to be executed at the FermiQP platform. This constitutes a big first step towards an implementable protocol to explore the rich physics captured by the 2D Fermi-Hubbard model on the FermiQP demonstrator.

Thus, a path towards a quantum-classical algorithm for the study of microcanonical properties of the two-dimensional Fermi-Hubbard model on the FermiQP quantum simulator has been proposed. Its successful implementation could open the doors to low-energy regimes of strongly correlated electron systems relevant for material science and quantum chemistry. Such algorithm takes advantage of both FermiQP’s analog mode providing full Hamiltonian evolution and adiabatic preparation schemes, together with the digital mode enabling the implementation of the required short imaginary time evolution through specific gate sequences.

Circumventing the actual filtering of the initial state constitutes a big advantage of this algorithm, leaving the classically hard part of the protocol for the quantum simulator, which computes the required Loschmidt echos to the prescribed accuracy. This comes with the disadvantage of needing a large amount of measurements to be carried out to determine every Loschmidt echo, each involving state preparation and Hamiltonian evolution again. Plus, the phase resolution technique further increases the number of measurements in requiring several data points for the phase integration.

Such algorithm is however interesting on itself in that it involves a concrete implementation of a short imaginary time evolution on a quantum simulator. And it provides a practical context where such milestone could be integrated to deliver an efficient protocol for research in condensed matter physics.

Further, the algorithm is best implemented on the FermiQP platform based on neutral atoms on an optical lattice, where the fermionic isotopes natively hop through the lattice as opposed to other architectures where the information is not contained in occupation numbers but in the internal energy states of the atoms.

The accessible energies and temperatures are still limited by the small plaquette sizes and absence of doping. Future work would study in more detail the introduction of doping in the plaquette-product state by defining a unit cell comprising several plaquettes with different particle numbers. The adiabatic preparation of such states would have to be revisited as well, although in general one could in future fully optimize any adiabatic evolution via optimal control techniques collaborating with other partners with expertise in the field, such as the one at Forschungszentrum Jülich. Dealing with larger plaquette sizes would have to be considered depending on the capabilities of quantum simulators as experimental achievements improve over time. Promising work on a native gate set within a double well suggests that rotation gates for the implementation of imaginary time evolution between plaquettes could be obtained explicitly from Hamiltonian evolution in a near future.

In the medium and long term, one could then start identifying and analyzing the main error sources in the protocol and try to mitigate them. The proof-of-principle toy model on a small sized lattice could give relevant insights in this respect, yet finite size effect could also be dominant and could spoil such information. The scaling to larger system sizes should not be problematic, since the protocol has been designed for states given by plaquettes that are homogeneously repeated over the lattice. As long as the demonstrator is able to handle a large number of sites, scaling up would be guaranteed. Additionally, the algorithm could further be extended for the actual computation of microcanonical and canonical expectation values by sampling over a whole basis set via Monte-Carlo sampling, perhaps benefiting from the knowledge at the Chair of Theoretical Nanophysics at the Ludwig Maximilian University of Munich. Last, quantum verification and benchmarking techniques to certify the computations from the FermiQP quantum device should be included to guarantee its well functioning or at least build trust on the success of the quantum computation. Such techniques could be developed in collaboration with partners such as the Chair of Quantum Algorithms and Applications at the Technical University of Munich.

Appendix A

Codes for numerical simulation

The full protocol applying the algorithm using 1×1 "plaquettes" has been simulated numerically with the following `python` code, specially relying on the `QuSpin` package:

```
from quspin.operators import hamiltonian # operators
from quspin.basis import spinful_fermion_basis_general # spin basis
import numpy as np # general math functions
from scipy.linalg import expm
from scipy import integrate
```

The code starts by defining the parameters of the simulation and then runs the algorithm. The basis `basis_2d` is restricted to the sector `Nf` of $3 \uparrow$ and $3 \downarrow$.

```
###### define model parameters ######
Lx, Ly = 3, 2 # linear dimension 2d lattice
N = Lx*Ly # number of sites
t  = 1 # hopping
U = 8 # onsite interaction
mu = 0.0 # chemical potential

###### define algorithm parameters ######
E = 0 # microcanonical target energy
delta = 0.1 # width of filtered state
x = 1 # defines Fourier transform cutoff
h = 0.1 # imaginary time
Delta_t = 0.1 # integration step

###### numerical settings ######
# setting up basis
basis_2d = spinful_fermion_basis_general(N, Nf=(3,3))
# setting up Hamiltonian for Fermi-Hubbard model
H = construct_H(Lx, Ly, t, U, mu, basis_2d, 'FHM')
```

```
###### Prepare initial state |psi> ######
psi = get_initial_state(Lx, Ly, basis_2d)

###### Compute generalized observable ######
Obs = get_observable(basis_2d)
O_delta_psi = generalized_observable(Obs,psi,E,delta,H,N,x,h,Delta_t)
```

This ends the protocol. Here, several functions have been defined. First, the function `construct_H` to construct the Hamiltonian `H` is given as follows:

```
def construct_H(Lx, Ly, t, U, mu, Basis, case):
    """ Constructs the Fermi-Hubbard model with parameters t, U and mu
    on a Lx*Ly lattice (or part of it). The FH Hamiltonian matrix may be
    constructed for either the whole Hilbert space or for a subspace of
    it, with basis 'Basis'. """
    ###### setting up 2d lattice indices and translations ######
    N = Lx*Ly # number of sites
    s = np.arange(N) # sites [0,1,2,...,N-1] in simple notation
    x = s%Lx # x positions for sites
    y = s//Lx # y positions for sites
    T_x = (x+1)%Lx + Lx*y # translation along x-direction
    T_y = x + Lx*((y+1)%Ly) # translation along y-direction
    ###### setting up Hamiltonian ######
    # setting up site-coupling lists
    if case == 'FHM':
        # OBC (delete both 'if' for PBC)
        hopping_left  = [[-t,i,T_x[i]] for i in range(N) if T_x[i]%Lx]
                        + [[-t,i,T_y[i]] for i in range(N) if T_y[i]>=Lx]
        hopping_right = [[+t,i,T_x[i]] for i in range(N) if T_x[i]%Lx]
                        + [[+t,i,T_y[i]] for i in range(N) if T_y[i]>=Lx]
    elif case == 'oh': # even horizontal hoppings only
        hopping_left  = [[-t,i,T_x[i]] for i in range(N)
                                if (T_x[i]%Lx and (i%Lx)%2)]
        hopping_right = [[+t,i,T_x[i]] for i in range(N)
                                if (T_x[i]%Lx and (i%Lx)%2)]
    elif case == 'eh': # odd horizontal hoppings only
        hopping_left  = [[-t,i,T_x[i]] for i in range(N)
                                if (T_x[i]%Lx and not((i%Lx)%2))]
        hopping_right = [[+t,i,T_x[i]] for i in range(N)
```

```
                                if (T_x[i]%Lx and not((i%Lx)%2))]
    elif case == 'ov': # even vertical hoppings only
        hopping_left  = [[-t,i,T_y[i]] for i in range(N)
                                if (T_y[i]>=Lx and (i//Ly)%2)]
        hopping_right = [[+t,i,T_y[i]] for i in range(N)
                                if (T_y[i]>=Lx and (i//Ly)%2)]
    elif case == 'ev': # odd vertical hoppings only
        hopping_left  = [[-t,i,T_y[i]] for i in range(N)
                                if (T_y[i]>=Lx and not((i//Ly)%2))]
        hopping_right = [[+t,i,T_y[i]] for i in range(N)
                                if (T_y[i]>=Lx and not((i//Ly)%2))]
    else:
        print('Warning: Hamiltonian case not defined.')
        return
    potential = [[-mu,i] for i in range(N)]
    interaction = [[U,i,i] for i in range(N)]
    # setting up static part of Hamiltonian (no dynamic part for FHM)
    static = [["+-|",hopping_left], # spin up hops to left
            ["-+|",hopping_right], # spin up hops to right
            ["|+-",hopping_left], # spin down hopes to left
            ["|-+",hopping_right], # spin up hops to right
            ["n|",potential], # onsite potenial, spin up
            ["|n",potential], # onsite potential, spin down
            ["n|n",interaction]] # spin up-spin down interaction
    # build hamiltonian
    H = hamiltonian(static, [], basis=Basis, dtype=np.float64)
    return H
```

Also, the initial state given by the antiferromagnet $|\uparrow,\downarrow,\uparrow,\downarrow,\uparrow,\downarrow\rangle$ is obtained through the function `get_initial_state` defined as follows:

```
def get_initial_state(Lx, Ly, Basis):
    """ Constructs the AFM state: |up, down, up, down, up, down>. """
    N = Lx*Ly
    # prepare AFM state
    s_up   = "".join("10" for i in range(N//2))
    s_down = "".join("01" for i in range(N//2))
    iAFM = Basis.index(s_up,s_down) # find  Fock state index in basis
    AFM = np.zeros(Basis.Ns) # allocate space for state
```

```
    AFM[iAFM] = 1.0 # set MB state to be the given product state 'AFM'
    return AFM
```

The observable A has sometimes directly been taken to be the Hamiltonian energy H. However, any other observable such as the local longitudinal magnetization may be defined within the function `get_observable`:

```
def get_observable(Basis):
    """ Constructs the observable Obs = n_{0,up} - n_{0,down},
    i.e. the local longitudinal magnetization on the first site (0). """
    # setting up site-coupling lists
    up_occupation   = [[+1,0]] #  up  spin occupation on first site only
    down_occupation = [[-1,0]] # down spin occupation on first site only
    # setting up static part of operator
    static = [["n|",up_occupation], ["|n",down_occupation]]
    # build operator
    Obs = hamiltonian(static, [], basis=Basis, dtype=np.float64)
    return Obs
```

The computation of the generalized microcanonical expectation value of the observable is left to the function `generalized_observable`:

```
def generalized_observable(Obs, psi, E, delta, H, N, x, h, Delta_t):
    """ Computes the generalized expectation value of the microcanonical
    observable
        Obs_{delta,psi}= [<psi|{Obs*P_delta(E) + P_delta(E)*Obs}|psi}]
                        / [2<psi|P_delta(E)|psi>]
    in terms of Loschmidt echos of type 1, 2 and 3, which the Quantum
    Simulator would compute (here implemented with 'Loschmidt_echo'
    function). """
    # compute parameters
    M = 2*np.floor((N*N)/(delta*delta)/2).astype(int) # nearest even int
    R = x*N/delta
    # check whether R is well defined
    if int(R) != R:
        print('Warning: R is not an integer. Need to choose x properly.')
        exit()
    elif R > M:
        print('Warning: M should be larger than R. Choose delta and x.')
        return
```

```python
# turn R into integer
R = int(R)
# construct sequence of times tm and coefficients bm
tm = np.array([(k)*2/N for k in range(R+1)])
    # tm = 2m/N for m=0,...,R (positives only)
bm = np.zeros(2*R+1)
# compute with logs for large numbers:
aux = np.array([np.log2(M - j) for j in range(M)]).sum()
for k in range(2*R+1):
    auxm = aux
    auxm = auxm - np.array([np.log2(M/2 - (-R + k) - j) for j
                            in range(int(M/2 - (-R + k)))]).sum()
    auxm = auxm - np.array([np.log2(M/2 + (-R + k) - j) for j
                            in range(int(M/2 + (-R + k)))]).sum()
    bm[k] = np.power(2, auxm - M)
# compute Loschmidt echos of each type
LE1, LE2, LE3 = np.zeros((3,2*R+1))
for k in range(len(tm)):
    if k == 0:
        LE1[R] = Loschmidt_echo(1, H, Obs, psi, 0, h, Delta_t)
        LE2[R] = Loschmidt_echo(2, H, Obs, psi, 0, h, Delta_t)
        LE3[R] = Loschmidt_echo(3, H, Obs, psi, 0, h, Delta_t)
    else: # use symmetry for negative times
        LE1[R+k] = Loschmidt_echo(1, H, Obs, psi, tm[k], h, Delta_t)
        LE2[R+k] = Loschmidt_echo(2, H, Obs, psi, tm[k], h, Delta_t)
        LE3[R+k] = Loschmidt_echo(3, H, Obs, psi, tm[k], h, Delta_t)
        LE1[R-k] = np.conj(LE1[R+k])
        LE2[R-k] = np.conj(LE3[R+k])
        LE3[R-k] = np.conj(LE2[R+k])
# compute generalized observable
tm = np.array([(-R + k)*2/N for k in range(2*R+1)])
    # tm = 2m/N for m=-R,...,R = k-R with k=0,...,2R
num = (bm*np.exp(1j*E*tm)*(LE2m+LE3m)).sum()
denom = (bm*np.exp(1j*E*tm)*LE1m).sum()*2
O_delta_psi = num/denom
return O_delta_psi
```

This function in turn calls the `Loschmidt_echo` function to compute the required Loschmidt echos at the suitable times. It is defined as follows:

```
def Loschmidt_echo(type, H, Obs, psi, tm, h, Delta_t):
    """ Computes Loschmidt echo (LE) of type 1, 2 or 3:
        LE type 1: <psi|e^{-iHt}|psi>
        LE type 2: <psi|Obs*e^{-iHt}|psi>
        LE type 3: <psi|e^{-iHt}*Obs|psi>
    measuring the amplitudes by sampling and resolving the phases through
    ITE e^{-hH} (see 'resolve_phase' function). """
    if type == 1:
        # Obtain amplitude
        expt_psi = H.evolve(psi,0,tm,imag_time=False) # e^-iHt |psi>
        r = np.abs(np.dot(psi,expt_psi)) # |<psi|e^{-iHt}|psi>|
        # Resolve phase
        phase = resolve_phase(1, H, Obs, psi, tm, h, Delta_t)
    elif type == 2:
        # Obtain amplitude
        expt_psi = H.evolve(psi,0,tm,imag_time=False) # e^-iHt |psi>
        O_expt_psi = Obs.dot(expt_psi,time=0,check=True) # O e^-iHt |psi>
        r = np.abs(np.dot(psi,O_expt_psi)) # |<psi|O*e^{-iHt}|psi>|
        # Resolve phase
        phase = resolve_phase(2, H, Obs, psi, tm, h, Delta_t)
    elif type == 3:
        O_psi = Obs.dot(psi,time=0,check=True) # O |psi>
        expt_O_psi = H.evolve(O_psi,0,tm,imag_time=False) # e^-iHt O |psi>
        r = np.abs(np.dot(psi,expt_O_psi)) # |<psi|e^{-iHt}*O|psi>|
        # Resolve phase
        phase = resolve_phase(3, H, Obs, psi, tm, h, Delta_t)
    else:
        print('Warning: Loschmidt echo of type', type, 'is not defined.')
        return
    # Put together
    LE = r*np.exp(1j*phase) # r e^i\phi
    return LE
```

This function in turn estimates the phase of the Loschmidt echos through the function `resolve_phase`, defined as follows:

```
def resolve_phase(type, H, Obs, psi, tm, h, Delta_t):
    """ It resolves the phase of a Loschmidt echo ot type 1, 2 or 3 by:
        i)   implementing ITE
```

```
    ii)  computing the amplitudes r(t +- ih)
    iii) approximating the imaginary time derivative of ln(r)
            with finite difference
    iv)  integrating the phase numerically. """
# discretize time interval [0, tm] for integration
isteps = np.abs(int(tm/Delta_t)) + 1 # Delta_t: integration step
tk = np.linspace(0, tm, num=isteps) # t_k
# initialize arrays
evol_psi = np.zeros((isteps, 2, len(psi)), dtype=np.complex64)
r = np.zeros((isteps, 2), dtype=np.complex64)
gamma = np.zeros(isteps, dtype=float)
Hmatrix = H.tocsr()
Hmatrix = Hmatrix.todense()
phase0 = 0
if type == 1:
    phim = (expm(-h*Hmatrix)).dot(psi) # e^-hH |psi>
    phip = (expm(+h*Hmatrix)).dot(psi) # e^+hH |psi>
    """should implement ITE gates instead:
    # phim = ITE_1x1(Lx, Ly, t, basis_2d, psi, h) # e^-hH |psi>
    # phip = ITE_1x1(Lx, Ly, t, basis_2d, psi, -h) # e^+hH |psi> """
    # initial phase
    phase0 = 0 # arg <psi|psi>
    for k in range(isteps):
        # Obtain amplitude r(t_k - ih) = |<psi|e^-iHt_k e^-hH|psi>|
        if k == 0:
            evol_psi[k,0,:] = H.evolve(phim,0,tk[k],imag_time=False)
                                                # e^-iHt_k e^-hH |psi>
        else:
            evol_psi[k,0,:] = H.evolve(evol_psi[k-1,0,:],tk[k-1],
                    tk[k], imag_time=False) # e^-iHt_k e^-hH |psi>
        r[k,0] = np.abs(np.dot(psi,evol_psi[k,0,:])) # r(t_k - ih)
        # Obtain amplitude r(t_k + ih) = |<psi|e^-iHt_k e^+hH|psi>|
        if k == 0:
            evol_psi[k,1,:] = H.evolve(phip,0,tk[k],imag_time=False)
                                                # e^-iHt_k e^+hH |psi>
        else:
            evol_psi[k,1,:] = H.evolve(evol_psi[k-1,1,:],tk[k-1],
                    tk[k], imag_time=False) # e^-iHt_k e^+hH |psi>
```

```
            r[k,1] = np.abs(np.dot(psi,evol_psi[k,1,:])) # r(t_k + ih)
            # Estimate imaginary time derivative of ln(r)
            if k > 0: gamma[k] = (np.log(np.real(r[k,0]))
                                   - np.log(np.real(r[k,1])))/(2*h)
    elif type == 2:
        phim = (expm(-h*Hmatrix)).dot(psi) # e^-hH |psi>
        phip = (expm(+h*Hmatrix)).dot(psi) # e^+hH |psi>
        """should implement ITE gates instead:
        phim = ITE_1x1(Lx, Ly, t, basis_2d, psi, h) # e^-hH |psi>
        phip = ITE_1x1(Lx, Ly, t, basis_2d, psi, -h) # e^+hH |psi> """
        # initial phase
        phase0 = np.angle(Obs.expt_value(psi)) # arg <psi|O|psi>
        for k in range(isteps):
            # Obtain amplitude r(t_k - ih) = |<psi|O e^-iHt_k e^-hH|psi>|
            if k == 0:
                evol_psi[k,0,:] = H.evolve(phim,0,tk[k],imag_time=False)
                                                # e^-iHt_k e^-hH |psi>
            else:
                evol_psi[k,0,:] = H.evolve(evol_psi[k-1,0,:],tk[k-1],
                        tk[k], imag_time=False) # e^-iHt_k e^-hH |psi>
            evol_psi[k,0,:] = Obs.dot(evol_psi[k,0,:],time=0,check=True)
                                                # O e^-iHt_k e^-hH |psi>
            r[k,0] = np.abs(np.dot(psi,evol_psi[k,0,:])) # r(t_k - ih)
            # Obtain amplitude r(t_k + ih) = |<psi|O e^-iHt_k e^+hH|psi>|
            if k == 0:
                evol_psi[k,1,:] = H.evolve(phip,0,tk[k],imag_time=False)
                                                # e^-iHt_k e^+hH |psi>
            else:
                evol_psi[k,1,:] = H.evolve(evol_psi[k-1,1,:],tk[k-1],
                        tk[k], imag_time=False) # e^-iHt_k e^+hH |psi>
            evol_psi[k,1,:] = Obs.dot(evol_psi[k,1,:],time=0,check=True)
                                                # O e^-iHt_k e^+hH |psi>
            r[k,1] = np.abs(np.dot(psi,evol_psi[k,1,:])) # r(t_k + ih)
            # Estimate imaginary time derivative of ln(r)
            if k > 0: gamma[k] = (np.log(np.real(r[k,0]))
                                   - np.log(np.real(r[k,1])))/(2*h)
    elif type == 3:
        Opsi = Obs.dot(psi,time=0,check=True) # O |psi>
```

```
        phimO = (expm(-h*Hmatrix)).dot(Opsi) # e^-hH O |psi>
        phipO = (expm(+h*Hmatrix)).dot(Opsi) # e^+hH O |psi>
        """should implement ITE gates instead:
        phimO = ITE_1x1(Lx, Ly, t, basis_2d, Opsi, h) # e^-hH O |psi>
        phipO = ITE_1x1(Lx, Ly, t, basis_2d, Opsi, -h) # e^+hH O |psi>
        with a pulse sequence optmized for the state O|psi> instead."""
        # initial phase
        phase0 = np.angle(Obs.expt_value(psi)) # arg <psi|O|psi>
        for k in range(isteps):
            # Obtain amplitude r(t_k - ih) = |<psi|e^-iHt_k e^-hH O|psi>|
            if k == 0: evol_psi[k,0,:] = H.evolve(phimO,0,tk[k],imag_time=
                                            False) # e^-iHt_k e^-hH O |psi>
            else: evol_psi[k,0,:] = H.evolve(evol_psi[k-1,0,:],tk[k-1],
                                tk[k], imag_time=False) # e^-iHt_k e^-hH O |psi>
            r[k,0] = np.abs(np.dot(psi,evol_psi[k,0,:])) # r(t_k - ih)
            # Obtain amplitude r(t_k + ih) = |<psi|e^-iHt_k e^+hH O|psi>|
            if k == 0: evol_psi[k,1,:] = H.evolve(phipO,0,tk[k],imag_time=
                                            False) # e^-iHt_k e^+hH O |psi>
            else: evol_psi[k,1,:] = H.evolve(evol_psi[k-1,1,:],tk[k-1],
                                tk[k], imag_time=False) # e^-iHt_k e^+hH O |psi>
            r[k,1] = np.abs(np.dot(psi,evol_psi[k,1,:])) # r(t_k + ih)
            # Estimate imaginary time derivative of ln(r)
            if k > 0: gamma[k] = (np.log(np.real(r[k,0]))
                                        - np.log(np.real(r[k,1])))/(2*h)
    else:
        print('Warning: Loschmidt echo of type', type, 'is not defined.')
        return
    # estimate phase by integration
    phase = phase0 + (gamma*Delta_t).sum()
    return phase%(2*np.pi) # (phase-np.pi)%(2*np.pi)-np.pi # in [-pi,pi]
```

The function that would implement the imaginary time evolution (ITE) between 1 × 1 “plaquettes” through previously optimized pulse sequences, is defined as follows:

```
def ITE_1x1(Lx, Ly, t, basis_2d, phi, h):
    """ Implements imaginary time evolution e^{-hH} on 1x1 plaquettes
    by applying the corresponding (optimized) pulse sequence for each of
    the 4 non-commuting layers: horizontal/vertical with even/odd. """
    U, mu = 8, 0
```

```
if h > 0: # ITE pulse sequence (1x1): 30 steps, 99.96% fidelity.
    t_s =
    [0.74198237,0.19902577,0.03580839,0.06216097,0.48975395,0.957848,
    0.95064562,0.47683249,0.05917705,0.04076871,0.21981493,0.74243817,
    0.94588595,0.6606147,0.16279287,0.02746031,0.12040639,0.56648806,
    0.83032992,0.66574926,0.23927655,0.02598068,0.11777753,0.54651277,
    0.83811079,0.70349491,0.25723853,0.03948775,0.02265397,0.485852]
elif h < 0: # ITE pulse sequence (1x1): 30 steps, 99.96% fidelity.
    t_s =
    [0.93913415,2.19925806,2.9394367,2.49514729,1.25416662, 0.50622435,
    0.59648825,1.71658816,2.75143612,2.71565766,1.60209629,0.54096024,
    0.50959105,1.27111601,2.47433212,2.76885509,1.85736753,0.62352598,
    0.47901146,0.96298534,2.25370858,2.81255679,2.12869171,0.85619701,
    0.49386383,0.74118908,2.03926055,2.87035476,2.48801875,1.2775673 ]
else: print('Warning: h=0 !')
tsteps = len(t_s)
# ITE pulse reconstruction:
terms = ['eh', 'ev']
if Lx > 2: terms = terms + ['oh']
if Ly > 2: terms = terms + ['ov']
for term in terms: # odd/even horizontal/vertical hopping terms
    for k in range(tsteps):
        H_k = construct_H(Lx, Ly, t_s[k], U, mu, basis_2d, term)
        phi = H_k.evolve(phi, 0, h)
# norm factor
phi = phi * np.power(np.sqrt(1+2*h*h*t*t), (Lx-1)*Ly + (Ly-1)*Lx)
return phi
```

Bibliography

[1] Paul Benioff. The computer as a physical system: A microscopic quantum mechanical hamiltonian model of computers as represented by turing machines. *Journal of Statistical Physics*, 22:563–591, 1980. URL https://api.semanticscholar.org/CorpusID:122949592.

[2] Y. Manin. Computable and uncomputable, 1980. Sovetskoye Radio, Moscow 128.

[3] Richard P. Feynman. Simulating physics with computers. *International Journal of Theoretical Physics*, 21:467–488, 1982. doi: 10.1007/BF02650179. URL https://doi.org/10.1007/BF02650179.

[4] David Deutsch and Richard Jozsa. Rapid solution of problems by quantum computation. *Proceedings of the Royal Society of London. Series A: Mathematical and Physical Sciences*, 439:553 – 558, 1992. URL https://api.semanticscholar.org/CorpusID:121702767.

[5] D.R. Simon. On the power of quantum computation. In *Proceedings 35th Annual Symposium on Foundations of Computer Science*, pages 116–123, 1994. doi: 10.1109/SFCS.1994.365701.

[6] Ethan Bernstein and Umesh Vazirani. Quantum complexity theory. *SIAM Journal on Computing*, 26(5):1411–1473, 1997. doi: 10.1137/S0097539796300921. URL https://doi.org/10.1137/S0097539796300921.

[7] P.W. Shor. Algorithms for quantum computation: discrete logarithms and factoring. In *Proceedings 35th Annual Symposium on Foundations of Computer Science*, pages 124–134, 1994. doi: 10.1109/SFCS.1994.365700.

[8] Lov K. Grover. A fast quantum mechanical algorithm for database search. In *Proceedings of the Twenty-Eighth Annual ACM Symposium on Theory of Computing*, STOC '96, page 212–219, New York, NY, USA, 1996. Association for Computing Machinery. ISBN 0897917855. doi: 10.1145/237814.237866. URL https://doi.org/10.1145/237814.237866.

[9] Seth Lloyd. Universal quantum simulators. *Science*, 273(5278):1073–1078, 1996. doi: 10.1126/science.273.5278.1073. URL https://www.science.org/doi/abs/10.1126/science.273.5278.1073.

[10] J. I. Cirac and P. Zoller. Quantum computations with cold trapped ions. *Phys. Rev. Lett.*, 74:4091–4094, May 1995. doi: 10.1103/PhysRevLett.74.4091. URL https://link.aps.org/doi/10.1103/PhysRevLett.74.4091.

[11] Y. Nakamura, Yu. A. Pashkin, and J. S. Tsai. Coherent control of macroscopic quantum states in a single-cooper-pair box. *Nature*, 398(6730):786–788, April 1999. ISSN 1476-4687. doi: 10.1038/19718. URL `http://dx.doi.org/10.1038/19718`.

[12] D. Vion, A. Aassime, A. Cottet, P. Joyez, H. Pothier, C. Urbina, D. Esteve, and M. H. Devoret. Manipulating the quantum state of an electrical circuit. *Science*, 296(5569):886–889, May 2002. ISSN 1095-9203. doi: 10.1126/science.1069372. URL `http://dx.doi.org/10.1126/science.1069372`.

[13] J. A. Schreier, A. A. Houck, Jens Koch, D. I. Schuster, B. R. Johnson, J. M. Chow, J. M. Gambetta, J. Majer, L. Frunzio, M. H. Devoret, S. M. Girvin, and R. J. Schoelkopf. Suppressing charge noise decoherence in superconducting charge qubits. *Physical Review B*, 77(18), May 2008. ISSN 1550-235X. doi: 10.1103/physrevb.77.180502. URL `http://dx.doi.org/10.1103/PhysRevB.77.180502`.

[14] Oliver Morsch and Markus Oberthaler. Dynamics of bose-einstein condensates in optical lattices. *Rev. Mod. Phys.*, 78:179–215, Feb 2006. doi: 10.1103/RevModPhys.78.179. URL `https://link.aps.org/doi/10.1103/RevModPhys.78.179`.

[15] Marco Anderlini, Patricia J. Lee, Benjamin L. Brown, Jennifer Sebby-Strabley, William D. Phillips, and J. V. Porto. Controlled exchange interaction between pairs of neutral atoms in an optical lattice. *Nature*, 448(7152):452–456, July 2007. ISSN 1476-4687. doi: 10.1038/nature06011. URL `http://dx.doi.org/10.1038/nature06011`.

[16] E. Urban, T. A. Johnson, T. Henage, L. Isenhower, D. D. Yavuz, T. G. Walker, and M. Saffman. Observation of rydberg blockade between two atoms. *Nature Physics*, 5(2):110–114, January 2009. ISSN 1745-2481. doi: 10.1038/nphys1178. URL `http://dx.doi.org/10.1038/nphys1178`.

[17] Alpha Gaëtan, Yevhen Miroshnychenko, Tatjana Wilk, Amodsen Chotia, Matthieu Viteau, Daniel Comparat, Pierre Pillet, Antoine Browaeys, and Philippe Grangier. Observation of collective excitation of two individual atoms in the rydberg blockade regime. *Nature Physics*, 5(2):115–118, January 2009. ISSN 1745-2481. doi: 10.1038/nphys1183. URL `http://dx.doi.org/10.1038/nphys1183`.

[18] R. Hanson, L. P. Kouwenhoven, J. R. Petta, S. Tarucha, and L. M. K. Vandersypen. Spins in few-electron quantum dots. *Rev. Mod. Phys.*, 79:1217–1265, Oct 2007. doi: 10.1103/RevModPhys.79.1217. URL `https://link.aps.org/doi/10.1103/RevModPhys.79.1217`.

[19] E. Knill, R. Laflamme, and G. J. Milburn. A scheme for efficient quantum computation with linear optics. *Nature*, 409:46–52, 2001. doi: 10.1038/35051009.

[20] David P. DiVincenzo. The physical implementation of quantum computation. *Fortschritte der Physik*, 48(9–11):771–783, September 2000. ISSN 1521-3978. doi: 10.1002/1521-3978(200009)48:9/11⟨771::aid-prop771⟩3.0.co;

2-e. URL http://dx.doi.org/10.1002/1521-3978(200009)48:9/11<771::AID-PROP771>3.0.CO;2-E.

[21] Dorit Aharonov and Michael Ben-Or. Fault-tolerant quantum computation with constant error rate, 1999. URL https://arxiv.org/abs/quant-ph/9906129.

[22] Emanuel Knill, Raymond Laflamme, and Wojciech H. Zurek. Resilient quantum computation: error models and thresholds. *Proceedings of the Royal Society of London. Series A: Mathematical, Physical and Engineering Sciences*, 454(1969): 365–384, January 1998. ISSN 1471-2946. doi: 10.1098/rspa.1998.0166. URL http://dx.doi.org/10.1098/rspa.1998.0166.

[23] A.Yu. Kitaev. Fault-tolerant quantum computation by anyons. *Annals of Physics*, 303(1):2–30, January 2003. ISSN 0003-4916. doi: 10.1016/s0003-4916(02)00018-0. URL http://dx.doi.org/10.1016/S0003-4916(02)00018-0.

[24] Matthew DeCross, Reza Haghshenas, Minzhao Liu, Enrico Rinaldi, Johnnie Gray, Yuri Alexeev, Charles H. Baldwin, John P. Bartolotta, Matthew Bohn, Eli Chertkov, Julia Cline, Jonhas Colina, Davide DelVento, Joan M. Dreiling, Cameron Foltz, John P. Gaebler, Thomas M. Gatterman, Christopher N. Gilbreth, Joshua Giles, Dan Gresh, Alex Hall, Aaron Hankin, Azure Hansen, Nathan Hewitt, Ian Hoffman, Craig Holliman, Ross B. Hutson, Trent Jacobs, Jacob Johansen, Patricia J. Lee, Elliot Lehman, Dominic Lucchetti, Danylo Lykov, Ivaylo S. Madjarov, Brian Mathewson, Karl Mayer, Michael Mills, Pradeep Niroula, Juan M. Pino, Conrad Roman, Michael Schecter, Peter E. Siegfried, Bruce G. Tiemann, Curtis Volin, James Walker, Ruslan Shaydulin, Marco Pistoia, Steven. A. Moses, David Hayes, Brian Neyenhuis, Russell P. Stutz, and Michael Foss-Feig. The computational power of random quantum circuits in arbitrary geometries, 2024. URL https://arxiv.org/abs/2406.02501.

[25] Tomi H. Johnson, Stephen R. Clark, and Dieter Jaksch. What is a quantum simulator? *EPJ Quantum Technology*, 1:10, 2014. doi: 10.1140/epjqt10. URL https://doi.org/10.1140/epjqt10.

[26] I.M. Georgescu, S. Ashhab, and Franco Nori. Quantum simulation. *Reviews of Modern Physics*, 86(1):153–185, March 2014. ISSN 1539-0756. doi: 10.1103/revmodphys.86.153. URL http://dx.doi.org/10.1103/RevModPhys.86.153.

[27] Francesco Tacchino, Alessandro Chiesa, Stefano Carretta, and Dario Gerace. Quantum computers as universal quantum simulators: State-of-the-art and perspectives. *Advanced Quantum Technologies*, 3(3), December 2019. ISSN 2511-9044. doi: 10.1002/qute.201900052. URL http://dx.doi.org/10.1002/qute.201900052.

[28] J. Ignacio Cirac and Peter Zoller. Goals and opportunities in quantum simulation. *Nature Physics*, 8:264–266, 2012. doi: 10.1038/nphys2275. URL https://doi.org/10.1038/nphys2275.

[29] Axel Friedenauer, Hector Schmitz, Jan Tibor Glückert, Diego Porras, and Tobias Schätz. Simulating the quantum magnet, 2008. URL https://arxiv.org/abs/0802.4072.

[30] R. Gerritsma, G. Kirchmair, F. Zähringer, E. Solano, R. Blatt, and C. F. Roos. Quantum simulation of the dirac equation. *Nature*, 463(7277):68–71, January 2010. ISSN 1476-4687. doi: 10.1038/nature08688. URL http://dx.doi.org/10.1038/nature08688.

[31] M. Greiner, O. Mandel, T. Rom, A. Altmeyer, A. Widera, T.W. Hänsch, and I. Bloch. Quantum phase transition from a superfluid to a mott insulator in an ultracold gas of atoms. *Physica B: Condensed Matter*, 329-333:11–12, 2003. ISSN 0921-4526. doi: https://doi.org/10.1016/S0921-4526(02)01872-0. URL https://www.sciencedirect.com/science/article/pii/S0921452602018720. Proceedings of the 23rd International Conference on Low Temperature Physics.

[32] B. P. Lanyon, J. D. Whitfield, G. G. Gillett, M. E. Goggin, M. P. Almeida, I. Kassal, J. D. Biamonte, M. Mohseni, B. J. Powell, M. Barbieri, A. Aspuru-Guzik, and A. G. White. Towards quantum chemistry on a quantum computer. *Nature Chemistry*, 2 (2):106–111, January 2010. ISSN 1755-4349. doi: 10.1038/nchem.483. URL http://dx.doi.org/10.1038/nchem.483.

[33] C. Monroe, W. C. Campbell, L.-M. Duan, Z.-X. Gong, A. V. Gorshkov, P. W. Hess, R. Islam, K. Kim, N. M. Linke, G. Pagano, P. Richerme, C. Senko, and N. Y. Yao. Programmable quantum simulations of spin systems with trapped ions. *Reviews of Modern Physics*, 93(2), 2021. ISSN 1539-0756. doi: 10.1103/revmodphys.93.025001. URL http://dx.doi.org/10.1103/RevModPhys.93.025001.

[34] D. Leibfried, B. DeMarco, V. Meyer, M. Rowe, A. Ben-Kish, J. Britton, W. M. Itano, B. Jelenković, C. Langer, T. Rosenband, and D. J. Wineland. Trapped-ion quantum simulator: Experimental application to nonlinear interferometers. *Physical Review Letters*, 89(24), 2002. ISSN 1079-7114. doi: 10.1103/physrevlett.89.247901. URL http://dx.doi.org/10.1103/PhysRevLett.89.247901.

[35] M. Neeley, M. Ansmann, R. C. Bialczak, M. Hofheinz, E. Lucero, A. D. O'Connell, D. Sank, H. Wang, J. Wenner, A. N. Cleland, M. R. Geller, and J. M. Martinis. Emulation of a quantum spin with a superconducting phase qudit. *Science*, 325: 722–725, 2009. doi: 10.1126/science.1173440.

[36] J. P. F. LeBlanc, Andrey E. Antipov, Federico Becca, Ireneusz W. Bulik, Garnet Kin-Lic Chan, Chia-Min Chung, Youjin Deng, Michel Ferrero, Thomas M. Henderson, Carlos A. Jiménez-Hoyos, E. Kozik, Xuan-Wen Liu, Andrew J. Millis, N. V. Prokof'ev, Mingpu Qin, Gustavo E. Scuseria, Hao Shi, B. V. Svistunov, Luca F. Tocchio, I. S. Tupitsyn, Steven R. White, Shiwei Zhang, Bo-Xiao Zheng, Zhenyue Zhu, and Emanuel Gull. Solutions of the two-dimensional hubbard model: Benchmarks and results from a wide range of numerical algorithms. *Physical Review*

X, 5(4), December 2015. ISSN 2160-3308. doi: 10.1103/physrevx.5.041041. URL `http://dx.doi.org/10.1103/PhysRevX.5.041041`.

[37] Thomas Schäfer, Nils Wentzell, Fedor Šimkovic, Yuan-Yao He, Cornelia Hille, Marcel Klett, Christian J. Eckhardt, Behnam Arzhang, Viktor Harkov, François-Marie Le Régent, Alfred Kirsch, Yan Wang, Aaram J. Kim, Evgeny Kozik, Evgeny A. Stepanov, Anna Kauch, Sabine Andergassen, Philipp Hansmann, Daniel Rohe, Yuri M. Vilk, James P. F. LeBlanc, Shiwei Zhang, A.-M. S. Tremblay, Michel Ferrero, Olivier Parcollet, and Antoine Georges. Tracking the footprints of spin fluctuations: A multimethod, multimessenger study of the two-dimensional hubbard model. *Phys. Rev. X*, 11:011058, Mar 2021. doi: 10.1103/PhysRevX.11.011058. URL `https://link.aps.org/doi/10.1103/PhysRevX.11.011058`.

[38] Ulrich Schneider, Lucia Hackermüller, Jens Philipp Ronzheimer, Sebastian Will, Simon Braun, Thorsten Best, Immanuel Bloch, Eugene Demler, Stephan Mandt, David Rasch, and Achim Rosch. Fermionic transport and out-of-equilibrium dynamics in a homogeneous hubbard model with ultracold atoms. *Nature Physics*, 8(3):213–218, January 2012. ISSN 1745-2481. doi: 10.1038/nphys2205. URL `http://dx.doi.org/10.1038/nphys2205`.

[39] Ian G. White, Randall G. Hulet, and Kaden R. A. Hazzard. Correlations generated from high-temperature states: Nonequilibrium dynamics in the fermi-hubbard model. *Phys. Rev. A*, 100:033612, Sep 2019. doi: 10.1103/PhysRevA.100.033612. URL `https://link.aps.org/doi/10.1103/PhysRevA.100.033612`.

[40] Rahul Trivedi, Adrian Franco Rubio, and J. Ignacio Cirac. Quantum advantage and stability to errors in analogue quantum simulators, 2023. URL `https://arxiv.org/abs/2212.04924`.

[41] H. F. Trotter. On the product of semi-groups of operators. *Proceedings of the American Mathematical Society*, 10(4):545–551, 1959. ISSN 00029939, 10886826. URL `http://www.jstor.org/stable/2033649`.

[42] David Layden. First-order trotter error from a second-order perspective. *Physical Review Letters*, 128(21), May 2022. ISSN 1079-7114. doi: 10.1103/physrevlett.128.210501. URL `http://dx.doi.org/10.1103/PhysRevLett.128.210501`.

[43] Sergey B. Bravyi and Alexei Yu. Kitaev. Fermionic quantum computation. *Annals of Physics*, 298(1):210–226, May 2002. ISSN 0003-4916. doi: 10.1006/aphy.2002.6254. URL `http://dx.doi.org/10.1006/aphy.2002.6254`.

[44] P. Jordan and E. Wigner. Über das Paulische Äquivalenzverbot. *Zeitschrift fur Physik*, 47(9-10):631–651, September 1928. doi: 10.1007/BF01331938.

[45] F Verstraete and J I Cirac. Mapping local hamiltonians of fermions to local hamiltonians of spins. *Journal of Statistical Mechanics: Theory and Experiment*, 2005(09): P09012–P09012, September 2005. ISSN 1742-5468. doi: 10.1088/1742-5468/2005/09/p09012. URL `http://dx.doi.org/10.1088/1742-5468/2005/09/P09012`.

[46] Kanav Setia, Sergey Bravyi, Antonio Mezzacapo, and James D. Whitfield. Superfast encodings for fermionic quantum simulation. *Physical Review Research*, 1 (3), October 2019. ISSN 2643-1564. doi: 10.1103/physrevresearch.1.033033. URL http://dx.doi.org/10.1103/PhysRevResearch.1.033033.

[47] Charles Derby, Joel Klassen, Johannes Bausch, and Toby Cubitt. Compact fermion to qubit mappings. *Physical Review B*, 104(3), July 2021. ISSN 2469-9969. doi: 10.1103/physrevb.104.035118. URL http://dx.doi.org/10.1103/PhysRevB.104.035118.

[48] Yu-An Chen and Yijia Xu. Equivalence between fermion-to-qubit mappings in two spatial dimensions. *PRX Quantum*, 4:010326, Mar 2023. doi: 10.1103/PRXQuantum.4.010326. URL https://link.aps.org/doi/10.1103/PRXQuantum.4.010326.

[49] Mitchell Chiew and Sergii Strelchuk. Discovering optimal fermion-qubit mappings through algorithmic enumeration. *Quantum*, 7:1145, October 2023. ISSN 2521-327X. doi: 10.22331/q-2023-10-18-1145. URL https://doi.org/10.22331/q-2023-10-18-1145.

[50] Oliver O'Brien and Sergii Strelchuk. Ultrafast hybrid fermion-to-qubit mapping. *Phys. Rev. B*, 109:115149, Mar 2024. doi: 10.1103/PhysRevB.109.115149. URL https://link.aps.org/doi/10.1103/PhysRevB.109.115149.

[51] D. González-Cuadra, D. Bluvstein, M. Kalinowski, R. Kaubruegger, N. Maskara, P. Naldesi, T. V. Zache, A. M. Kaufman, M. D. Lukin, H. Pichler, B. Vermersch, Jun Ye, and P. Zoller. Fermionic quantum processing with programmable neutral atom arrays. *Proceedings of the National Academy of Sciences*, 120(35), August 2023. ISSN 1091-6490. doi: 10.1073/pnas.2304294120. URL http://dx.doi.org/10.1073/pnas.2304294120.

[52] Qingyu Li, Chiranjib Mukhopadhyay, and Abolfazl Bayat. Fermionic simulators for enhanced scalability of variational quantum simulation. *Physical Review Research*, 5 (4), November 2023. ISSN 2643-1564. doi: 10.1103/physrevresearch.5.043175. URL http://dx.doi.org/10.1103/PhysRevResearch.5.043175.

[53] Antoine Michel. Quantum simulation for strongly interacting fermions with neutral atoms array: towards the simulation of materials of interest, 2024. URL https://arxiv.org/abs/2406.13343.

[54] Fabian H. L. Essler, Holger Frahm, Frank Göhmann, Andreas Klümper, and Vladimir E. Korepin. *The One-Dimensional Hubbard Model*. Cambridge University Press, 2005.

[55] Bo-Xiao Zheng, Chia-Min Chung, Philippe Corboz, Georg Ehlers, Ming-Pu Qin, Reinhard M. Noack, Hao Shi, Steven R. White, Shiwei Zhang, and Garnet Kin-Lic Chan. Stripe order in the underdoped region of the two-dimensional hubbard

model. *Science*, 358(6367):1155–1160, December 2017. ISSN 1095-9203. doi: 10.1126/science.aam7127. URL `http://dx.doi.org/10.1126/science.aam7127`.

[56] Christian Gross and Immanuel Bloch. Quantum simulations with ultracold atoms in optical lattices. *Science*, 357(6355):995–1001, 2017. doi: 10.1126/science.aal3837. URL `https://www.science.org/doi/abs/10.1126/science.aal3837`.

[57] Lawrence W. Cheuk, Matthew A. Nichols, Melih Okan, Thomas Gersdorf, Vinay V. Ramasesh, Waseem S. Bakr, Thomas Lompe, and Martin W. Zwierlein. Quantum-gas microscope for fermionic atoms. *Physical Review Letters*, 114(19), May 2015. ISSN 1079-7114. doi: 10.1103/physrevlett.114.193001. URL `http://dx.doi.org/10.1103/PhysRevLett.114.193001`.

[58] Christie S. Chiu, Geoffrey Ji, Anton Mazurenko, Daniel Greif, and Markus Greiner. Quantum state engineering of a hubbard system with ultracold fermions. *Physical Review Letters*, 120(24), June 2018. ISSN 1079-7114. doi: 10.1103/physrevlett.120.243201. URL `http://dx.doi.org/10.1103/PhysRevLett.120.243201`.

[59] Christie S. Chiu, Geoffrey Ji, Annabelle Bohrdt, Muqing Xu, Michael Knap, Eugene Demler, Fabian Grusdt, Markus Greiner, and Daniel Greif. String patterns in the doped hubbard model. *Science*, 365(6450):251–256, July 2019. ISSN 1095-9203. doi: 10.1126/science.aav3587. URL `http://dx.doi.org/10.1126/science.aav3587`.

[60] Anton Mazurenko, Christie S. Chiu, Geoffrey Ji, Maxwell F. Parsons, Márton Kanász-Nagy, Richard Schmidt, Fabian Grusdt, Eugene Demler, Daniel Greif, and Markus Greiner. A cold-atom fermi–hubbard antiferromagnet. *Nature*, 545(7655):462–466, May 2017. ISSN 1476-4687. doi: 10.1038/nature22362. URL `http://dx.doi.org/10.1038/nature22362`.

[61] Thomas Hartke, Botond Oreg, Ningyuan Jia, and Martin Zwierlein. Quantum register of fermion pairs. *Nature*, 601(7894):537–541, January 2022. ISSN 1476-4687. doi: 10.1038/s41586-021-04205-8. URL `http://dx.doi.org/10.1038/s41586-021-04205-8`.

[62] Hao-Tian Wei, Eduardo Ibarra Garcia Padilla, Kaden Hazzard, Michael Wall, Zoe Yan, Benjamin Spar, Max Prichard, Sungjae Chi, and Waseem Bakr. Effective Hubbard parameters for programmable tweezer arrays. In *APS March Meeting Abstracts*, volume 2023 of *APS Meeting Abstracts*, page T66.012, January 2023.

[63] Benjamin Spar, Max Prichard, Siddharth Dandavate, Zoe Yan, and Waseem Bakr. Programmable Fermi-Hubbard Lattices. In *APS Division of Atomic, Molecular and Optical Physics Meeting Abstracts*, volume 2023 of *APS Meeting Abstracts*, page N01.130, January 2023.

[64] Martin C. Gutzwiller. Effect of correlation on the ferromagnetism of transition metals. *Phys. Rev. Lett.*, 10:159–162, Mar 1963. doi: 10.1103/PhysRevLett.10.159. URL `https://link.aps.org/doi/10.1103/PhysRevLett.10.159`.

[65] Hubbard J. Electron correlations in narrow energy bands. *Proc. R. Soc. Lond.*, A 276:238–257, 1963.

[66] Hubbard J. Electron correlations in narrow energy bands iii. an improved solution. *Proc. R. Soc. Lond.*, A 281:401–419, 1964.

[67] P. W. Anderson. New approach to the theory of superexchange interactions. *Phys. Rev.*, 115:2–13, Jul 1959. doi: 10.1103/PhysRev.115.2. URL `https://link.aps.org/doi/10.1103/PhysRev.115.2`.

[68] Norbert Schuch and Frank Verstraete. Computational complexity of interacting electrons and fundamental limitations of density functional theory. *Nature Physics*, 5(10):732–735, August 2009. ISSN 1745-2481. doi: 10.1038/nphys1370. URL `http://dx.doi.org/10.1038/nphys1370`.

[69] Julia Kempe, Alexei Kitaev, and Oded Regev. The complexity of the local hamiltonian problem, 2005. URL `https://arxiv.org/abs/quant-ph/0406180`.

[70] E. Gull and A. J. Millis. Ten years of Nature Physics: Numerical models come of age. *Nature Physics*, 11(10):808–810, October 2015. doi: 10.1038/nphys3501.

[71] D. Jaksch, C. Bruder, J. I. Cirac, C. W. Gardiner, and P. Zoller. Cold bosonic atoms in optical lattices. *Physical Review Letters*, 81(15):3108–3111, October 1998. ISSN 1079-7114. doi: 10.1103/physrevlett.81.3108. URL `http://dx.doi.org/10.1103/PhysRevLett.81.3108`.

[72] Belen Paredes, Artur Widera, Valentin Murg, Olaf Mandel, Simon Folling, Ignacio Cirac, Georgy V. Shlyapnikov, Theodor Hansch, and Immanuel Bloch. Tonks-Girardeau gas of ultracold atoms in an optical lattice. *Nature*, 429:277–281, 2004. URL `https://hal.science/hal-00002239`.

[73] Thomas Uehlinger, Gregor Jotzu, Michael Messer, Daniel Greif, Walter Hofstetter, Ulf Bissbort, and Tilman Esslinger. Artificial graphene with tunable interactions. *Physical Review Letters*, 111(18), October 2013. ISSN 1079-7114. doi: 10.1103/physrevlett.111.185307. URL `http://dx.doi.org/10.1103/PhysRevLett.111.185307`.

[74] D. Porras and J. I. Cirac. Bose-einstein condensation and strong-correlation behavior of phonons in ion traps. *Physical Review Letters*, 93(26), December 2004. ISSN 1079-7114. doi: 10.1103/physrevlett.93.263602. URL `http://dx.doi.org/10.1103/PhysRevLett.93.263602`.

[75] D. Porras and J. I. Cirac. Phonon Superfluids in Sets of Trapped Ions. *Foundations of Physics*, 36(4):465–476, April 2006. doi: 10.1007/s10701-005-9036-6.

[76] A. F. Ho, M. A. Cazalilla, and T. Giamarchi. Quantum simulation of the hubbard model: The attractive route. *Physical Review A*, 79(3), March 2009. ISSN 1094-1622. doi: 10.1103/physreva.79.033620. URL `http://dx.doi.org/10.1103/PhysRevA.79.033620`.

[77] Andrew J. Daley, Immanuel Bloch, Christian Kokail, Stuart Flannigan, Natalie Pearson, Matthias Troyer, and Peter Zoller. Practical quantum advantage in quantum simulation. *Nature*, 607:667–676, 2022. doi: 10.1038/s41586-022-04940-6. URL `https://doi.org/10.1038/s41586-022-04940-6`.

[78] Jia-Wei Ji and David L. Feder. Extending matchgates to universal quantum computation via the hubbard model. *Phys. Rev. A*, 100:052324, Nov 2019. doi: 10.1103/PhysRevA.100.052324. URL `https://link.aps.org/doi/10.1103/PhysRevA.100.052324`.

[79] Thomas Chalopin, Petar Bojović, Dominik Bourgund, Si Wang, Titus Franz, Immanuel Bloch, and Timon Hilker. Optical superlattice for engineering hubbard couplings in quantum simulation, 2024. URL `https://arxiv.org/abs/2405.19322`.

[80] Thomas Chalopin. Optical superlattices in quantum gas microscopy. *Nature Reviews Physics*, 3:605, 2021. doi: 10.1038/s42254-021-00357-8. URL `https://doi.org/10.1038/s42254-021-00357-8`.

[81] Mingpu Qin, Thomas Schäfer, Sabine Andergassen, Philippe Corboz, and Emanuel Gull. The hubbard model: A computational perspective. *Annual Review of Condensed Matter Physics*, 13(1):275–302, March 2022. ISSN 1947-5462. doi: 10.1146/annurev-conmatphys-090921-033948. URL `http://dx.doi.org/10.1146/annurev-conmatphys-090921-033948`.

[82] D. Galanakis, E. Khatami, K. Mikelsons, A. Macridin, J. Moreno, D. A. Browne, and M. Jarrell. Quantum criticality and incipient phase separation in the thermodynamic properties of the hubbard model. *Philosophical Transactions of the Royal Society A: Mathematical, Physical and Engineering Sciences*, 369(1941): 1670–1686, April 2011. ISSN 1471-2962. doi: 10.1098/rsta.2010.0228. URL `http://dx.doi.org/10.1098/rsta.2010.0228`.

[83] Sirui Lu, Mari Carmen Bañuls, and J. Ignacio Cirac. Algorithms for quantum simulation at finite energies. *PRX Quantum*, 2:020321, May 2021. doi: 10.1103/PRXQuantum.2.020321. URL `https://link.aps.org/doi/10.1103/PRXQuantum.2.020321`.

[84] Yilun Yang, Arthur Christianen, Mari Carmen Bañuls, Dominik S. Wild, and J. Ignacio Cirac. Phase-sensitive quantum measurement without controlled operations. *Phys. Rev. Lett.*, 132:220601, May 2024. doi: 10.1103/PhysRevLett.132.220601. URL `https://link.aps.org/doi/10.1103/PhysRevLett.132.220601`.

[85] Mark Srednicki. Chaos and quantum thermalization. *Physical Review E*, 50(2): 888–901, August 1994. ISSN 1095-3787. doi: 10.1103/physreve.50.888. URL `http://dx.doi.org/10.1103/PhysRevE.50.888`.

[86] Joshua M Deutsch. Eigenstate thermalization hypothesis. *Reports on Progress in Physics*, 81(8):082001, July 2018. ISSN 1361-6633. doi: 10.1088/1361-6633/aac9f1. URL `http://dx.doi.org/10.1088/1361-6633/aac9f1`.

[87] Yimin Ge, Jordi Tura, and J. Ignacio Cirac. Faster ground state preparation and high-precision ground energy estimation with fewer qubits. *Journal of Mathematical Physics*, 60(2):022202, 02 2019. ISSN 0022-2488. doi: 10.1063/1.5027484. URL https://doi.org/10.1063/1.5027484.

[88] Philippe Corboz. Improved energy extrapolation with infinite projected entangled-pair states applied to the two-dimensional hubbard model. *Physical Review B*, 93(4), January 2016. ISSN 2469-9969. doi: 10.1103/physrevb.93.045116. URL http://dx.doi.org/10.1103/PhysRevB.93.045116.

[89] Phillip Weinberg and Marin Bukov. Quspin: a python package for dynamics and exact diagonalisation of quantum many body systems. part ii: bosons, fermions and higher spins. *SciPost Physics*, 7(2), August 2019. ISSN 2542-4653. doi: 10.21468/scipostphys.7.2.020. URL http://dx.doi.org/10.21468/SciPostPhys.7.2.020.

[90] Alexander Wietek, Yuan-Yao He, Steven R. White, Antoine Georges, and E. Miles Stoudenmire. Stripes, antiferromagnetism, and the pseudogap in the doped hubbard model at finite temperature. *Phys. Rev. X*, 11:031007, Jul 2021. doi: 10.1103/PhysRevX.11.031007. URL https://link.aps.org/doi/10.1103/PhysRevX.11.031007.

[91] Edward Farhi, Jeffrey Goldstone, Sam Gutmann, and Michael Sipser. Quantum computation by adiabatic evolution, 2000. URL https://arxiv.org/abs/quant-ph/0001106.

[92] Sabine Jansen, Mary-Beth Ruskai, and Ruedi Seiler. Bounds for the adiabatic approximation with applications to quantum computation. *Journal of Mathematical Physics*, 48(10), October 2007. ISSN 1089-7658. doi: 10.1063/1.2798382. URL http://dx.doi.org/10.1063/1.2798382.

[93] Andrew M. Childs and Nathan Wiebe. Hamiltonian simulation using linear combinations of unitary operations. *Quantum Information and Computation*, 12(11 & 12), November 2012. ISSN 1533-7146. doi: 10.26421/qic12.11-12. URL http://dx.doi.org/10.26421/QIC12.11-12.

[94] Shantanav Chakraborty. Implementing any linear combination of unitaries on intermediate-term quantum computers, 2024. URL https://arxiv.org/abs/2302.13555.

[95] Mario Motta, Chong Sun, Adrian T. K. Tan, Matthew J. O'Rourke, Erika Ye, Austin J. Minnich, Fernando G. S. L. Brandão, and Garnet Kin-Lic Chan. Determining eigenstates and thermal states on a quantum computer using quantum imaginary time evolution. *Nature Physics*, 16(2):205–210, November 2019. ISSN 1745-2481. doi: 10.1038/s41567-019-0704-4. URL http://dx.doi.org/10.1038/s41567-019-0704-4.

[96] Navin Khaneja, Timo Reiss, Cindie Kehlet, Thomas Schulte-Herbrüggen, and Steffen J. Glaser. Optimal control of coupled spin dynamics: design of nmr pulse sequences by gradient ascent algorithms. *Journal of Magnetic Resonance*, 172(2):296–305, 2005. ISSN 1090-7807. doi: https://doi.org/10.1016/j.jmr.2004.11.004. URL `https://www.sciencedirect.com/science/article/pii/S1090780704003696`.

[97] Richard H. Byrd, Peihuang Lu, Jorge Nocedal, and Ciyou Zhu. A limited memory algorithm for bound constrained optimization. *SIAM Journal on Scientific Computing*, 16(5):1190–1208, 1995. doi: 10.1137/0916069. URL `https://doi.org/10.1137/0916069`.

[98] Ciyou Zhu, Richard H. Byrd, Peihuang Lu, and Jorge Nocedal. Algorithm 778: L-bfgs-b: Fortran subroutines for large-scale bound-constrained optimization. *ACM Trans. Math. Softw.*, 23(4):550–560, dec 1997. ISSN 0098-3500. doi: 10.1145/279232.279236. URL `https://doi.org/10.1145/279232.279236`.

List of Figures

Acknowledgements

This work has been possible thanks to the great support of many people, to whom I am deeply indebted. I am most thankful to Prof. Dr. Ignacio Cirac for letting me join the Theory Division at the Max Planck Institute for Quantum Optics (MPQ) throughout the duration of this thesis. I have had the chance to witness not only the cutting edge research level found at this remarkable place — reaffirmed by Prof. Dr. Ferenc Krausz's Nobel Prize in Physics 2023 during my stay at the institute —, but also the coexisting impressive human atmosphere that prevails in this workplace. My thanks extend to Dr. Philipp Preiss, without whom this opportunity of joining the FermiQP collaboration wouldn't have been possible. Thanks for the chance of taking part on this project from the experimental side at Prof. Dr. Immanuel Bloch's group at the Quantum Many Body Division already before starting my thesis, and for later suggesting this project from the theoretical point of view, not to mention the countless discussions together with Dr. Timon Hilker. My most sincere gratitude goes to Dr. Luis Escalera and M.Sc. Benjamin Schiffer for the joint work and guidance throughout the project, bringing out the best of myself while making the way towards the goal an enjoyable time. Thanks for all those insightful conversations beyond the project, helping me better grasp what science is all about and opening my eyes to various soft skills that will surely have a deep impact on my career.

This thesis builds upon many years of study and internships in both physics and mathematics at the Polytechnic University of Catalonia within the CFIS program in Barcelona, the Max Planck Institute for Physics, the European Organization for Nuclear Research (CERN) and the California Institute of Technology (Caltech), in addition to the current master jointly run by the Ludwig Maximilian University and the Technical University of Munich, as well as to the present research stay at MPQ. I am very grateful for each and every one on the way who inspired me to dive into the seas of quantum physics.

Special thanks go to my parents, family and beloved ones for their immense support. Notably to you, Rahel, for being there for me through thick and thin. Thank you in particular to Johannes P., Johannes R., Momme H., Gonzalo F. and Albert R., for being a rock to lean on now and then throughout this journey.

I acknowledge the Elitenetzwerk Bayern for making possible the elite master course in Theoretical and Mathematical Physics.

D.O.G.

Statement of authorship:

I hereby declare that this thesis is my own work, and that I have not used any sources and aids other than those stated in the thesis.

Place, Date

Signature